CHALMERS

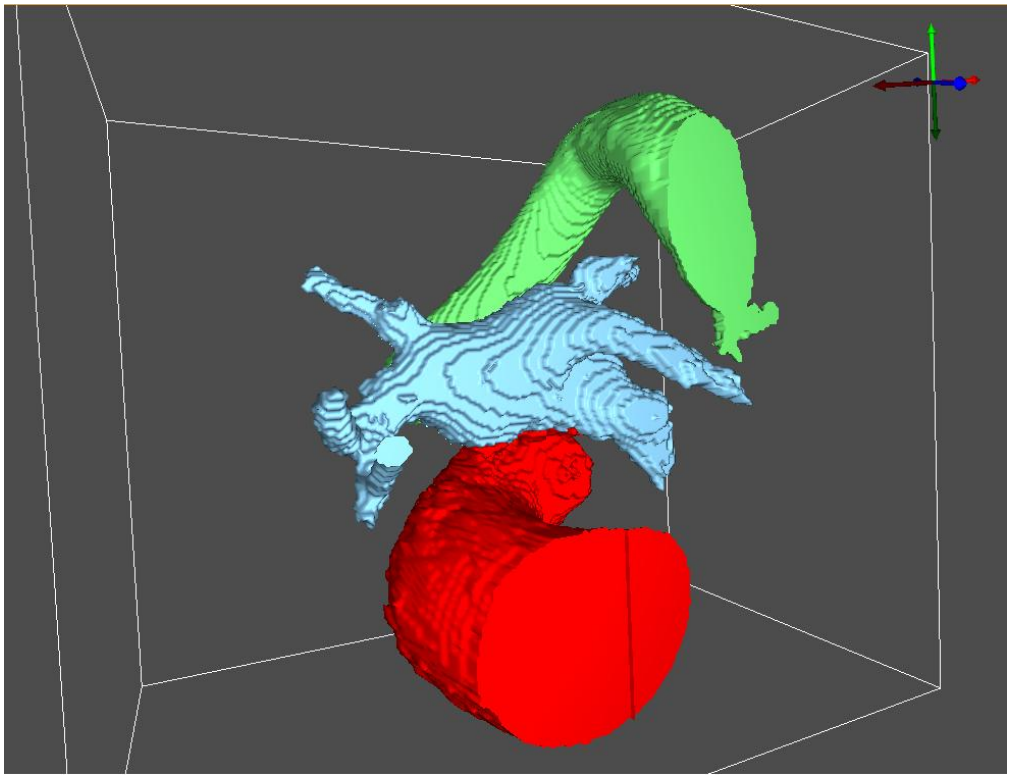

Segmentation of the Left Atrium using the Marker-Controlled Watershed algorithm

Master of Science Thesis [in the Master Degree Programme, MPBME]

REZA GHARIPOUR

Department of Signal and Systems
CHALMERS UNIVERSITY OF TECHNOLOGY
Gothenburg, Sweden 2013
Ex057/2013

THESIS FOR THE DEGREE OF MASTER OF SCIENCE

Segmentation of the Left Atrium Using the Marker-Controlled Watershed algorithm

REZA GHARIPOUR

Supervisor:
OLE JAKOB ELLE

The Intervention Centre
Oslo University Hospital
Faculty of Medicine
University of Oslo
Oslo, Norway

Examiner:
YNGVE HAMNERIUS

Department of Signal and Systems
Chalmers University of Technology

Segmentation of the Left Atrium using the Marker-Controlled Watershed algorithm
Reza Gharipour

Thesis for the degree of Master of Science
Department of Signal and Systems
Chalmers University of Technology
SE-412 96 Gothenburg
Sweden
Telephone: +46 (0)31-772 1000

Cover:
Segmented Left Atrium plus the pulmonary veins using the Marker-Controlled Watershed algorithm

Abstract

According to the statistics heart disease is the cause of more than 600,000 deaths per year in the USA. While 715,000 Americans annually have a heart stroke, it has been also the main cause of death in lots of other developing countries as well [1]. Among them, about 15% of all the heart attacks are associated with a condition called Atrial Fibrillation (AF). In case of permanent AF, Radio Frequency Catheter Ablation (RFCA) must be applied on the patient to prevent the risk of death. Hence knowing an exact geometry of the heart and its chambers is vital in success of the operation. Nevertheless, segmenting the Left Atrium (LA) and its pulmonary veins (PVs) has been always a challenging task due to high variability of the LA. During the last years several methods have been proposed to overcome this situation.

Here we proposed a segmentation method based on the Marker-Controlled Watershed algorithm, in order to extract a 3D geometry of the LA and its PVs. Also we compared results of the method by their corresponding ground truth images (manual segmentation) to find the estimated error of the method. The results implied that while the method is fast and parameter free, yet we encounter the oversegmentation issue in some cases. According to our observation, oversegmentation occurs mostly in the Left Ventricle (LV) and also the PVs. The overall result confirmed a mean overlap of 65-99% between the ground truth image and our method for all datasets.

Keywords : Atrial Fibrillation, Radio Frequency Catheter Ablation, Segmentation, Left Atrium, Marker-Controlled Watershed

Acknowledgements

The most part of this master thesis was done in the Intervention Centre at the Oslo University Hospital (Rikshospitalet) during 2012-2013. This has been possible only with a numerous support and dedication provided by my supervisors and colleagues at Chalmers University in Gothenburg and the Intervention Centre in Oslo.

Firstly, I would like to thank my supervisors Professor Yngve Hamnerius in Gothenburg and Professor Ole Jakob Elle in Oslo, all your supports and guidance beside the positive feedbacks assisted me in the way of completing this master thesis. Most immediately, special thanks to Dr. Hugues Fontenelle and Rafael Palomar at the Intervention Centre, your patience, kindliness and motivation during this time is highly appreciated. Development of the c++ code and implementation of the algorithm was definitely impossible without your cooperation and collaboration. Least but not last, I would like to thank Oslo University Hospital which provided me the place to work on my master thesis.

Table of Contents

Introduction

Radio Frequency catheter ablation (RFCA) is the sole solution of the permanent Atrial Fibrillation (AF). AF is a condition in which electrical impulses of the heart starts in the atria, instead of Sino-Atrial node (SA node). Hence finding a precise anatomy of the heart and its chambers is vital in this operation. From the other side, an efficient contact between the tissue and the electrode plays an important role in success of the operation. While insufficient contact pressure may produce a superficial lesion with no efficient isolating impact; excessive contact pressure from the other side may puncture wall of the heart or hurt the esophagus. Image modalities like Magnetic Resonance Angiography (MRA) and Computed Tomography Angiography (CTA) have made it possible to extract a 3D geometry of the heart and its chambers using segmentation. Although segmentation of the left atrium and its pulmonary veins is not necessary, but it is beneficial for pre operative evaluation of the LA geometry in the RFCA operation. Among all the other segmentation methods which have been proposed, this document introduces a method for segmentation of LA and its PVs using the Marker-Controlled Watershed algorithm. It must be clarified that this master thesis was a part of an EU project with cooperation of the Oslo University Hospital. Also the segmentation method used in this master thesis (Marker-Controlled Watershed algorithm) was decided and defined by my supervisor at the Oslo University Hospital. The main task defined in this master thesis was to design and implement a pipeline to do the segmentation since using watershed algorithm alone does not lead to a satisfactory result. This document consists of 8 chapters and 2 appendices. Chapter 1 gives some backgrounds about the AF and the RFCA procedure, chapter 2 introduces imaging of the LA and its PVs prior to the ablation. Chapter 3 describes several segmentation algorithms of the LA and integration of the selected algorithm into the software (3DSlicer) is done in chapter 4. Chapter 5 describes the results and outcome of the method and we will discuss more about those results in chapter 6. While conclusion is done in chapter 7, we will represent the references in chapter 8. Finally two appendices are included in this document as Appendix A and Appendix B in chapters 9 and 10. Appendix A illustrates the results of the segmentation and their corresponding ground truth image and Appendix B depicts accuracy of the method in segmenting all 12 datasets based on Hausdorff distance algorithm.

1. Background

1.1 Heart Anatomy and Physiology

The human heart is a biological structure that is placed in the thoracic cavity posterior to the sternum, superior to the thoracic diaphragm and between the lungs. The size of the heart is similar to a clenched fist and it weighs 250-300 grams in females to 300-350 grams in males. The main functionality of the heart is to receive oxygenated blood through the pulmonary veins from the lungs and then send it to other parts of the body through the arteries, arterioles and capillaries. In addition, the heart also receives de-oxygenated blood through the superior and inferior Vena Cava from the body tissues and passes it to the lungs via the pulmonary artery [2-4].

Valves and Chambers:

The heart consists of four chambers, two lower chambers and two upper chambers. The upper part of the heart is called atrium and the lower part is called ventricle. The atrium and the ventricle are divided in two parts by a partition called septum. The inter-atrial septum divides the atrium into the left and the right atria, and the inter-ventricular septum divides the ventricle into the left and the right ventricles. The atria receive the blood that comes back from the body to the heart, then the ventricle pump the blood which was received by the atria to all parts of the body (Figure 1). There are two valves between the atria and the ventricles which allow flow of the blood only in one direction from the atria to the ventricles. The tricuspid valve allows the blood to flow from the right atrium to the right ventricle. In the other side of the heart the mitral valve is responsible for flowing of the blood from the left atrium to the left ventricle [5-6].

There are two other valves in the heart, the aortic valve that is located between the left ventricle and the aorta, and the pulmonary valve that allows the blood to flow from the right ventricle to the pulmonary artery [5-6].

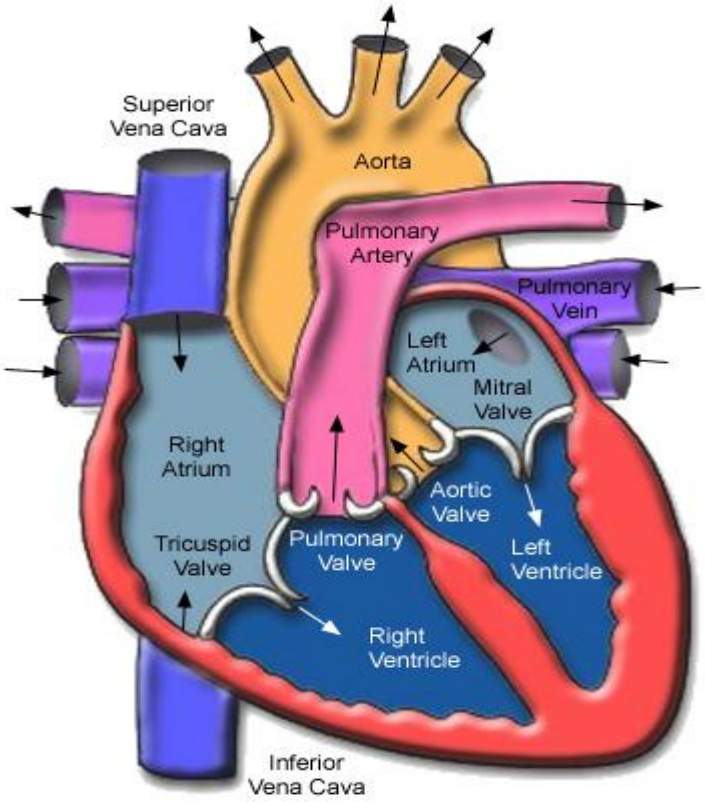

Figure1. Anatomy of the heart [31].

Wall and Layers*:*

The muscular wall of the heart is composed of three layers; the outset layer of the heart that is called epicardium is composed of connective tissue and is covered by epithelium which provides an outer protection for the heart. The mid layer of the heart called myocardium consists of contracting cardiac muscle fibers and it stimulates the heart contractions. The most inner layer of the heart which also covers the valves of the heart called endocardium is composed of epithelial tissue and connective tissue [5-6].

Cardiac cycle:

The cardiac cycle of the heart can be divided into two phases, the first phase occurs when the ventricles are relaxed and the heart is filled by the blood (so called diastolic phase) and the next phase is when the ventricles contract and pump the blood to the arteries which is called systolic phase [7-8].

Cardiac Conduction System:

The cardiac conduction of the heart (Figure 2) starts at the SA node. This node which located in the upper wall of the right atrium, generates electrical impulses which propagate all through the heart's wall, this leads to contraction of both atria, then the impulses reach to the Atrio-Ventricular (AV) node that is located in the right side of the septum near the bottom of the right atrium, here there is a small amount of delay which helps the atrium to be contracted, these impulses go further down toward the right and the left ventricles through the atrioventricular bundle and at the end when they reach to the purkinje fibers, these fibers will trigger the muscle fibers of the ventricles and cause them to contract and push the blood towards the lungs and rest of the body. Finally, the ventricles will be relaxed and a new impulse will start again in the SA node, this process is known as a normal heartbeat [7-8].

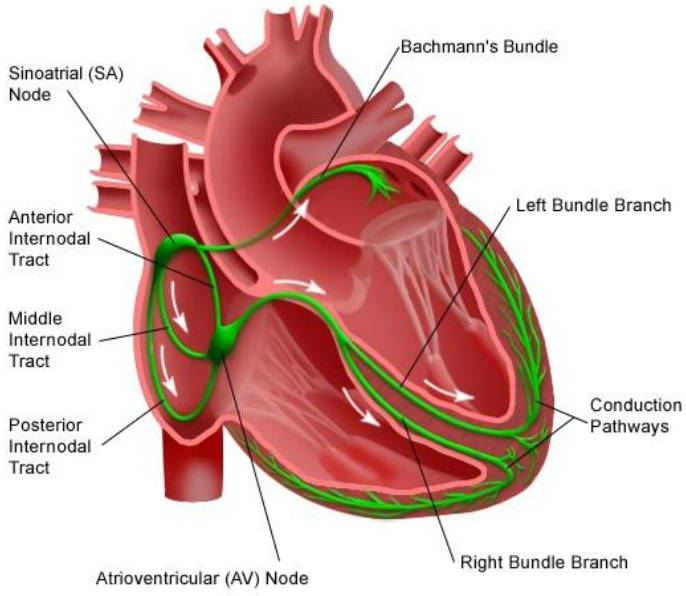

Figure2. Cardiac Conduction System of the Heart [32].

1.2 Atrial Fibrillation

Atrial Fibrillation (AF) is the most common type of arrhythmia, affecting millions of persons worldwide. During AF (Figure 3), generated electrical pulses may spread in a rapid and uncommon manner throughout the atrium which may lead to a fibrillation in the atria. In this case, the ventricles will also beat faster than the normal rate, but less than the rate of the atria, so the beat rate of the atria and the ventricles will be uncoordinated. As a result, the blood will not be pumped completely from the atria to the ventricles and a part of it may remain in the ventricles, this, among other adverse effects, might lead to formation of clots which in turn increases the risk of stroke, as the clots can move toward the brain [9-10].

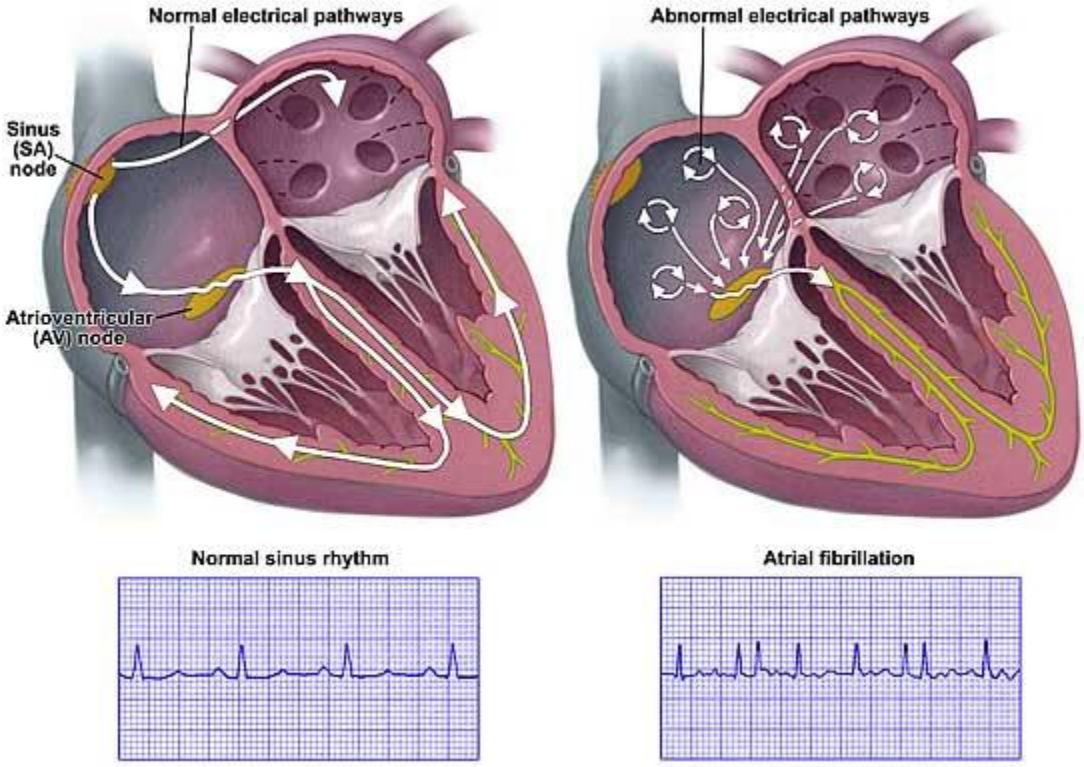

Figure 3. Normal vs. Abnormal electrical activity of the heart [30].

Sign and symptoms:

An irregular and fast rhythm of the heartbeat is the most common sign of AF; other symptoms are dizziness, palpitations, weakness and breathlessness, confusion, hypotension, angina, disorders of the heart muscle and heart failure [11-13].

Most common types:

AF may be paroxysmal, persistent or longstanding persistent. In paroxysmal AF the symptoms may last from a few seconds up to minutes, hours or even a few days, but it stops by its own. In persistent AF the symptoms will continue until patient goes under the medical treatment. Longstanding persistent AF or permanent AF cannot be stopped by the common medical treatments [11-13].

Cause:

AF has a close relation with aging and it can be seen rarely in young people, some elements which can contribute to the occurrence of the AF are : smoking, alcohol, hypertension, mitral valve disease, coronary artery disease, hyperthyroidism, atrial flutter, cardiomyopathy, pericarditis, previous heart surgery and so on [11-13].

Treatment, medication and drugs:

Treatment of AF varies from one patient to another patient. It mostly depends on the cause (if the cause is known), duration and acuteness of the symptoms, risk of the stroke and so on. Treatments for AF include medication, pacemakers, drugs, electrical cardioversion and catheter ablation [11-13].

1.3 Radio-Frequency Catheter Ablation for the Treatment of AF

Radio frequency catheter ablation (RFCA) is a surgical procedure in which heart areas generating abnormal electrical pulses are disabled by means of ablation. RFCA is not being used only for AF, but also for treatment of atrial flutter, ventricular tachycardia (VT), supraventricular tachycardia (SVT), atrioventricular nodal reentrant tachycardia, unifocal atrial tachycardia and also Wolff Parkinson White syndrome (WPW) [14-15].

Before the procedure starts, the patient is prepared under local anesthesia. Long thin wires called catheters then are guided to the heart through the tubes which will be inserted to the body. For triggering and mapping the electrical disturbances of the heart, normally 3-5 catheters will be inserted into the both groins, sometimes into the neck, the elbow or under the collarbone (Figure 3). After the insertion, catheters will be guided to the heart using fluoroscopy imaging. Every electrophysiology laboratory has an X-Ray system which aims to supply fluoroscopy imaging of the heart. In the way towards the left atrium, the catheters cross from the right atrium; here a small puncture hole between the left atrium and the right atrium must be made, allowing the electrophysiologist doctor to perform ablation in the left atrium [16-18].

Once the catheters are in the right place, electrical activities of the heart can be recorded from inside the heart. However it is possible to find parts of the heart which are responsible for electrical disturbances, this task which is called mapping can be done by triggering an electrical disturbance and studying record of this disturbance. Then a particular ablation catheter is maneuvered in such way that an electrode at the tip of the catheter can touch the abnormal tissue [16-18].

Once the catheters are positioned in the right place (by using fluoroscopy) and tissues of the heart responsible for electrical disturbances are known, then radio frequency energy will be used to ablate the tissue, this will be done by contacting the tissue with an RF electrode at the tip of the catheter, which in turn makes the tissue to be heated and causes a lesion. For treatment of AF an area of approximately 1 cm is needed to create an isolating line. Efficient contact between the tissue and the electrode plays an important role in success of the operation, while insufficient contact pressure may produce a superficial lesion with no efficient isolating impact; excessive

contact pressure from the other side may puncture wall of the heart or hurt the esophagus. Although overall success rate of radio frequency catheter ablation for VT, SVT, WPW and atrial flutter is roughly 90-95%, but indeed there are some complications, some of them are bleeding, nerve damage, heart attack, stroke, pulmonary vein problems, pericarditis and rarely death (0.1%) [16-18].

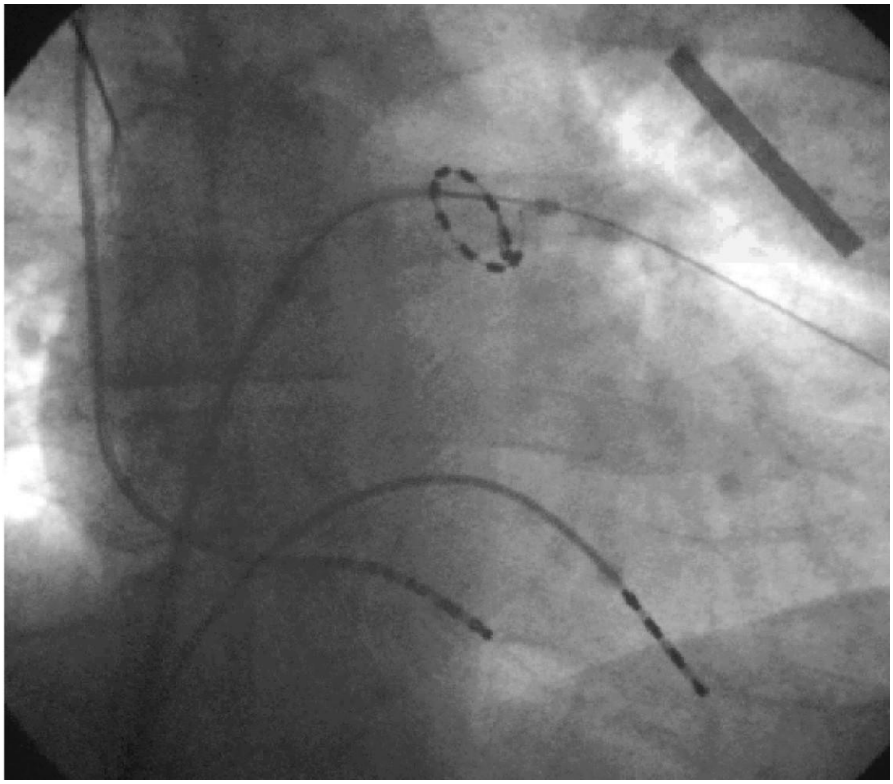

Figure 4. Fluoroscopic view of catheter ablation procedure, reproduced from [33] with permission.

1.3.1 Electroanatomic Mapping Systems

Electroanatomic mapping systems allow electrophysiologists to build a 3D model of the atrium chamber intraoperatively, this is, during the surgical procedure, and without the need of any other imaging modality. This model contains the 3D geometry and electrical properties of the atrium chamber [34-36].

The model is created by acquiring position of a catheter tip when this is in contact with the atrium wall multiple times at different locations. These acquisitions conform a cloud of 3D points that are reconstructed in a 3D mesh in which the electrical properties are mapped, usually in form of color maps. The main advantages of these models are the reduction of the X-Ray exposure and the possibility to avoid registration procedures between pre-opeative images and the intra-operative reality. The created models are used by electrophysiologists to guide the ablation process according to the geometry of the atrium, the position of the catheters and the electrical properties of the tissue [34-36].

Among the electroanatomic mapping systems which allow merging of MRI or CT, CartoMerge™ (Biosense Webster, Diamond Bar, CA, USA) and the NavXFusion™ (St Jude Medical, St. Paul, MN, USA) are being used in AF catheter ablation (Figure 5) [34-36].

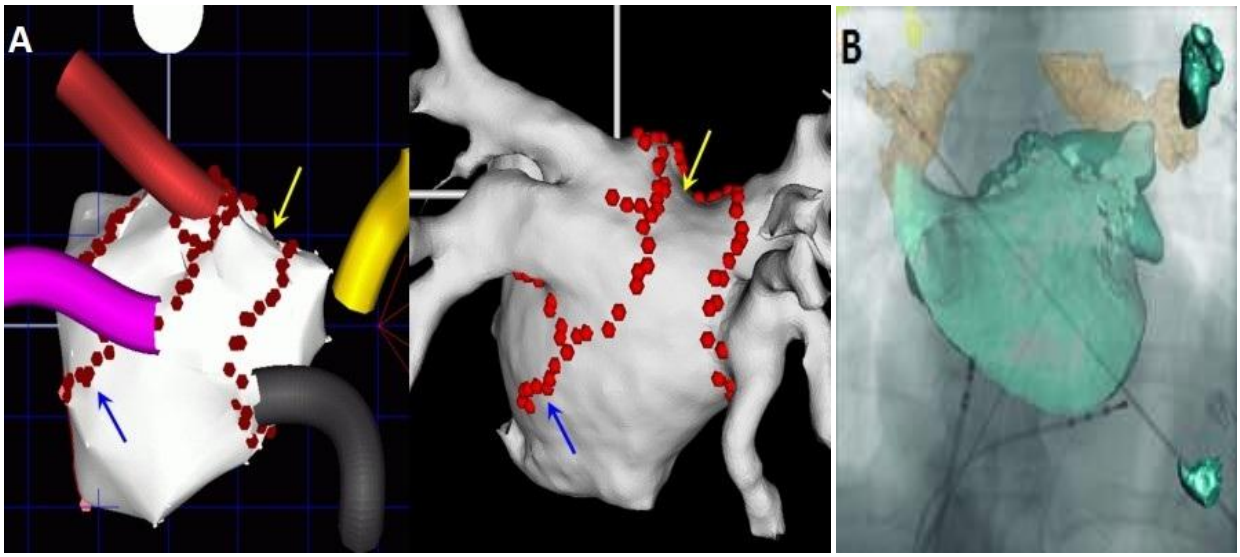

Figure 5. A) Integration of the electroanatomic map of LA with MRI/CT using CartoMergeTM B) a mapping system provided by NavXFusionTM System, reproduced from [20-21] with permission.

CartoMerge™ utilizes electromagnetic tracking to localize catheter inside the body. The system can also guide the catheter tip within the atrium. NavXFusion™ system localizes the catheter tip by using voltage gradients which is made by exterior electric field. CartoSound™ (Biosense Webster) system is an example of integrating intracardiac echocardiography and electroanatomic mapping. This system is supplied by an intracardiac echocardiography probe with a position

sensor which is being tracked by the mapping system. Also integration of fluoroscopy with CT or MRI has been provided by newly developed custom software (Figure 6). The advantage of this method is integration of well detailed images of MRI and CT with the real time images of fluoroscopy. Recent studies have reported the possibility of integrating bi-plane fluoroscopy with MRI and also single plane fluoroscopy with CT [34-36].

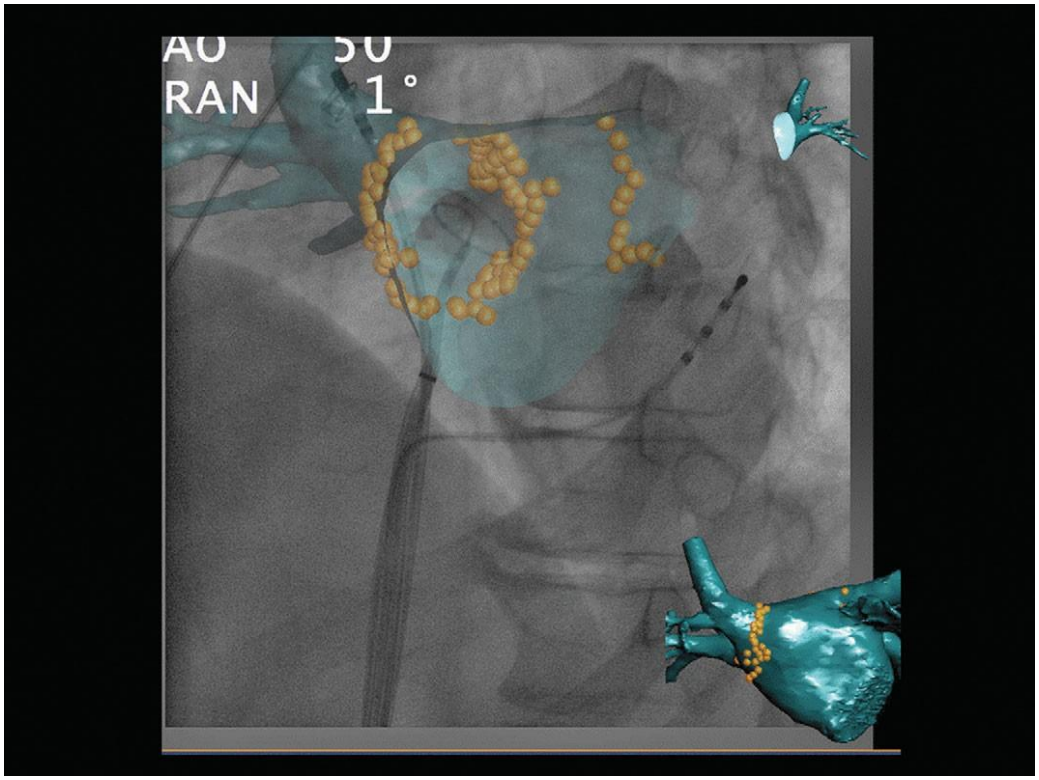

Figure 6. Here a pre-operative CT image of LA is merged with a fluoroscopic image using PhilipsTM CT overlay system, the ablation points in this image has been marked by yellow dots, reproduced from [25] with permission.

1.3.1.1 CartoMerge™

This method utilizes a magnetic coil which is put beneath the operating table. This magnetic coil will be linked to a specialized catheter which is placed within the heart. The magnetic coil beneath the catheterization table is able to detect the catheter tip in 3D space when an intracardiac signal is computed and the system collects the electrical information and the spatial data.

Then the computer simulates a 3D electroanatomic map of the intracardiac chamber which the catheter tip is inside it (Figure 7). Location of the catheter tip inside the mapped space is shown on the monitor that let maneuvering the catheter without using fluoroscopy [34-36].

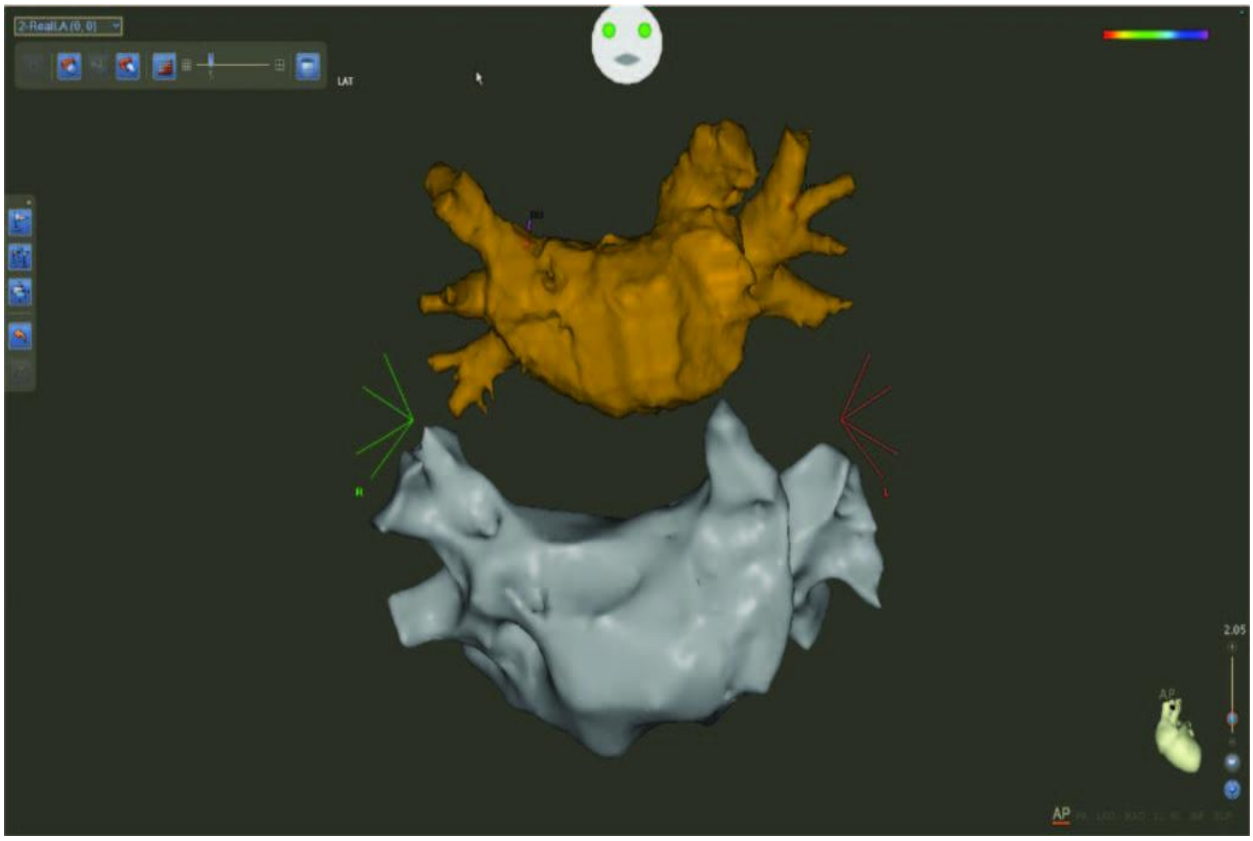

Figure7. Geometry of the LA in the CARTO system, reproduced from [34] with permission.

The paper by L. Gepstein, G. Hayam, and S. A. Ben-Haim, introduces the mapping system which utilizes an external magnetic field emitter [36]. This magnetic coil which is put beneath the cauterization table emits three different ultralow magnetic fields (5 μT to 50 μT). The system also comprises two catheters with miniature magnetic field sensors and a processing unit (CARTO, Biosense). A magnetic field sensor is embedded in a regular electrophysiological 8F deflectable-tip catheter (Cordis-Webster). Figure 8 illustrates the new catheter system and also the procedure for calculating the location of the catheter [34-36].

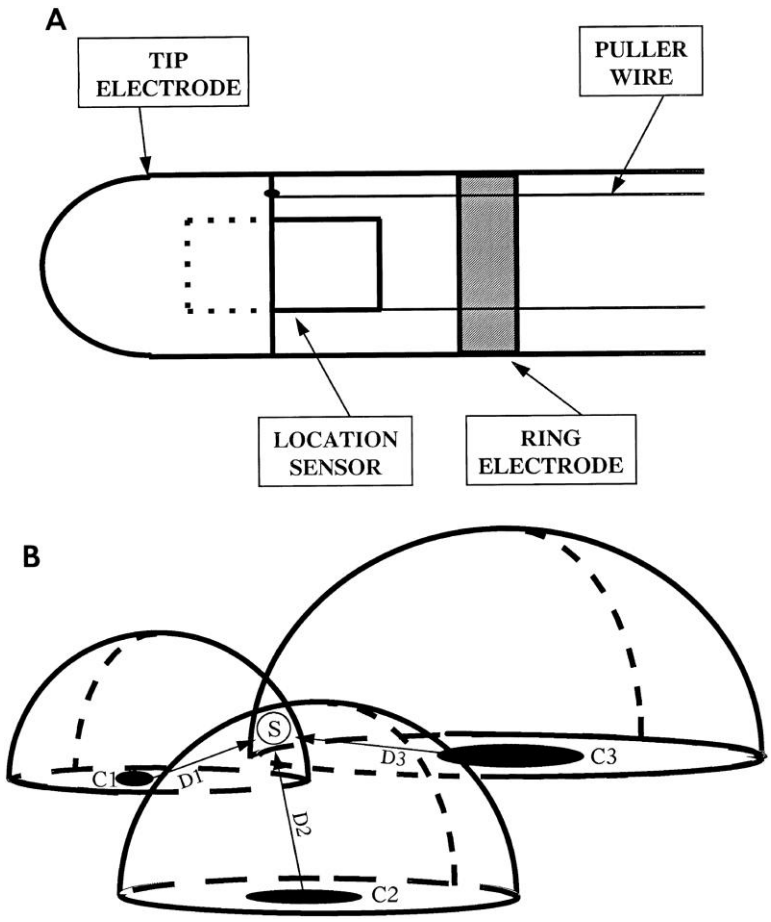

Figure8. A) Design of the new catheter system. B) procedure of calculating the location. A) The catheter consists of tip, ring electrodes and the sensor which all integrated into the catheter. B) 3 coils generate a magnetic field; this magnetic field decays as the distance from the coils increases. The sensor is responsible for computing intensity of this magnetic field. Also it is possible to calculate the distance to each coil [36].

This sensor can provide information about the location and the orientation (x, y, z, roll, pitch, and yaw) of the distal catheter segment. Recording of unipolar or bipolar signals is feasible through the tip electrode and also a proximal ring electrode of the catheter. Hence, based on the location of the catheter tip in the heart, electrophysiological data can be obtained. The second catheter which is called reference catheter is placed in a steady location like in the coronary sinus (CS) or to the back of the patient. Respiration variation or patient movement which alter the intracardiac position slightly, are detectable using this reference catheter. The mapping catheter is inserted in the right atrium and is hauled alongside the endocardium. Fluoroscopic imaging is employed to distinguish the first points [34-36].

It is also possible to reconstruct a real time 3D activation map by successive recording. Local activation time (LAT) at each site is decided from the intracardiac bipolar electrogram. The LAT at each site is calculated in accordance with the fixed intracardiac electrogram acquired from the reference catheter. New points can be joined to the map just if the stability criteria in space and the LAT are fulfilled. Then an operator analyses the signals and brings them into the 3D map if they can be regarded as valid. In order to improve the image, in recent versions of CARTO it has been feasible to integrate variation in impedance (CARTO 3) or real time structural information from intracardiac ultrasound (CartoSound)[34-36].

1.3.1.2 EnSite NavX™

The LocaLisa (Medtronic Inc, St. Paul, MN) system which first was acquired by Endocardial Solutions, Inc. was used in preliminary investigations of non-fluoroscopic procedures. The system then obtained by the St. Jude Medical, Inc. and integrated into the EnSite NavX system (St. Jude Medical, St Paul, MN). In this system patches are located on the skin to trigger an electrical signal; this signal can be felt by the catheters within the body. A reference catheter which is placed in a steady place is used for generating the geometry. The catheter which is used for the ablation purpose is placed and controlled in the chamber; then the contact with the wall is determined by computing the electrical signal and the position of the catheter will be recorded. Variations in electrical impedance which point to change in the position of the catheter can be felt by the system and the new catheter position will be shown in the monitor. The system is capable of tracking 64 distinct electrodes on up to 12 separate catheters at the same time [34-36].

2. Imaging of the Left atrium and Pulmonary veins previous to Catheter Ablation

2.1 Image Modalities

As stated before catheter ablation is considered to be the most convenient way of treating AF when antiarrhythmic drugs have failed. Due to the anatomical variability of the left atrium and the PVs for different patients, precise visualization of these anatomical structures has an important role in obtaining critical information such as 1) number and branch pattern of PVs 2) measurement of PVs ostial diameter 3) LA diameter measurement 4) anatomical understanding of structures like esophagus (to prevent complications such as atrial-esophageal fistula) [19]. Complementing fluoroscopy, there are other image modalities for visualizing the left atrium and the PVs such as Computed Tomography (CT), Magnetic Resonance Imaging (MRI). This imaging modalities are often used together with the model generated during electroanatomical mapping, thus providing a more complete model.

2.2 Image Acquisition

The first step of the image integration process is the image acquisition by means of a CT or MRI. Considering the quality of resulting images of LA and PVs, both the modalities work as the same, but deciding which modality to choose varies between the institutes. Using contrast agent substances helps better distinguishing of blood pool and the borders of the Endocardium (internal part of the atrium chamber) during the segmentation procedure. Using ECG gating method is encouraged, as it enhances the temporal resolution and makes reconstruction of the LA and the PVs images possible at any point in time throughout the cardiac cycle [19].

3. Segmentation of the Left Atrium

3.1 Medical Image Segmentation

Segmentation is the process of dividing an image into smaller parts or regions. Considering one or more features, each divided subset is uniform. Segmentation has a significant role in medical imaging area and is being used extensively in clinical applications. Segmentation in medical imaging refers to the extraction of anatomical structures from 2D/3D medical images.

3.2 Methodology for Segmentation of the Left Atrium

In the case of AF, the regions of interest which are the LA and the PVs will be acquired by some algorithms automatically or semi automatically. The first step for segmenting medical images is to put the CT or MRI data in the electroanatomic mapping system. To set the level threshold accurately, normally a horizontal slice of the desired cardiac chamber will be chosen. Boundaries of different cardiac structures within the slice can be identified by manipulating this threshold. Existence of contrast in the left atrium makes the distinction of the Endocardium and the blood pool easier, since while the blood pool has a high intensity still the Endocardium has a low intensity. Then all pixels of the CT or MRI which are in the range of the level threshold will be labeled, the purpose of image labeling is to make a 3D volume. Then particular seeds are positioned in the center of each region to segment the 3D volume to various structures. Dependent upon the positioning of the seeds and their boundaries, an algorithm will delineate the desired structures automatically. Verification of the segmented volume based on the sagittal slices and 3D reconstructions could be the finalizing step.

3.2.1 Segmentation Algorithms

Cristoforetti et al. 2008, has designed a method to extract the internal surface of the LA and its vessels from high resolution 3D cardiac multi-detector CT [37]. The technique can be divided into two stages. Main principle of the first step was the marker controlled watershed, a mathematical morphology approach which was applied to the gradient magnitude of the actual CT image. In the second step, results of the segmentation in the first step will be used in order to generate a locally variable threshold. This threshold will be used to improve the segmentation somehow to obtain more details. User interaction is needed at the starting point including selection of markers for various classes. There were six classes including the right ventricle, left ventricle, right atrium, left atrium, aortic arch and pulmonary arteries. Then each marker was allocated to one of those classes. Also another marker class was defined corresponded to the background. The results indicate an average of 90% correctly classified voxels and an average border mismatch lower than 1.5 voxels [37].

M Depa et al. 2010, introduces an automatic segmentation method for segmentation of the left atrium by applying weighted voting label fusion and a modified demons registration procedure which is capable of handling images with different intensity distributions [38]. This method is a non-parametric atlas-based procedure based on a label fusion algorithm which utilizes a training set of MRA images. The label fusion algorithm aligns the training set entirely to the test subject image, afterwards merges the weighted votes from training subjects to determine the decision, this will be led to assigning each voxel either to the left atrium or to the background. The important thing is that at each voxel, the votes will be calculated separately, depending not only on similarity between the intensities of the training set and the test subject, but also position of the voxel. However, although the method has a high accuracy but instead the computational time is high [38].

John & Rahn 2005, introduced a method for extracting cardiac structures like the left atrium from the CTA and MRA data sets. This method performs segmentation of the blood pool by simple thresholding, and then the segmented blood pool will be divided into smaller components at narrowings. Finally, those components will be combined to present the heart structures. This approach is robust and fast and it allows the user to enhance the segmentation outcome by marking additional voxels [39].

Koppert, Rongen, Prokop, Romeny and Van Assen 2010, proposed a method for segmentation of endocardial wall followed by segmentation of epicardial wall on CT image data based on active contours, Otsu's multiple threshold method and hysteresis thresholding [40]. Importance of the method is that it considers both endocardial and epicardial wall, as the information about the wall thickness of the heart is extremely important in order to enhance the result of the catheter ablation procedure.

The paper by O. Ecabert et al. 2008 announces an automatic model-based approach for segmentation of the whole heart (including both the atria, both the ventricles and the great vessels) from cardiac CT images. After detecting the heart, three sequent stages are applied in order to extract anatomy of the heart. The mean segmentation error decreases after each step and the total error of all steps is apparently smaller compared to the case of excluding one of the parametric initializations. Point-to-surface error is calculated for each chamber of the heart and the great vessels. According to the authors the overall mean mismatch is 0.7 mm, a 0.70 mm mismatch is reported in the case of the LA boasting, 0.82 mm mismatch for the RA, 0.60 mm mismatch for the PVs and finally 1.32 mm mismatch for the coronary sinuses. The method is fast and helps to accelerate quantitative analysis of cardiac CT images [43].

G. Nollo, A. Cristoforetti, L. Faes, and M. Centonze 2004, introduced a non parametric marker controlled watershed algorithm for segmenting the LA and also PVs from contrast enhanced CT images. The resulting geometrical model then was registered into the CARTO™ electrical maps using a stochastic optimization approach. They achieved a registration precision about 1 mm and a residual registration error about 3 mm [44].

The paper by Karim, Mohiaddin, & Rueckert 2009, presents a procedure for segmentation which uses the voronoi subdivision framework. The method is based on the minimization of a Markov random field based energy functional defined with a spatial and intensity prior [41]. Due to the high variability of the atrial anatomy, this method offers a probabilistic atlas from the training set which enhance the quality of the segmentation. This probabilistic atlas will be created for every anatomical class from the aligned atrial data sets. The result of this method shows a mean overlap (between the manual segmentation and this method) of 70-99 percent for 10 different subjects.

3.2.2 Marker-Controlled Watershed Transformation

Watershed transformation is a common segmentation tool which has an efficient algorithm with no dependency on any parameter. The method was presented firstly by Beucher & Lantuejoul as a geophysical model of rain falling on a terrain. The concept behind it is that rain drops which fall on a surface will be gathered in a minimum from a path which has the steepest descent. A group of points on the surface which guide the drops to the same minimum are called Catchment Basin (CB) and the boundaries between the CBs are known as watershed lines [26]. Now if we consider an image as a terrain and split it up into CBs then it is desired if each CB would include a structure of interest.

The classical approach of watershed segmentation uses an edge detector in order to brighten the borders of the objects, and then applies the watershed transform to the edge image. But due to the noise or typical variations in the surface of the objects, the number of regional minima is always greater than the number of the objects. This means while plenty of watershed lines are situated on important borders but still there are many that don’t, hence this approach is not quite practicable. However it is possible to conquer this condition to some extent by reducing the number of regional minima through applying a threshold or smoothing the image [26].

Beside the numerous advantages of watershed it has also some weak points as well. The main drawbacks of the method are sensitivity to the noise and also over segmentation which leads to a result with a number of unrelated and unwanted regions. By considering some factors it is possible to overcome these limitations and enhance the precision of the result. This can be achieved by defining some markers which hold the information about the quantity and location of each region. The method which is known as Marker-Controlled Watershed segmentation is a vigorous and flexible method of segmenting objects with closed contours, where the borders are indicating the ridges [26].

Generally, there are two approaches for implementation of the Marker-Controlled Watershed Segmentation. The first approach which is minima imposition followed by the regular watershed transform performs a morphological reconstruction by erosion from the desired regional minima. This can help by modifying the topography of the image somehow that the unwanted borders will be removed and only the desired watershed lines will remain.

Here the idea is to multiply the image with an arbitrary mask image to make minima in locations of the image that are of interest. The purpose of using this mask image which is called Marker is to generate one or more minima within every single object of interest. This marker is a connected component consists of one or more voxels [50]. Each marker image must generate more than two minima from which at least one minimum will be employed for segmenting the background. Implementing morphological reconstruction by erosion on the original image by using such a marker image generates a feasible topography for applying the watershed transform. Another approach is to use the Marker-Based Watershed algorithm directly on the input image. In this case, flooding step will be started from the marker provided by the user [26].

4. Integration of the Algorithm into 3D Slicer

4.1 The NA-MIC Kit

The National Alliance of Medical Image Computing (NA-MIC) was founded in September 2004 by the National Institute of Health and it is "a multi-institutional, interdisciplinary team of computer scientist, software engineers and medical investigators who develop computational tools for the analysis and visualization of medical image data" [27]. The NA-MIC kit is an attempt to evolve and set up a group of software and methodologies which aims at medical imaging issues. The purpose of this system is creating a community-based open source milieu which helps the research area. Such a system provides expansion and feedback not only for developers but also for end users. Insight Toolkit (ITK) and 3D Slicer are components of NA-MIC kit which will be introduced in the following parts.

4.1.1 Insight Segmentation and Registration Toolkit (ITK)

ITK is an open source and cross platform system for evolution of segmentation and registration of image analysis programs. It is a library of software tools for image analysis which supplies algorithms for image segmentation and image registration. ITK is implemented in C++ and other programming languages like Python, Java and Tcl are wrapped to it. Using C++ templates, the implementation of ITK utilizes a method so called generic programming. As ITK is an open source software toolkit then developers from all around the world may contribute to development of the project. This will be done by contacting between the members of the community who have the possibility to use, test, debug and maintain the system.

4.1.2 The Visualization Toolkit (VTK)

The Visualization Toolkit (VTK) is an open-source cross platform software targeting modeling, volume rendering, image processing and visualization of 3D images. Although early development of VTK refers to 1993 but since then it has been grown significantly so that nowadays VTK is considered as to be a powerful tool in visualization systems, this has been possible by support and contribution of a large community throughout the world [45]. The library of VTK supplies not only basic image, surface and mesh processing tools, but also numerous sophisticated visualization methods. Implementation of filters, algorithms and data structures in VTK is done through C++ classes and they are also wrapped in other languages like Python, Java and Tcl.

4.1.3 3D Slicer

3D Slicer is an open source software package for image analysis and scientific visualization [28]. 3D Slicer project commenced as a master thesis between the MIT artificial intelligence laboratory and the Surgical planning laboratory at the Brigham and Women's Hospital in 1998 [29]. After its creation the platform of 3D Slicer has been totally altered and it has been developed to a robust application which is being used extensively in clinical research everyday throughout the world. Slicer is a tool for displaying and analyzing multidimensional image data, reconstructing of surfaces and also extracting continuum meshes from CT or MRI, it also provides sophisticated algorithms for functional Magnetic Resonance Imaging (fMRI) and Diffusion Tensor Imaging (DTI). Also in Image-Guided Radiation Therapy (IGRT), Slicer is being used widely in order to build and visualize sets of MRI data which are accessible both pre and intra operatively to let obtaining spatial coordinates for tracing the instrument.

3D Slicer is based on C++ and its application program interface is accessible directly by a python wrapper. The user interface of 3D Slicer is carried through QT and it is also possible to be extended using Python and C++. Also it is possible to add some external modules to the Slicer using a command line interface which is based on an XML file; this XML file has the responsibility for generating a graphical interface inside the Slicer. Figure 9 depicts various abstraction layers of the Slicer graphically.

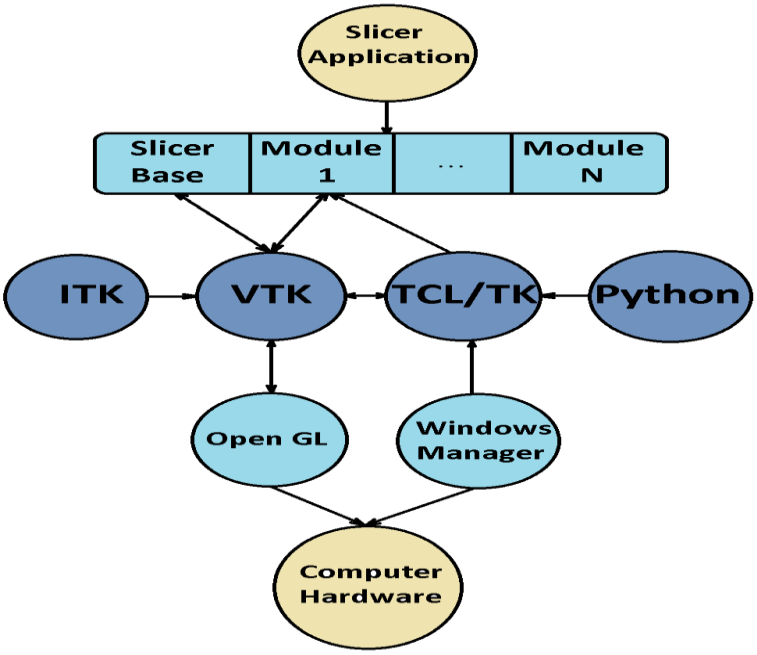

Figure 9. Graphical view of various layers of 3D Slicer.

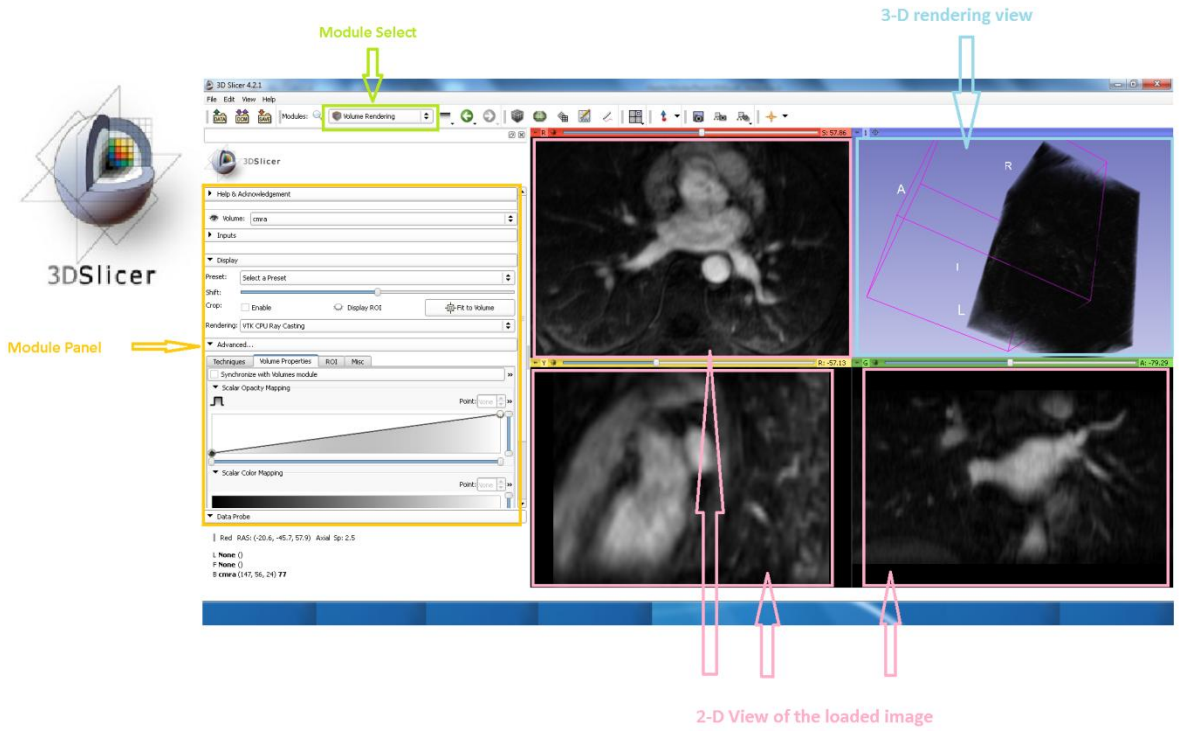

Figure 10.Graphical user interface of the 3D Slicer.

Here an MRI image of the heart is loaded, Volume Rendering is selected as the active module and its panel is shown in the picture, 2-D and 3-D windows are shown also.

4.2 Implementation of the Marker-Controlled Watershed Plugin

The best way of using watershed is to preprocess the image with some filters for example with an edge detector to brighten the boundaries of the image. Therefore we designed a plugin which uses a pipeline consists of three different filters. The first two filters preprocess the input image and then we feed this image into the main algorithm which is the last filter. The first filter in the pipeline is a Gradient Anisotropic Diffusion Filter and then the output of this filter is introduced to the second filter which is a Gradient Magnitude Filter. Finally we feed the output of this filter totally with a label mask into the watershed filter. Figure 11 depicts the pipeline in our method.

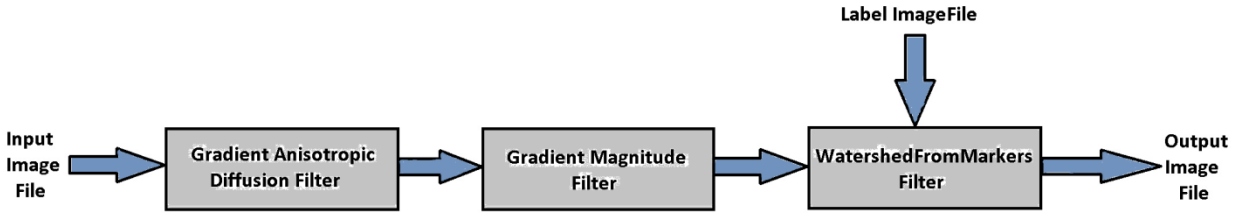

Figure 11. Schematic view of the pipeline.

The algorithm has been written in ITK using C++ templates. The whole procedure can be described as below:

First we define the input, output and label pixel types and then we define their corresponding image types (Label pixel and output pixel types as unsigned char and input pixel type as float). Also we define the dimension of the images which is 3 in our case. The algorithm accepts MR and CT images as the input. The next step is to define 3 pointers for the input and label readers and also for the output writer. Then we define and call the Gradient Anisotropic Diffusion filter and set all required parameters for this filter directly in the source code. The next step is to define and call the Gradient Magnitude filter. We introduce the output of the Gradient Anisotropic Diffusion filter as the input to this filter. Then we define and call the Watershed filter. As mentioned before this filter takes 2 parameters as the input, hence we feed the output of the Gradient Magnitude as the first input and also the label image as the second input to this filter. Using ITK, this filter performs the watershed transformation on whole the input image at once. This means the algorithm will be applied on the whole 3D image, not to the 2D slices. It is equivalent to say that the water will flow using city-block style connectivity which is 4-connectivity in the case of 2D and in our case which is 3D it will be 6-connectivity. Finally the output of this filter will be sent to the output writer and we update the writer.

As stated before, we have designed the pipeline and wrote the algorithm in ITK using C++ templates, then we built the source code using CMake and Visual Studio, after that we created a command line module which works stand alone, but since the target was using this plugin in the 3D Slicer hence we wrapped the module into the 3D Slicer using the built source code and also

an XML file. This XML file has the responsibility of generating a graphical user interface for the module inside 3D Slicer.

4.2.1 Gradient Anisotropic Diffusion Filter

This is a non linear smoothing filter which generates a Gaussian smoothed image. The algorithm reduces noise and unwanted details in the image while preserves particular features like edges. This filter uses three parameters:

- Time step which in general is restricted to be less than 1/2n while the n is the number of dimensions.

- Number of iterations to be performed, as the number of iterations increases the image will be smoothed more and more.

- Conductance that is a function of the gradient magnitude of the image at each point. In fact, sensitivity of the algorithm in preserving the edges is determined by this parameter, as it limits smoothing at the edges. Lower values of the conductance will result in preserving the features of the image to a high extent, while higher values will smooth the features more and more. In general this value depends on the type of the image and the number of iterations but normally the range is between 0.5-2.0.

Figure 12 illustrates the output of this filter applied on a cardiac MRI image as the input.

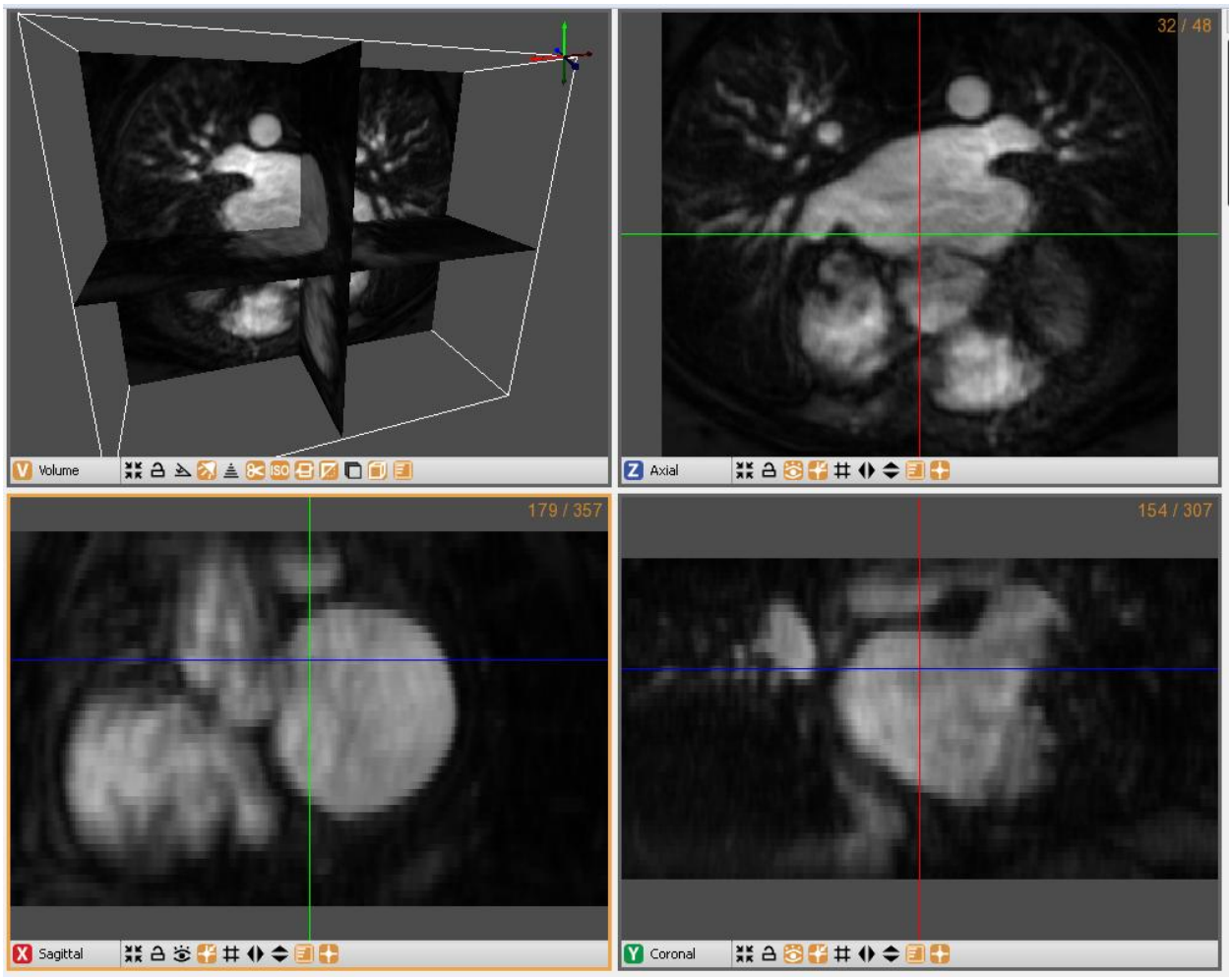

figure 12. Result of applying the Gradient Anisotropic Diffusion Filter on a cardiac MRI image, the output image has been pretty smoothed while the edges have been preserved. Number of iteration is 10 and the conductance is 1.

4.2.2 Gradient Magnitude Filter

This filter is responsible for calculating the gradient magnitude of an image region at each pixel. In the other hand, the main purpose of using such a filter is to determine contours of an object (edge detection) and also to separate homogenous regions in an image. This method calculates the gradient magnitude of an image at each pixel by a simple finite difference method. Considering a 2D image it is equal to convolve the image with some masks like:

-1	0	1

-1
0
1

And then add the sum of their squares and finally calculate the sum's square root. Figure 13 shows the result if we apply the Gradient Magnitude filter on the output of the Gradient Anisotropic Diffusion filter. As we can see borders of the LA are obviously detectable in this image and now we can feed this image into the watershed filter.

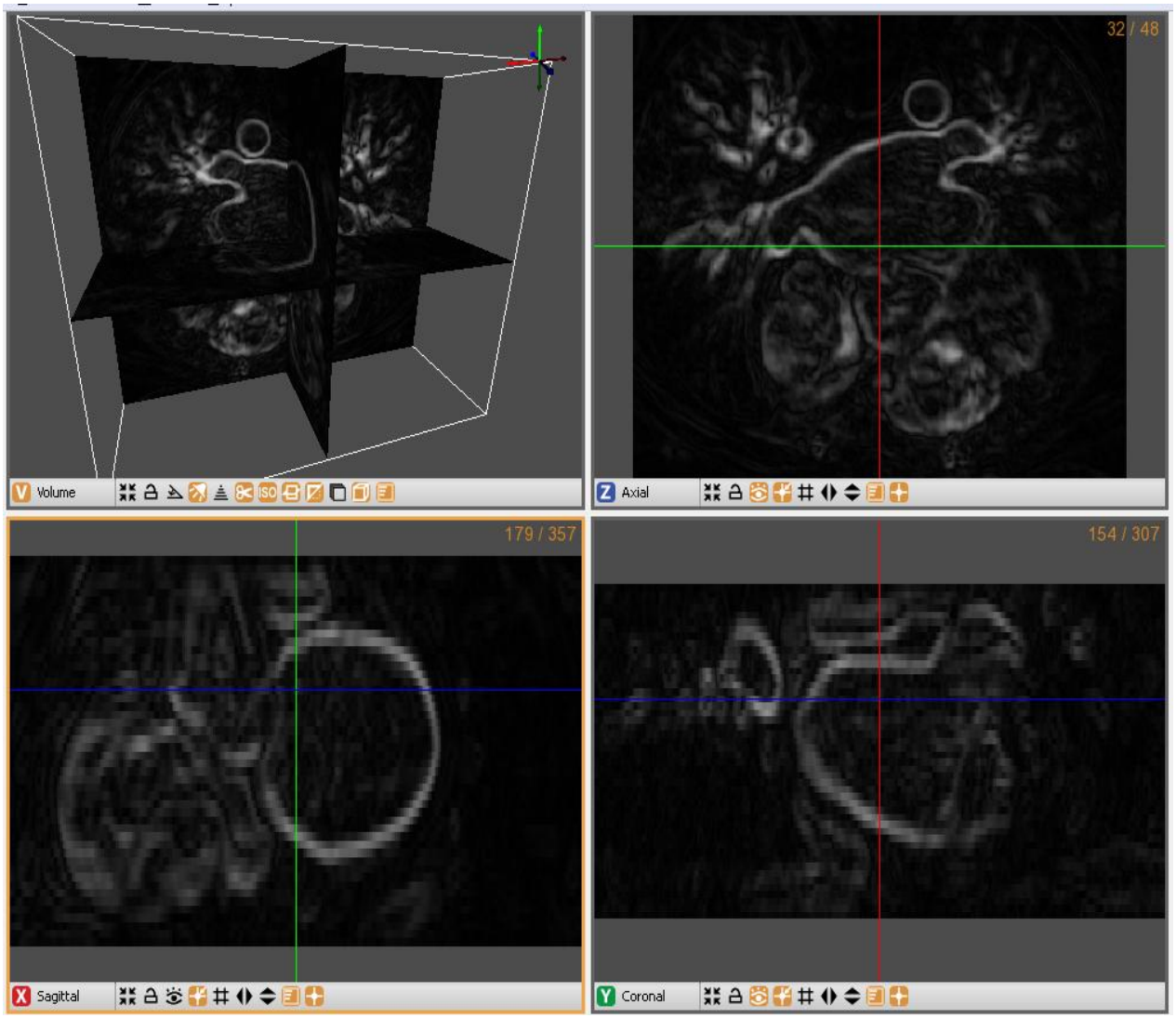

Figure 13. Resulting image after performing two filters (Gradient Anisotropic Diffusion Filter and the Gradient Magnitude Filter).

4.2.3 Marker-Controlled Watershed Filter

As we stated before, the best way of using watershed transformation is preprocessing the image for example with an edge detector to brighten boundaries of the objects and then apply the

watershed on the resulting image. This is why we introduced the result to an edge detector after applying a non linear smoothing filter on the input image. Although theses boundaries will represent the watershed lines but due to the variations in the surface of the objects or even due to the noise there will be more regional minima than the objects. Hence it may happen that some watershed lines will not lie on the corresponding boundaries and we lose some important details. This method uses a label mask (marker image) to overcome this situation. This label mask tags the minima in the input image and assigns a label to each of them. It consists of a seed which is placed roughly mid in the structure of interest. The marker image plays an important role in the output and depending on where you place the seeds the result may vary case to case. As we are interested to the LA then normally we can place the seeds on the LA, RA, RV, LV, superior and inferior vena cava and also the aorta. Figure 14 depicts a label mask superimposed on a cardiac MRI. Final result of the Marker-Controlled Watershed segmentation is shown on figure 15.

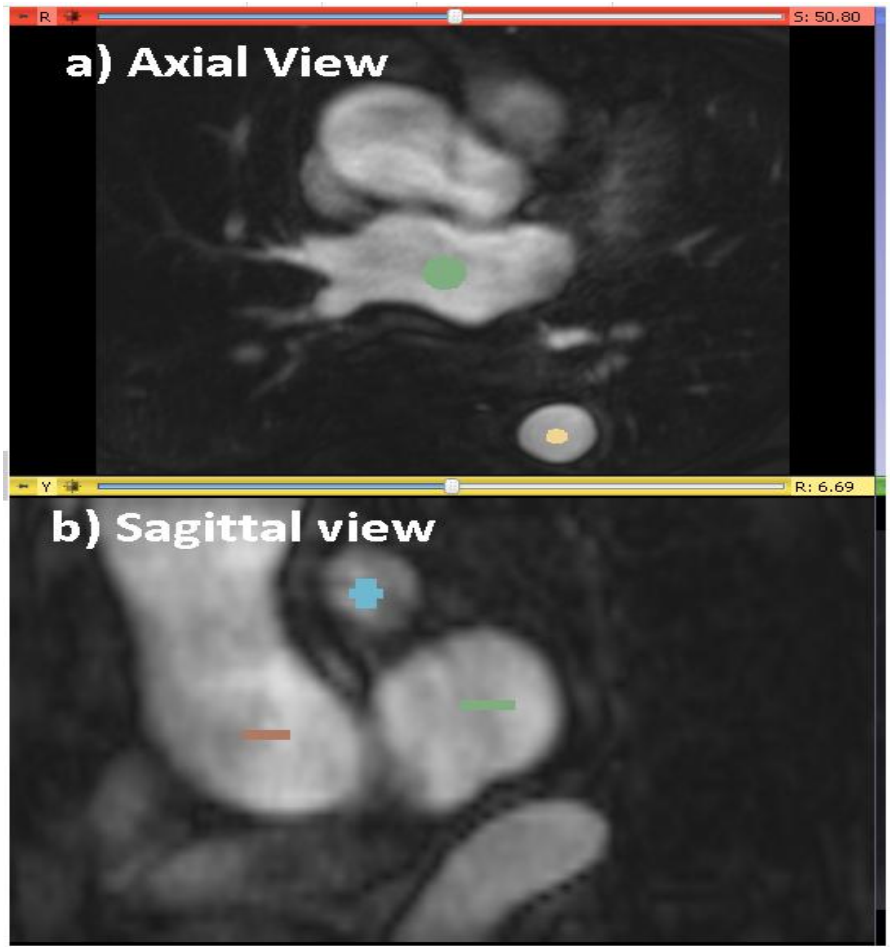

Figure 14. Patch of seeds placed on the LA, RA, Descending and Ascending Aorta. The label mask is superimposed on a cardiac MRI.

The algorithm can perform the watershed transformation based on the Meyer algorithm [46] or based on the Beucher algorithm [47]. These two algorithms are really close to each other, except that in Meyer algorithm the watershed lines are marked in the output image while in the Beucher algorithm they are not. We used the Beucher algorithm in our method. The main steps of the Beucher algorithm can be described as follow:

- The first step is to write the marker image (*M*) to the output image. Then all pixels of the marker image (*p*) with their neighbors will be put in a priority queue with their corresponding priority level *I[p]*.

- In the next step pixels with the highest priority level will be extracted from the priority queue and then the label of *p* grows towards all the pixels neighboring the marker *p* which are not labeled yet. The limit for adding unlabeled neighbors *q* with the priority level *I[q]* into the priority queue is that whether *I[q]* is greater than *I[p]* or at least as the same. So the priority queue contains the pixels bordering the growing regions.

Implementation of the Beucher algorithm has been demonstrated in the next page also.

Implementation of the Beucher algorithm:

1) initialization step

queue ← ***0***

for each *p* ∈ ***M***

do
- Copy the marker image to the output image
- ***O****[p]* ← ***M****[p]*
- Put the edges of the marker in the queue
- **if** ***M****[p]* ≠ *WSLABEL*
- **then**
  - *bgNeighbor* ← **false**
  - **for each** *q* ∈ ***N***(p)
  - **do**
    - **if** ***M****[q]* = *WSLABEL*
    - **then** *bgNeighbor* ← **true**
  - **if** *bgNeighbor*
  - **then** *queue* ***I****[p]* ← *queue* ***I****[p]]* ∪ *{p}*

2) flooding step

while *queue* ≠ 0

do
- *v* ← *FIRST (queue)*
- **while** *queue [v]* ≠ 0
- **do**
  - *p* ← *FIRST (queue [v])*
  - **for each** *q* ∈ ***N***(p)
  - **do**
    - **if** ***O*** *[q]* = *WSLABEL*
    - **do**
      - ***O*** *[q]* ← ***O*** *[p]*
      - **then**
        - *v* ← MAX *(****I*** *[q], v)*
        - *queue[v]* ← *queue[v]* ∪ *{q}*

Abbrv & Functions	Stands for
I	Input Image
M	Marker Image
O	Output Image
P	Marker pixels
Q	Unlabeled neighbor pixels
bgNeighbor	Background Neighbor
WSLABEL	A label to define background and watershed pixels
FIRST(queue)	Extracts the highest priority element from the queue
Max	Returns the max element
N(p)	Returns the list of p's neighbors

Table 1. Description of the abbreviations used in the Beucher algorithm above.

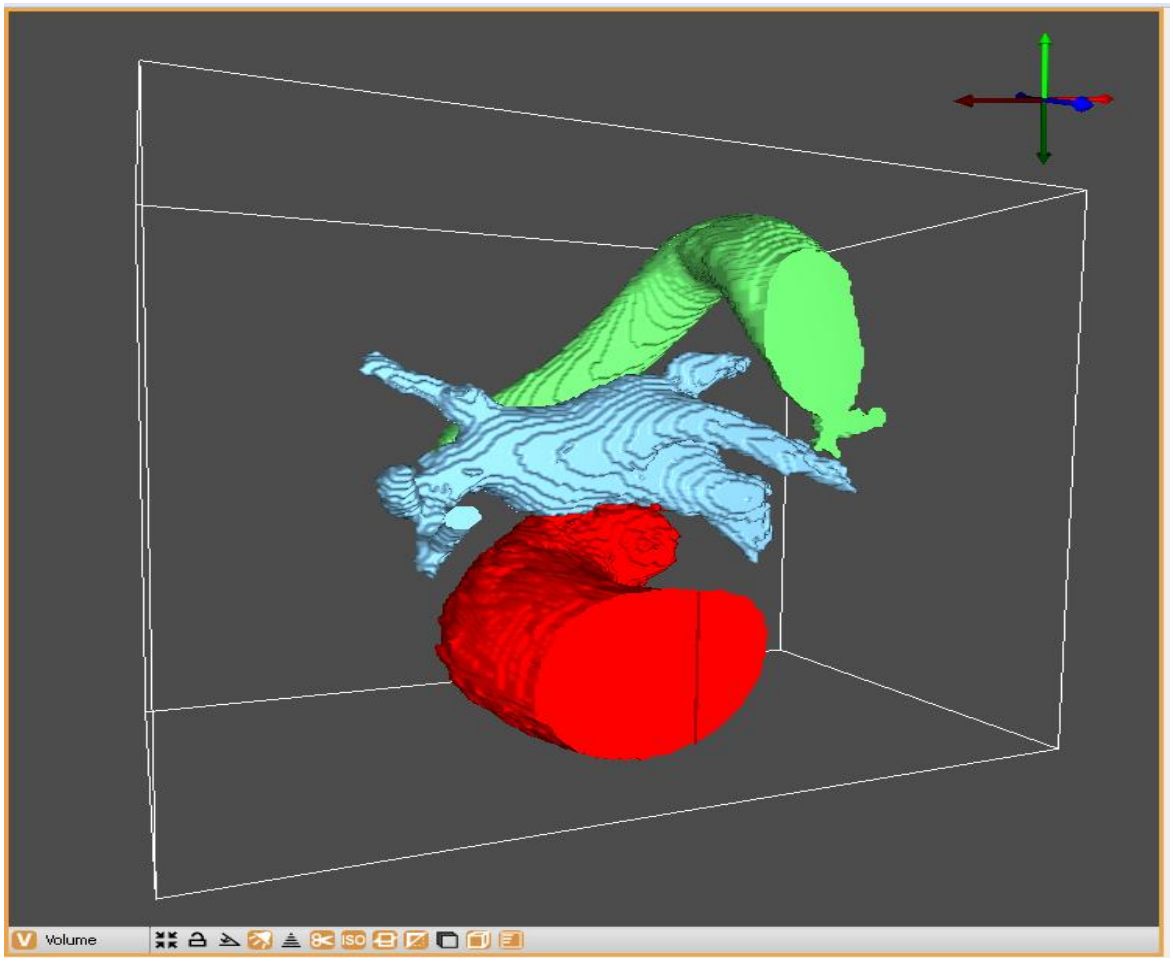

Figure 15.Result of the Marker-Controlled Watershed segmentation. The seeds were placed on the LA, Ascending Aorta (AAo) and Descending Aorta (DAo). While the blue label indicates the LA, the red and green labels indicate the Dao and AAo.

5. Empirical Evaluation

Segmentation is performed on a data set consists of 12 images were obtained from MIDAS provided by Comprehensive Arrhythmia Research and Management Center (CARMA) for exclusive use of the NA-MIC members [49]. These image datasets were late-gadolinium enhanced MRI-images (LGE-MRI) of the patients prior to undergo the radio frequency catheter ablation. LGE-MRI scans were obtained on either a 1.5 Tesla Avanto or a 3.0 Tesla Verio clinical scanner (Siemens Medical Solutions, Erlangen, Germany). The scan was acquired 15 minutes following contrast agent injection (0.1 mmol/kg, Multihance [Bracco Diagnostic Inc., Princeton, NJ]) using a 3D inversion recovery, respiration navigated, ECG-gated, gradient echo pulse sequence. Typical acquisition parameters were: free-breathing using navigator gating, a transverse imaging volume with voxel size = 1.25 × 1.25 × 2.5 mm (reconstructed to 0.625 × 0.625 × 1.25 mm), repetition time (TR)/echo time (TE) = 5.4/2.3 ms, flip angle=20 degrees, inversion time (TI) = 270 - 310 ms, and GRAPPA with R = 2 and 46 reference lines. ECG gating was used to acquire a small subset of phase encoding views during the diastolic phase of the LA cardiac cycle. The time interval between the R-peak of the ECG and the start of data acquisition was defined using the cine images of the LA. The TI value for the LGE-MRI scan was identified using a scout scan [49]. Also each data set consists of a ground-truth image (manual segmentation) produced using the Corview software [49]. We used these ground truth images to compare the results of the Marker-Controlled Watershed segmentation with them.

The methodology for the segmentation consists of two phases. The first step which was producing the marker image could be performed either in the 3D Slicer or any other software like Seg3D which has an editor toolbox. The procedure was loading the image and then labeling structures of interest each with a unique label. In the case of LA, the most important structures for labeling could be the LA itself, LV, RA, ascending and descending aorta. The background does not need to be labeled and it will be labeled automatically with 0. All the other labels had an integer value greater than 0. If the labeling was done in the 3D Slicer then it could be used directly in the Maker-Controlled Watershed plugin inside the Slicer, otherwise we should save the label image (marker image) and then load it totally with the input image on the module inside the Slicer. Figure 16 shows the user interface of the module inside the 3D Slicer.

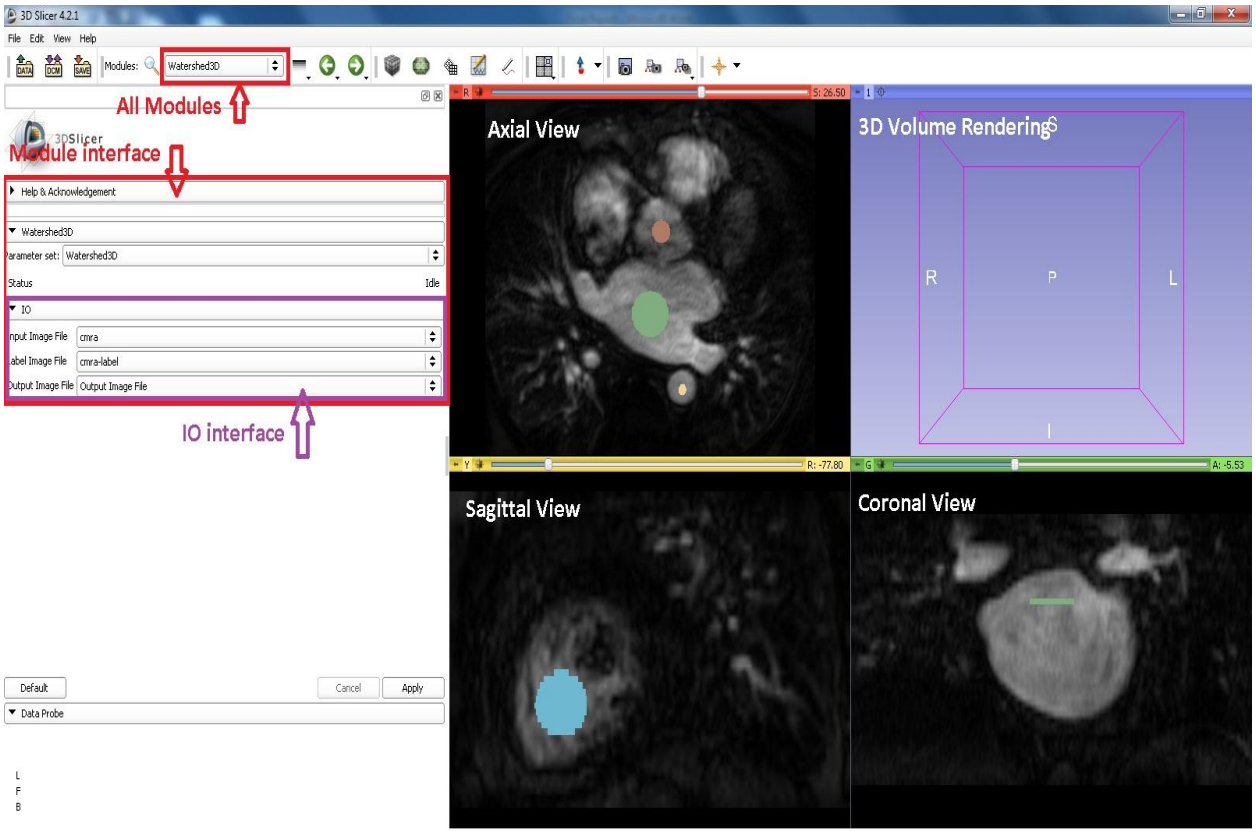

Figure 16. User Interface of the Marker-Control Watershed Segmentation inside the 3D Slicer.

In order to decrease the computational time, we cut the input image since the provided LGE-MRI images consists of areas around the heart which did not need to be segmented. Hence, we cut the input image first and then produce the label mask based on the edited image and finally load both the images in the module inside the 3D Slicer. The last step was to select the output image and run the plugin. We should emphasize that parameters of the Gradient Anisotropic Diffusion filter are only accessible from the source code, not in the module. This means that in the case of changing each parameter we had to rebuild the source code again to see the effect of the changes. What we have experienced in this method is that the result of the segmentation relies on 3 important factors:

- Number of iterations in the Gradient Anisotropic Diffusion filter
- Conductance parameter in the Gradient Anisotropic Diffusion filter
- Marker image

This means that in the case of an undesired result we had to change each of these three parameters to finally get the best result. Generally, the number of iterations ranges from 5-20, and also the conductance ranges from 0.1 till 2.

Table 2 summarizes information regarding the volumes obtained through the Marker-Controlled Watershed method compared to the ground truth images.

	Volume (mm^3)		
Dataset ID	Watershed Segmentation	Ground truth image	Estimated Error
72	73665	76426	- 3.61%
154	130285	95774	+36.03%
254	109320	82279	+32.86%
440	221743	181642	+22.08%
606	117809	117439	+0.31%
886	58649	44381	+32.14%
937	97470	79985	+21.86%
969	191731	163504	+17.26%
996	122937	112156	+9.61%
1063	107785	84511	+27.53%
1092	129363	95920	+34.86%
1133	79339	60390	+31.37%

Table 2 . Comparison between the volumes obtained by our method vs. ground truth. (–) sign in the estimated error implies undersegmentation of the LA, while (+) sign implies oversegmentation of the LA.

Also table 3 summarizes more statistics regarding the results consist of the mean estimated error, standard deviation of the estimated error and 95% confidence interval.

Mean Estimated Error	**Standard Deviation**	**95% confidence interval**
22.46	**12.37**	**15.46 ~ 29.46**

Table 3. Statistics of the results in more detailed. (Volumetric information)

Furthermore we have tried to visualize the results in order to find points of the LA that have the most effect on the errors. We used a VTK class to compute the Hausdorff Distance between the watershed segmentation with their corresponding ground truth image. VTK Hausdorff Distance is an accurate method for measuring the distance between sets of points as it measures the point to cell distance instead of point to point distance [48]. It is in fact a 3D reconstruction of the Marker-Controlled Watershed result versus the corresponding ground truth image as the reference. Consider S_1 and S_2 to be 2D surfaces that are embedded in R^3 and consider p_1 as a point which belongs to S_1. Then a surface to surface relative distance $(\Delta\ (S_1, S_2))$ can be defined as follow:

$$\delta\ (S_1, S_2) = \sup_{p_1 \in S_1} \delta\ (p_1, S_2) \quad (1)$$

As the distance is not symmetrical we call it relative and it means: $\Delta\ (S_1, S_2) \neq \Delta\ (S_2, S_1)$. Then the Hausdorff distance (d) between S_1, S_2 can be described as the maximum of the two relative distances:

$$d\ (S_1, S_2) = \max\ \{\Delta(\ S_1, S_2), \Delta(\ S_2, S_1)\} \quad (2)$$

"The algorithm takes 2 inputs, $input_A$ on the port 0 and $input_B$ on the port 1. Then the inputs will be copied to corresponding output ports and it computes the Hausdorff Distance $d(input_A\ ,\ input_B\ )$ and the relative distance $\Delta\ (input_A\ ,\ input_B\ )$ and $\Delta\ (input_B\ ,\ input_A\ )$.Although the mathematical definition of the Hausdorff Distance refers to R^3 surfaces but the algorithm allows comparisons between point sets. The user decides which element from the compared object should be targeted, points or cells. The point to cell distance implies the existence of cells in both inputs. When such a method is used, the point to surface δ computation performs a geometric interpolation of the targeted cells and this leads to a more precise distance calculation"[48]. Figure 17 illustrates the point to cell computation method considering the distance of a sphere S inscribed in a cube C.

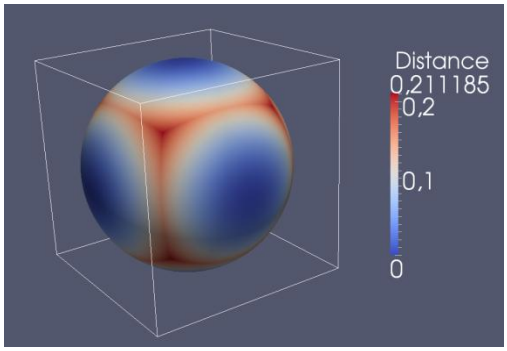

Figure 17. Point to cell computation method. [48]
Δ(S, C) = 0.211, Δ(C, S) = 0.366, d(C, S) = 0.366

Figure 18 shows the Hausdorff Distance between two datasets, ground truth image as the reference versus the result of the watershed segmentation as the reconstruction. We have selected the number 154 which has roughly the biggest error among the other datasets. Detailed results of all the other results can be found in Appendix B.

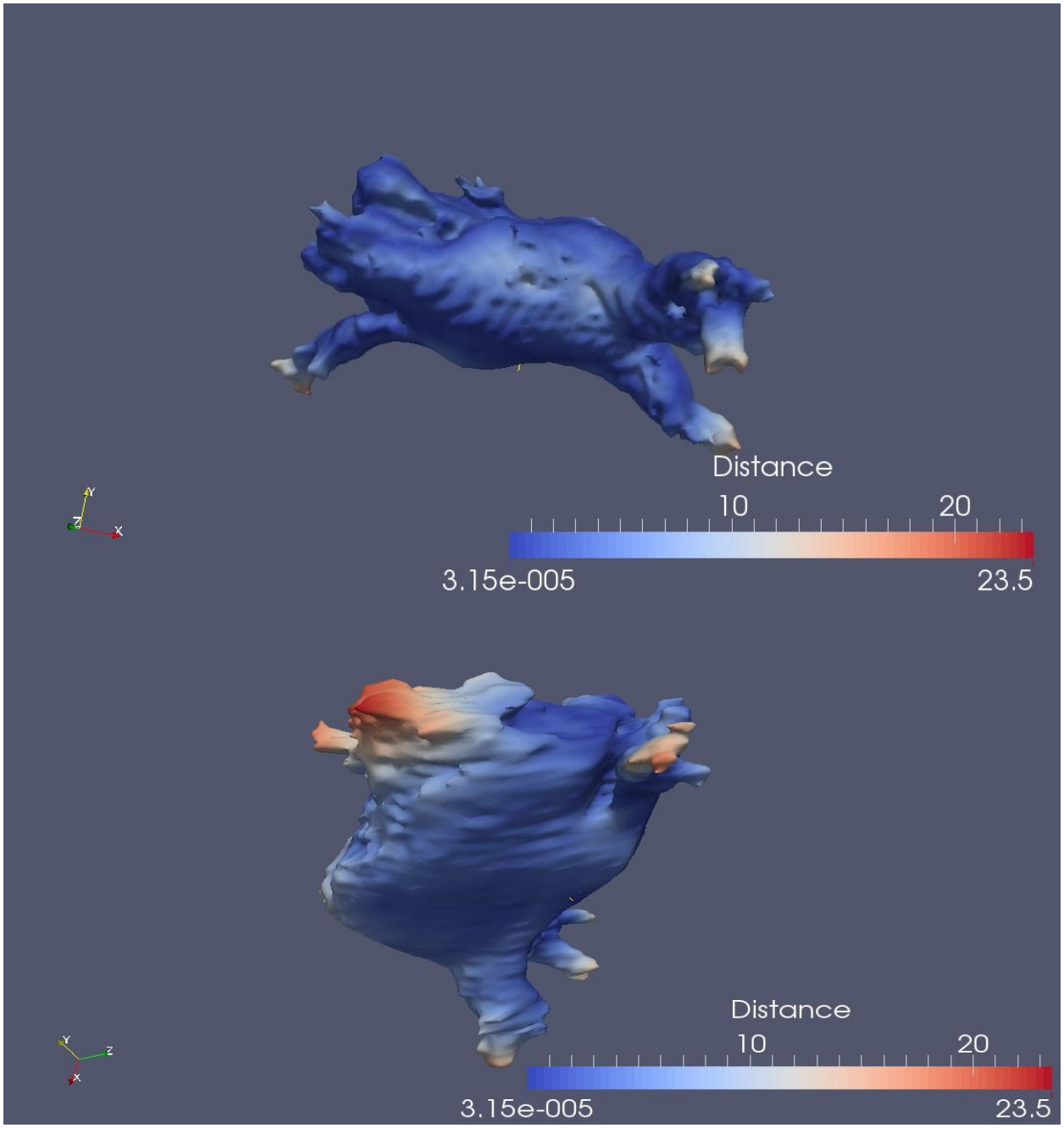

Figure 18 . Visualizing the error between the ground truth and the Marker-Controlled Watershed segmentation by the Hausdorff Distance method. The picture presents a group of point to set distances, visualized in Paraview from 2 different angles. (Distances are in mm)

What can be interpreted from these two images is that the maximum overlap between points of two datasets occurs in the body of the LA and the minimum overlap comes from the pulmonary veins and the part of the LA where it connects to the LV. While the dark blue color indicates the minimum distance between points of two datasets (maximum overlap) which is roughly 3.15e-005 mm, the dark red color indicates the maximum distance (minimum overlap) between points of two data sets which here is about 23 mm.

Furthermore we present the figure 19 which is the histogram of the VTK Hausdorff Distance algorithm. This histogram has been derived from the point to set distances for each point in the Marker-Based Watershed segmentation to its corresponding ground truth image. In another hand it shows the distribution of the points have been segmented correctly (with the distance near 0 mm between two datasets), until 9 mm distance between points of two datasets which indicates reduction in the overlap.

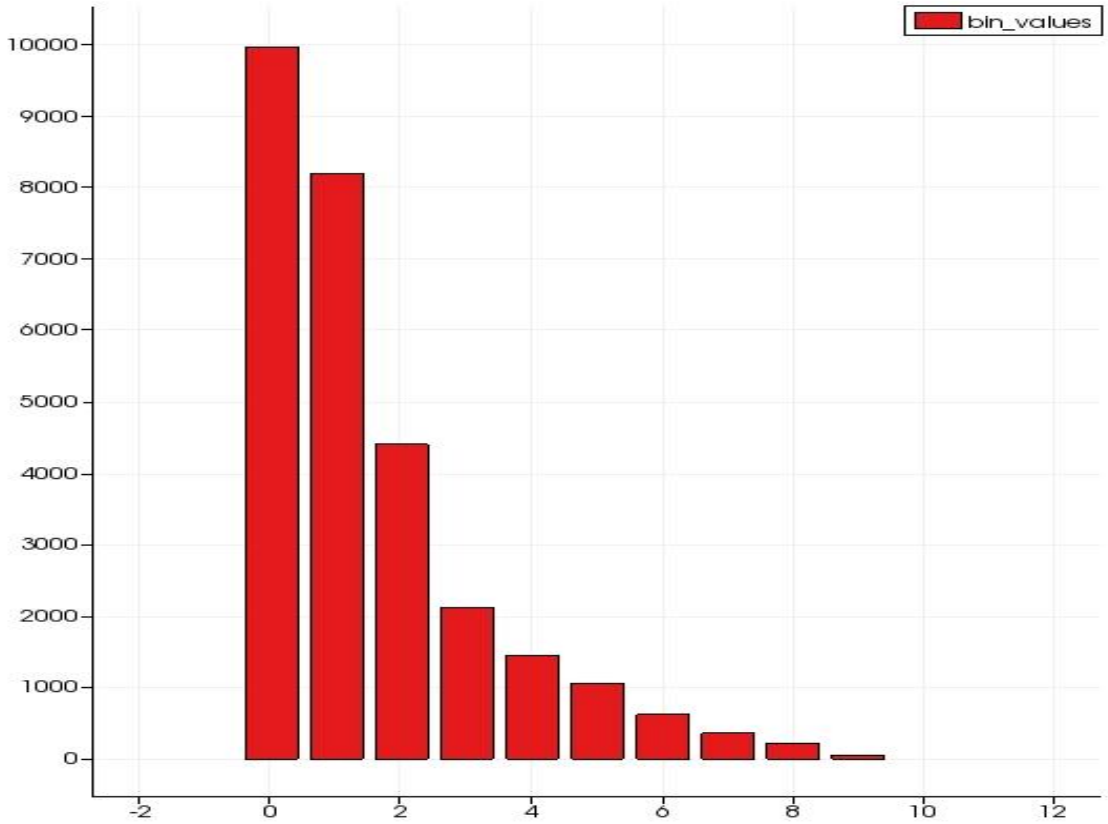

Figure 19 . Histogram of the Hausdorff Distance. It describes amounts of the points in two datasets have the distance 0 (points of two data sets are completely overlapped) until 9 (minimum overlap between points of two datasets).
(While X-axis shows the distance in mm, the Y-axis shows total amount of the points)

6. Discussion

Segmentations were done on a 32 bit Windows machine with an Intel(R) Core(TM) 2 due 2.4 GHz CPU with 4 GB of RAM and depending the number of iterations each single segmentation took about 3-6 minutes (3 minutes for 5 times of iteration and 6 for 10 times). The best results were obtained by the conductance term 1, except one dataset that showed a better result with conductance term 0.1. Half of the results were obtained by 10 times of iteration while the other half by 5 times of iterations. These two factors are mainly dependent on the contrast of the input image. Generally as the contrast decreases we need more iterations and less conductance to reach to an accepted result. The other important factor which affects the result considerably is the marker image that you select. Two different marker images may result in two different outputs. This is highly tricky where to place the seeds. In some cases due to the high contrast of the image it is possible to get a good result by placing the seeds only on the LA. But in other cases you may have to place the seeds on other structures like the RA, LV and aorta. Otherwise this may lead to leakage of other structures into the LA. The most probable cause of the leakage that was experienced in this method is the LV (oversegmenting the LA). Figure 20 depicts this leakage obviously.

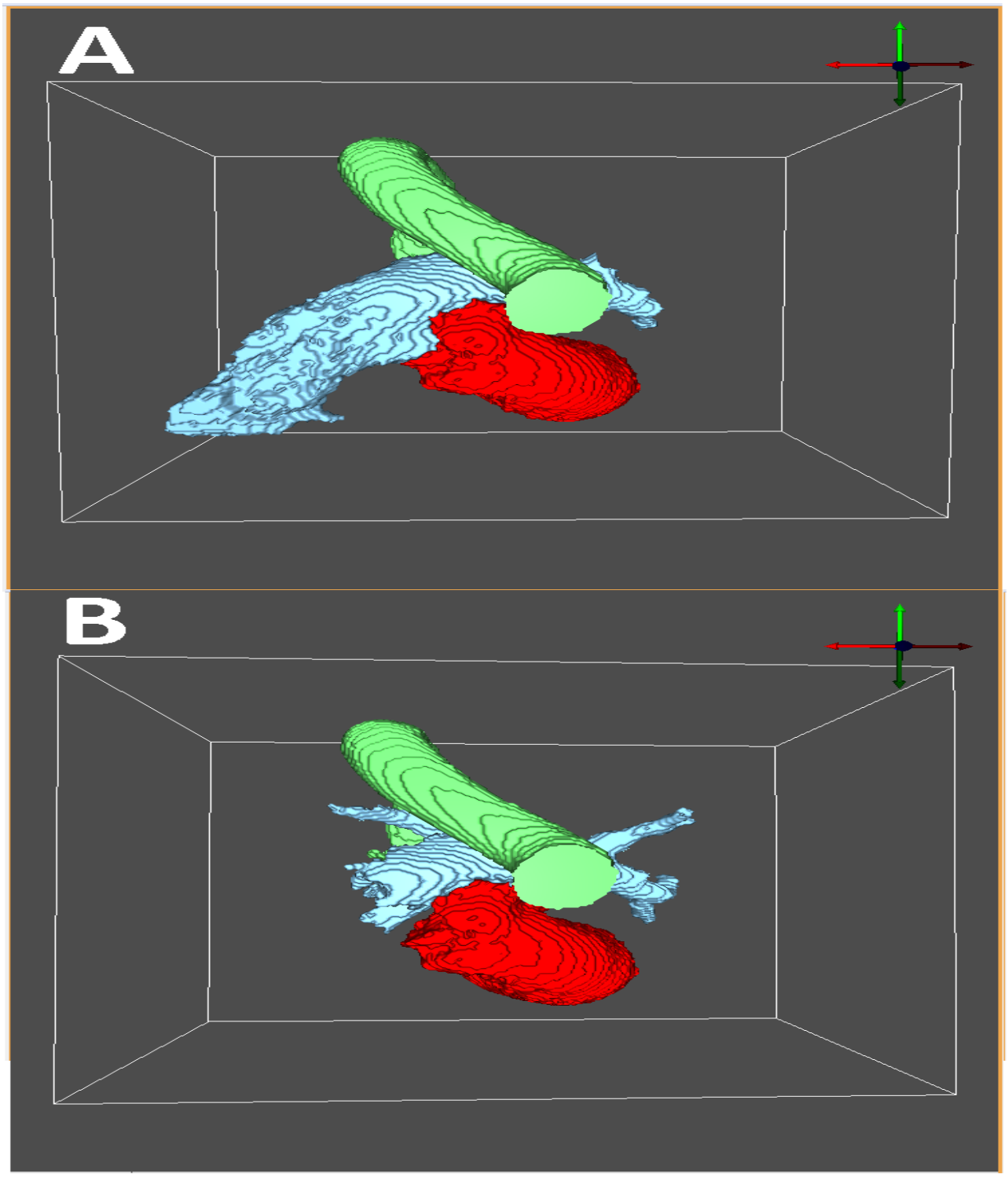

Figure 20 . Oversegmentation of the LA in figure A is obvious compared to figure B.

According to the results and looking through table 2 we can find that the method tends to oversegmentation. Referring to figure 18 we can find parts of the LA that have the oversegmenting issue and it is obvious that this issue arises from:

- Bottom of the LA where it connects to the LV
- Pulmonary veins

What we have experienced in this method is that due to the high variability of the LA it is really hard to segment the area between the LA and the LV completely true. But this is mainly dependent on the shape of the LA, LV and also the contrast of the image, as we have got some precise results as well (complete database of the results can be found in appendix A and B). This means that in the case of poor contrast in the image we will lose some important boundaries in the gradient magnitude image; hence there is no watershed line where it should be to stop growing the pixels belong to a specific marker (label) and it causes the oversegmentation. For instance according to figure 18 we can see there is roughly 20 mm difference between the two datasets (ground truth and watershed segmentation) in the area where the LA connects to the LV. To find out more about the source of this issue we used figure 21 which is the output of the dataset 254 after passing through the Gradient Anisotropic Diffusion and then Gradient Magnitude filter .We selected this image as it showed the maximum estimated error between all the other datasets. This figure clearly illustrates deformation of the LA and overlapping the LV and the LA beginning from the slice number 3. This is solely due to the poor contrast of the image. Also, this must be noticed that we did not observer such a condition on all the datasets, but this situation happened only on those datasets with a low contrast or an odd shape of the LA.

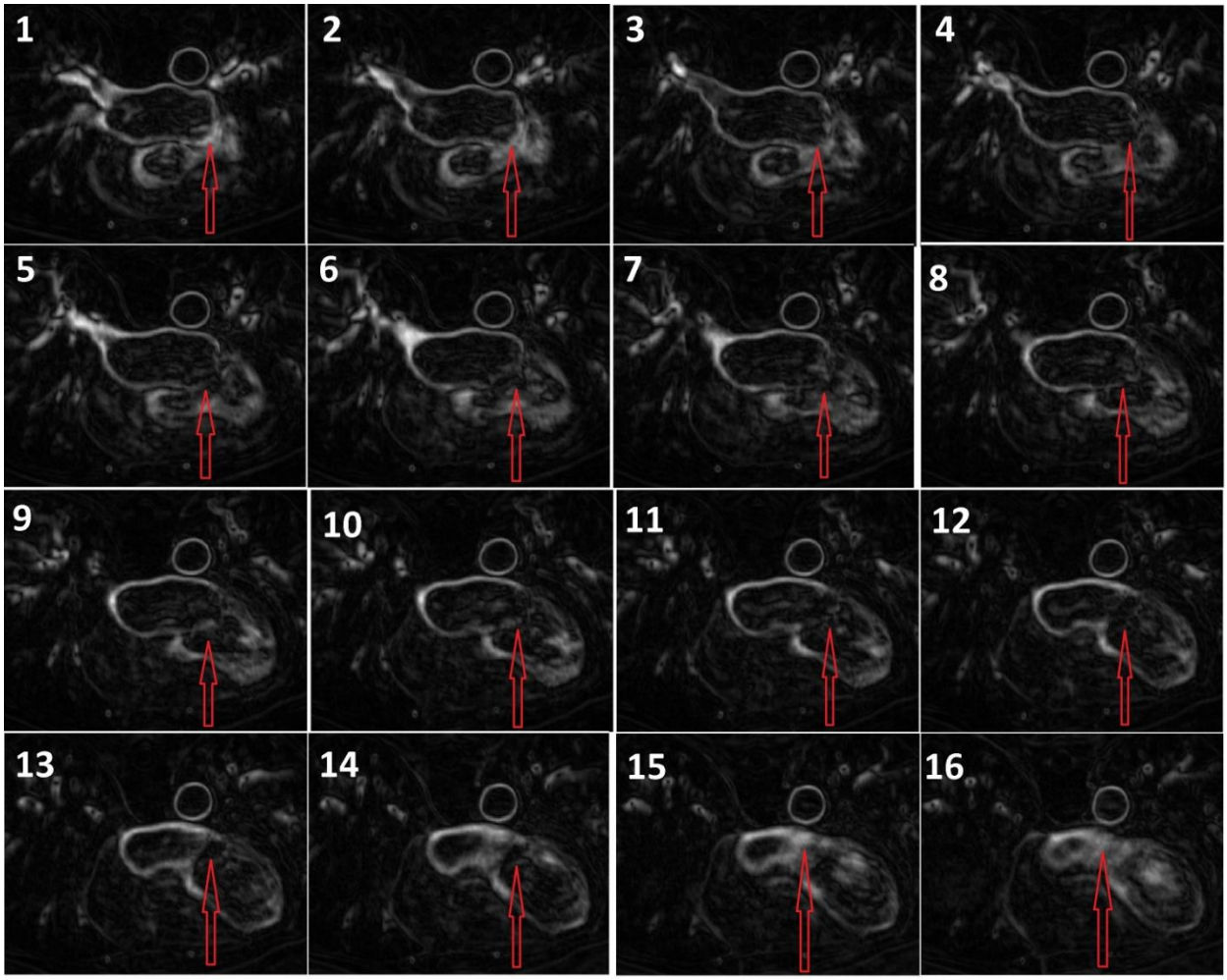

Figure 21. Deformation of the LA and Leakage of the LV into the LA which has the greatest effect on the estimated error is illustrated.

The other issue was the pulmonary veins that have a great effect on the error rate, but not considerable as the LV. Although parts of the pulmonary veins in junction of the LA are segmented truly but we have also continuation of the pulmonary veins segmented (oversegmenting the pulmonary veins). While in the ground truth image we can observe that only a small portion of the pulmonary veins have been segmented. Figure 18 depicted that the corresponding error is considerably smaller than the error in the area between the LA and the LV (roughly 12-15 mm). But this is really important as the RFCA is performed at the pulmonary vein ostia. However, as we can see in figure 18 the majority of this error comes from distal part of the pulmonary veins.

Finally, in order to compare the results of our method with other existing methods, we have tried to present the result of other methods in table 4. We have to mention that the accuracy measures used in those methods are different compared to our method and since we did not have any direct way of comparing our results with them, then this could be the subject of future research.

Paper	Modality	Description	Validation
(Cristoforetti et al., 2008) [37]	CT	Watershed of external morphological gradient then variable threshold surface extraction	90% of voxels correctly classified Border mismatch < 1.2 mm
(O. Ecabert et al., 2008) [43]	CT	Active Shape Model	Mismatch < 0.82 mm in heart chambers; < 1.32 in great vessels
(M Depa et al., 2010)[38]	MRA	Weighted voting label fusion +demons registration	Dice 92%, PV 84%
(C. Lorenz & J. v Berg, 2005) [42]	CT	Shape Model	Mismatch < 5 mm
(Karim et al.,2009 - 2010) [41]	CE-MRA	Voronoi subdivision framework + Markov Random Field	Correct Overlap of 0.70 till 0.99

Table 4. Results of other existing methods for segmenting the LA or whole the cardiac chambers.

7. Conclusion

Segmentation of the LA is beneficial not only for pre-operative assessment of cardiac chambers of the patients who will undergo the RFCA, but also for outcome evaluation of the operation. Nevertheless, due to high variability of the LA it has been always a challenging task among the experts. Several methods have been proposed so far to conquer this limitation. Here we prsented a method for segmenting the LA and its PVs based on the Marker-Controlled Watershed Segmentation. The main object of the thesis was to design and implement a plugin to do the segmentation inside the 3D Slicer. In order to achieve this, we designed a plugin consist of a pipeline with three different filters. For enhancing the quality and precision of the result, we preprocessed the image first with a non linear smoothing filter to remove the noise and unwanted details, while still preserves the most important structures of the image, i.e. edges. Then we applied an edge detector on the smoothed image to get the boundaries of the objects more clear and finally we applied the watershed on the resulting image. After designation of the pipeline we wrote the source code of the pipeline in ITK using C++ templates. Then we built the source code using CMake and Visual Studio and made a command line module for the algorithm which although works stand alone, but as the target was using the plugin inside the 3D Slicer we wrapped the command line module to the 3D Slicer using the source code and an XML file which has the responsibility for generating an user interface for the module inside the 3D Slicer.

Segmentation performed on a data set consists of 12 LGE-MRI images provided by Comprehensive Arrhythmia Research and Management Center. The data set provided us a ground-truth image for each single image which we used them to compare results of our method with them. Also we have used a VTK Hausdorff Distance algorithm to validate our results.

Considering the time of the segmentation, as we stated before the method is pretty fast compared to other methods. Considering the performance of the method and according to the results based on the VTK Hausdorff Distance algorithm we can say that the method is robust and powerful in segmenting the body of the LA and the pulmonary vein Ostia. As the VTK Hausdorff Distance algorithm proves 3.79e-004 to 8.28e-005 distance between two datasets (ground truth image and marker-controlled watershed result) in those areas for all datasets. But the weakness of the algorithm is oversegmenting the LA in the junction of the LV and also distally in the pulmonary veins area. We have to indicate that the oversegmentation issue did not observe on all the images but in most of them. Looking through the output of the Gradient Magnitude filter we found that the issue arises from the poor and low contrast of the input MRI images. This means that in the case of poor contrast of the input image we will lose some important boundaries in the gradient magnitude image; hence there is no watershed line where it should be to stop growing the pixels belong to a specific marker (label) and it causes the oversegmentation.

Future work may either focus on enhancement of the performance by solving some issues like the contrast of the input image or performing the method automatically. Although the segmentation is done automatically but still we need a user to define the marker image according the shape of the input image. Using some morphological operations or Hough transform the process of choosing a marker image may be achieved automatically in the near future.

8. Bibliography

[1] "CDC - DHDSP - Heart Disease Facts." [Online].
Available: http://www.cdc.gov/heartdisease/facts.htm. [Accessed: 14-Apr-2012].

[2] "What Is the Heart? - NHLBI, NIH." [Online].
Available: http://www.nhlbi.nih.gov/health/health-topics/topics/hhw/.
[Accessed: 14-Apr-2012].

[3] "The Heart (Human Anatomy): Diagram, Definition, Location in the Body, and Heart Problems." [Online]. Available: http://www.webmd.com/heart/picture-of-the-heart.
[Accessed: 14-Apr-2012].

[4] "Anatomy of the Heart - NHLBI, NIH." [Online].
Available: http://www.nhlbi.nih.gov/health/health-topics/topics/hhw/anatomy.html.
[Accessed: 14-Apr-2012].

[5] "Human Heart: Anatomy, Function & Facts | LiveScience." [Online].
Available: http://www.livescience.com/34655-human-heart.html. [Accessed: 14-Apr-2012].

[6] "An Overview of the Heart's Chambers and Valves." [Online].
Available: http://heartdisease.about.com/cs/starthere/a/chambersvalves.htm.
[Accessed: 14-Apr-2012].

[7] "Conduction System of the Heart." [Online].
Available: http://emedicine.medscape.com/article/1922987-overview.
[Accessed: 14-Apr-2012].

[8] "The Heart's Electrical System." [Online].
Available: http://www.bostonscientific.com/lifebeat-online/heart-smart/electrical-system.html. [Accessed: 14-Apr-2012].

[9] "Atrial Fibrillation." [Online].
Available: http://emedicine.medscape.com/article/151066-overview.
[Accessed: 14-Apr2012].

[10] "Atrial Fibrillation (AF). Symptoms and Treatments | Patient.co.uk." [Online].
Available: http://www.patient.co.uk/health/atrial-fibrillation-leaflet.
[Accessed: 14-Apr-2012].

[11] "Atrial Fibrillation - Treatment - NHS Choices," 30-Nov-2011. [Online].
Available: http://www.nhs.uk/Conditions/Atrial-fibrillation/Pages/Treatment.aspx.
[Accessed:03-Oct-2012].

[12] "Treatment for Atrial Fibrillation." [Online]. Available: http://www.medicalnewstoday.com/info/atrial-fibrillation/treatment-for-atrial-fibrillation.php. [Accessed: 03-Oct-2012].

[13] "Atrial fibrillation: Treatments and drugs - MayoClinic.com." [Online]. Available: http://www.mayoclinic.com/health/atrial-fibrillation/DS00291/DSECTION=treatments-and drugs. [Accessed: 03-Oct-2012].

[14] "How Is Atrial Fibrillation Treated? - NHLBI, NIH." [Online]. Available: http://www.nhlbi.nih.gov/health/health-topics/topics/af/treatment.html. [Accessed: 04-Oct-2012].

[15] "Treatment for Atrial Fibrillation." [Online]. Available: http://www.medicalnewstoday.com/info/atrial-fibrillation/treatment-for-atrial-fibrillation.php.[Accessed: 03-Oct-2012].

[16] "Radiofrequency catheter ablation for atrial fibrillation." [Online]. Available: http://www.webmd.com/heart-disease/atrial-fibrillation/radiofrequency-catheter-ablation-for-atrial-fibrillation. [Accessed: 05-Oct-2012].

[17] "An explanation of radio frequency catheter ablation." [Online]. Available: http://www.c-r-y.org.uk/radio_frequency_catheter_ablation.htm. [Accessed: 05-Oct-2012].

[18] "Catheter Ablation of Atrial Fibrillation." [Online]. Available: http://circ.ahajournals.org/content/113/13/e666.full. [Accessed: 05-Oct-2012].

[19] W. Thai, B. Wai, and Q. a Truong, "Preprocedural imaging for patients with atrial fibrillation and heart failure," Current cardiology reports, vol. 14, no. 5, pp. 584–92, Oct. 2012.

[20] M. Wright, "Electrophysiology Enhanced Imaging Modalities in Atrial Fibrillation," pp. 54–57, 2010.

[21] R. Kabra, "Recent Trends in Imaging for Atrial Fibrillation Ablation," vol. 10, no. 5, pp. 215–227, 2010.

[22] J. Ector, S. De Buck, J. Adams, S. Dymarkowski, J. Bogaert, F. Maes, and H. Heidbüchel, "Cardiac three-dimensional magnetic resonance imaging and fluoroscopy merging: a new approach for electroanatomic mapping to assist catheter ablation," Circulation, vol. 112, no. 24, pp. 3769–76, Dec. 2005.

[23] J. Sra, D. Krum, A. Malloy, M. Vass, B. Belanger, E. Soubelet, R. Vaillant, and M. Akhtar, "Registration of three-dimensional left atrial computed tomographic images with projection images obtained using fluoroscopy," Circulation, vol. 112, no. 24, pp. 3763–8, Dec. 2005.

[24] J. Sra, G. Narayan, D. Krum, A. Malloy, R. Cooley, A. Bhatia, A. Dhala, Z. Blanck, V. Nangia, and M. Akhtar, "Computed tomography-fluoroscopy image integration-guided catheter ablation of atrial fibrillation," Journal of cardiovascular electrophysiology, vol. 18, no. 4, pp. 409–14, Apr. 2007.

[25] S. Knecht, I. Nault, M. Wright, S. Matsuo, N. Lellouche, P. E. Somasundaram, M. D. O'Neill, K.-T. Lim, F. Sacher, A. Deplagne, P. Bordachar, M. Hocini, J. Clémenty, M. Haïssaguerre, and P. Jaïs, "Imaging in catheter ablation for atrial fibrillation: enhancing the clinician's view," Europace : European pacing, arrhythmias, and cardiac electrophysiology : journal of the working groups on cardiac pacing, arrhythmias, and cardiac cellular electrophysiology of the European Society of Cardiology, vol. 10 Suppl 3, pp. iii2–7, Nov. 2008.

[26] J. Roerdink and A. Meijster, "The watershed transform: definitions, algorithms and parallelization strategies," Fundamenta Informaticae, vol. 41, pp. 1–40, 2000.

[27] "National Alliance for Medical Image Computing." [Online]. Available: http://www.na-mic.org/. [Accessed: 10-Oct-2012].

[28] S. Pieper, M. Halle, and R. Kikinis, "3D Slicer," 2004 2nd IEEE International Symposium on Biomedical Imaging: Macro to Nano (IEEE Cat No. 04EX821), vol. 2, pp. 632–635, 2004.

[29] D. Gering, "A system for surgical planning and guidance using image fusion and interventional MR," Master's Thesis, Massachusetts Institute of Technology, Department of Electrical Engineering and Computer Science, 1999.

[30] "AtrialFibrillation." [Online]. Available: http://www.strokesurvivors.ca/new/AtrialFibrillation.php. [Accessed: 15-Oct-2012].

[31] "Anatomy of the human heart." [Online]. Available: http://www. http://healthinformation1.4arabs.com/heart/2.html. [Accessed: 3-Oct-2012].

[32] "Heart Conduction System," Medical Education for Undergraduate MD Students. [Online]. Available: http://mdmedicine.wordpress.com/2011/04/24/heart-conduction-system/. [Accessed: 3-Oct-2012].

[33] S. Spitzer and L. Karolyi, "Catheter ablation of atrial fibrillation–Current status and future directions," Applied Cardiopulmonary Pathophysiology 13: 291-299, pp. 291–299, 2009.

[34] G. M. Mcdaniel, "The Use of Electroanatomic Mapping Systems to Reduce Fluoroscopic Exposure in Pediatric Ablations," vol. 2, no. November, pp. 551–556, 2011.

[35] C. Reithmann and E. Hoffmann, “Electroanatomical mapping for visualization of atrial activation in patients with incisional atrial tachycardias,” European heart journal, pp. 237–246, 2001.

[36] L. Gepstein, G. Hayam, and S. A. Ben-Haim, “A Novel Method for Nonfluoroscopic Catheter-Based Electroanatomical Mapping of the Heart In Vitro and In Vivo Accuracy Results,” Circulation, vol. 95, no. 6, pp. 1611–1622, Mar. 1997.

[37] A. Cristoforetti, L. Faes, F. Ravelli, M. Centonze, M. Del Greco, R. Antolini, and G. Nollo, “Isolation of the left atrial surface from cardiac multi-detector CT images based on marker controlled watershed segmentation,” Medical Engineering & Physics, vol. 30, no. 1, pp. 48–58, Jan. 2008.

[38] M. Depa, M. Sabuncu, and G. Holmvang, “Robust atlas-based segmentation of highly variable anatomy: left atrium segmentation,” Statistical Atlases and Computational Models of the Heart: Mapping Structure and Function, pp. 85–94, 2010.

[39] M. John and N. Rahn, “Automatic left atrium segmentation by cutting the blood pool at narrowings,” Medical image computing and computer-assisted intervention : MICCAI' 05 Proceedings of the 8th international conference on Medical image computing and computer-assisted intervention, vol. 8, no. Pt 2, pp. 798–805, Jan. 2005.

[40] M. M. J. Koppert, P. M. J. Rongen, M. Prokop, B. M. H. Romeny, H. C. V. Assen, and P. Healthcare, “Cardiac Left Atrium CT Image Segmentation for Ablation Guidance,” Dept. of Biomedical Engineering , Eindhoven University of Technology , Netherlands, pp. 480–483, 2010.

[41] R. Karim and C. Juli, “Automatic segmentation of left atrial geometry from contrast-enhanced magnetic resonance images using a probabilistic atlas,” Statistical Atlases and computational models of the heart, and international conference on Cardiac electrophysiological simulation challenge, pp. 134-143, 2010.

[42] C. Lorenz and J. Von Berg, “Towards a comprehensive geometric model of the heart,” Functional Imaging and Modeling of the Heart, pp. 102–112, 2005.

[43] O. Ecabert, J. Peters, H. Schramm, C. Lorenz, J. von Berg, M. J. Walker, M. Vembar, M. E. Olszewski, K. Subramanyan, G. Lavi, and J. Weese, “Automatic model-based segmentation of the heart in CT images,” IEEE transactions on medical imaging, vol. 27, no. 9, pp. 1189–201, Sep. 2008.

[44] G. Nollo, A. Cristoforetti, L. Faes, and M. Centonze, “Registration and Fusion of Segmented Left Atrium CT Images with CARTO Electrical Maps for the Ablative Treatment of Atrial Fibrillation,” Department of Physics , University of Trento , Italy Radiology Division, S Chiara Hospital Trento , Italy, pp. 345–348, 2004.

[45] W. Schroeder, K. Martin, B. Lorensen, “Visualization Toolkit: An Object-Oriented pproach to 3D Graphics,” 4th Edition, Kitware, December 1, 2006.

[46] S. Beucher and F. Meyer. “Mathematical Morphology in Image Processing, chapter 12: The Morphological Approach to Segmentation: The Watershed Transformation,” pp.433–481, Marcel Dekker Inc., 1993.

[47] S. Beucher and C. Lantuejoul. “Use of watersheds in contour detection,” In Proc. Int. Workshop Image Processing, Real-Time Edge and Motion Detection/Estimation, 1979.

[48] F. Commandeur, J. Velut, and O. Acosta, “A VTK Algorithm for the Computation of the Hausdorff Distance,” The VTK Journal, pp. 1–6, 2011.

[49] “MIDAS - Collection NAMIC - CARMA Left Atrial MRI.” [Online]. Available: http://www.insight-journal.org/midas/collection/view/197. [Accessed: 10-Mar-2012].

[50] P. Soille, ”Morphological Image Analysis, Principles and Applications, chapter 9: Segmentation,” . pp. 267-290, 2004.

9. Appendix A

This section comprises the result of the segmentation in our method on all 12 datasets. Figure A depicts the result of Marker-Controlled Watershed segmentation while figure B depicts the ground truth image of the same dataset. The dataset ID of each image is included beside each picture.

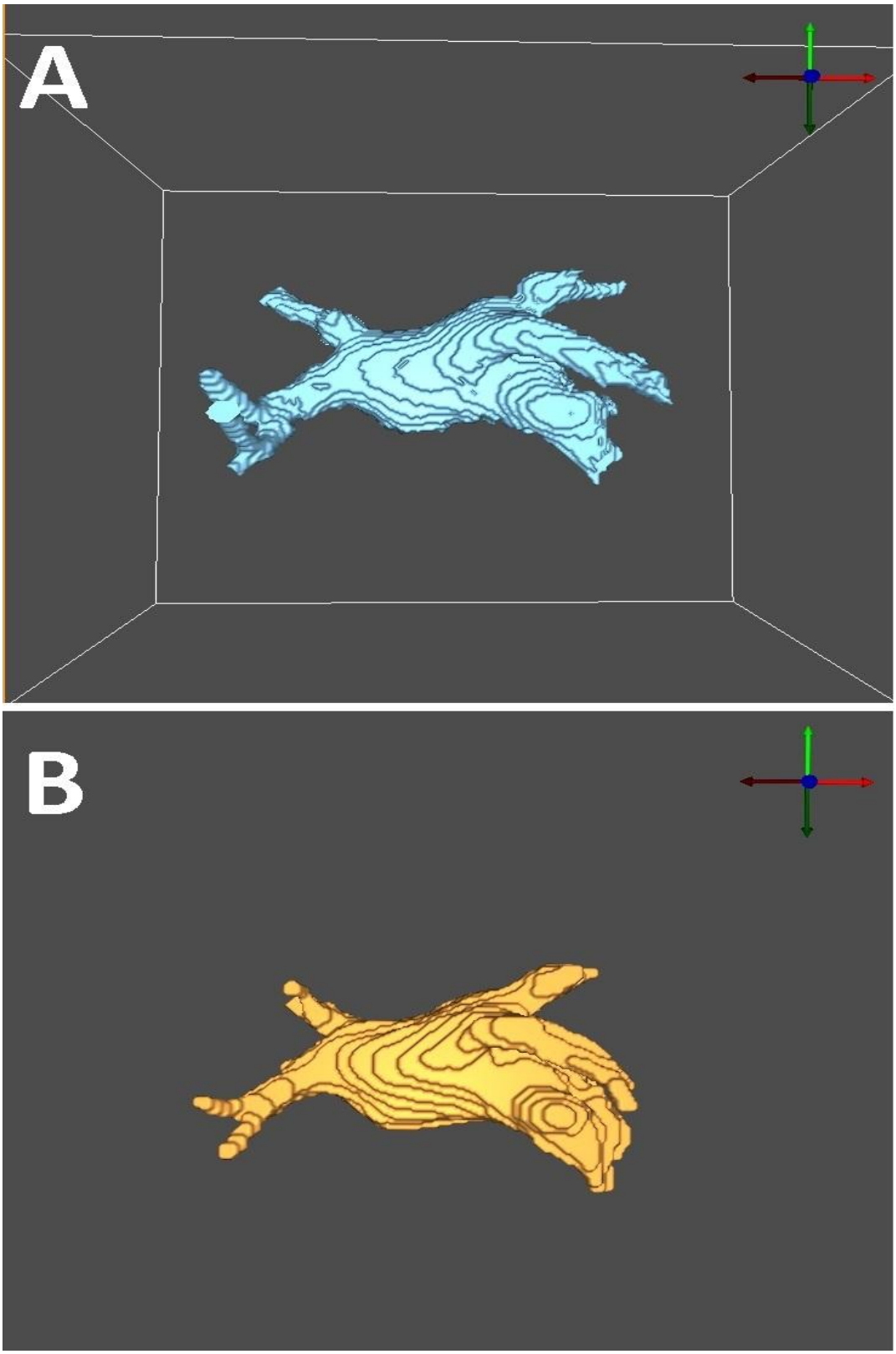

Figure 22. A) Result of Marker-Controlled Watershed Segmentation. B) Corresponding ground-truth image. (Dataset ID : 72)

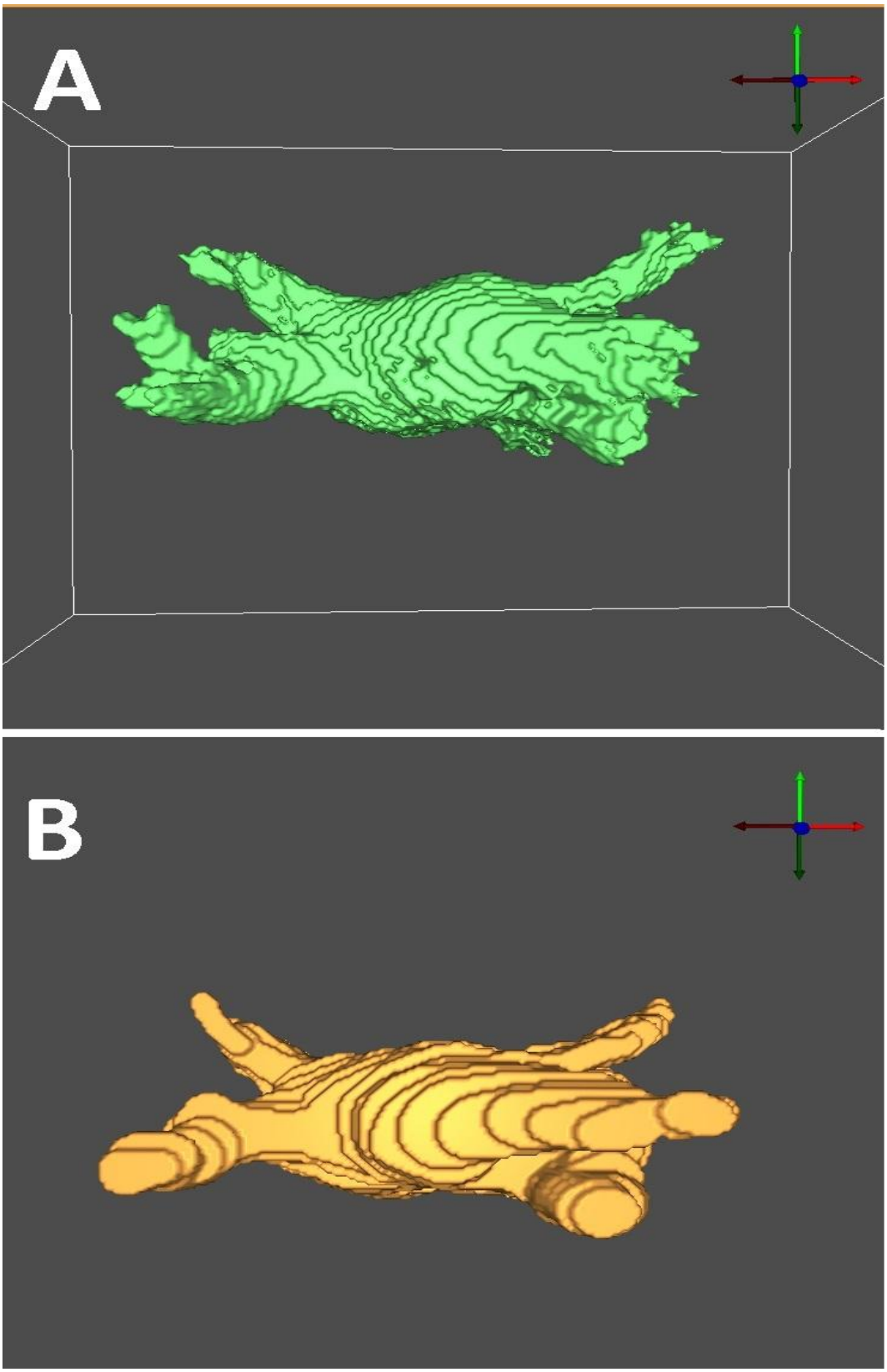

Figure 23. A) Result of Marker-Controlled Watershed Segmentation. B) Corresponding ground-truth image. (Dataset ID : 154)

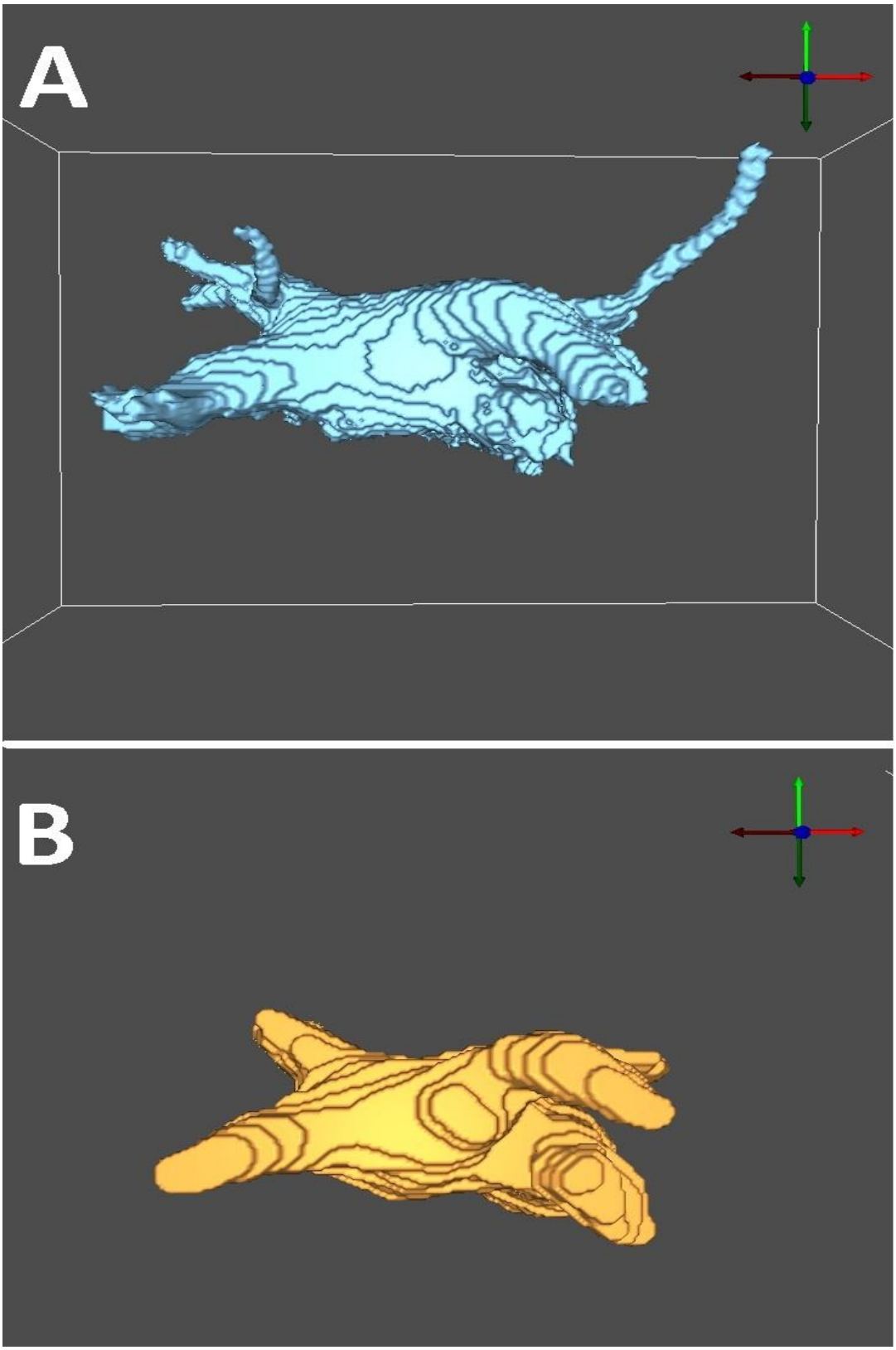

Figure 24. A) Result of Marker-Controlled Watershed Segmentation. B) Corresponding ground-truth image. (Dataset ID : 254)

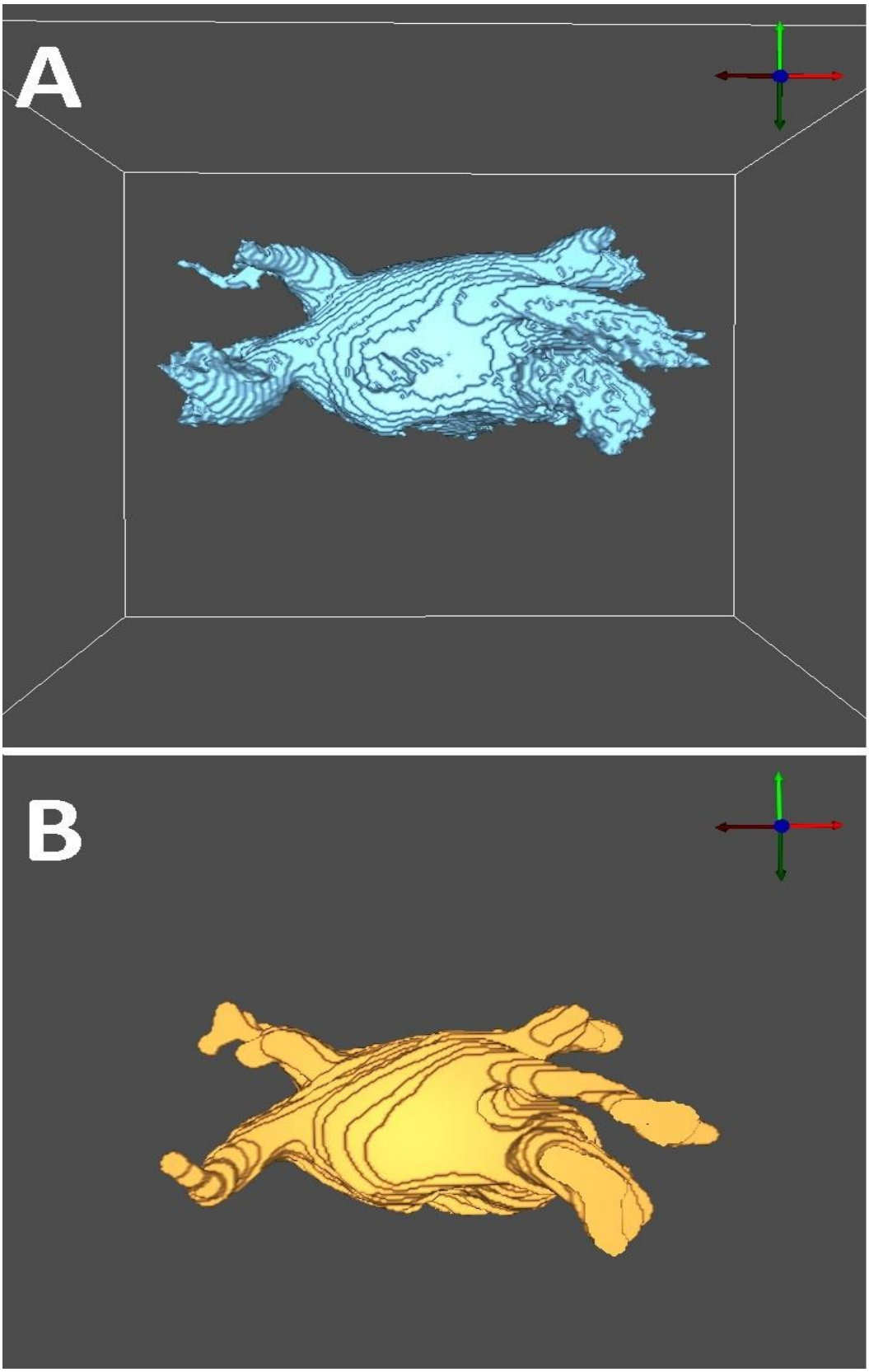

Figure 25. A) Result of Marker-Controlled Watershed Segmentation. B) Corresponding ground-truth image.(Dataset ID : 440)

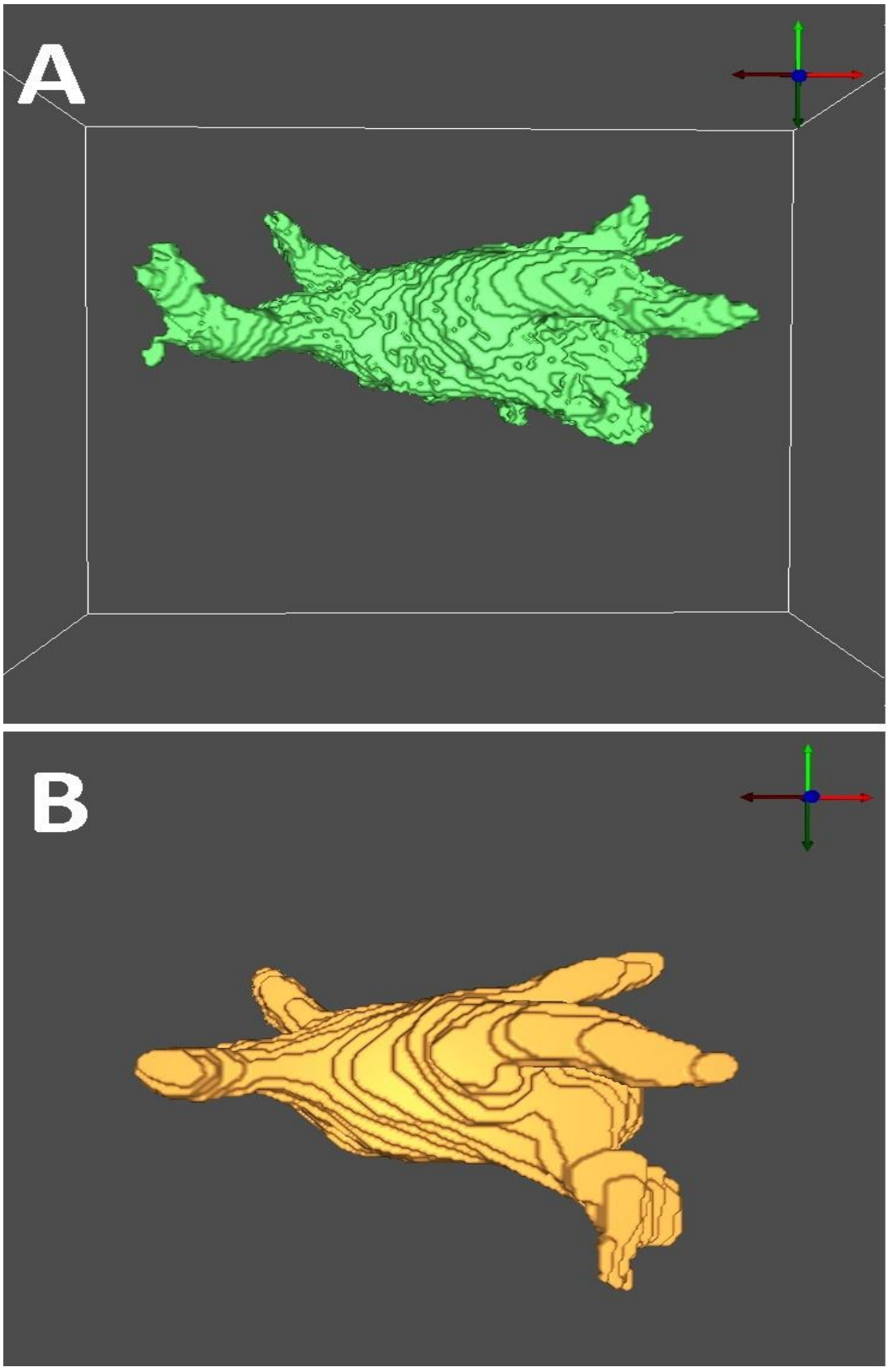

Figure 26. A) Result of Marker-Controlled Watershed Segmentation. B) Corresponding ground-truth image. (Dataset ID : 606)

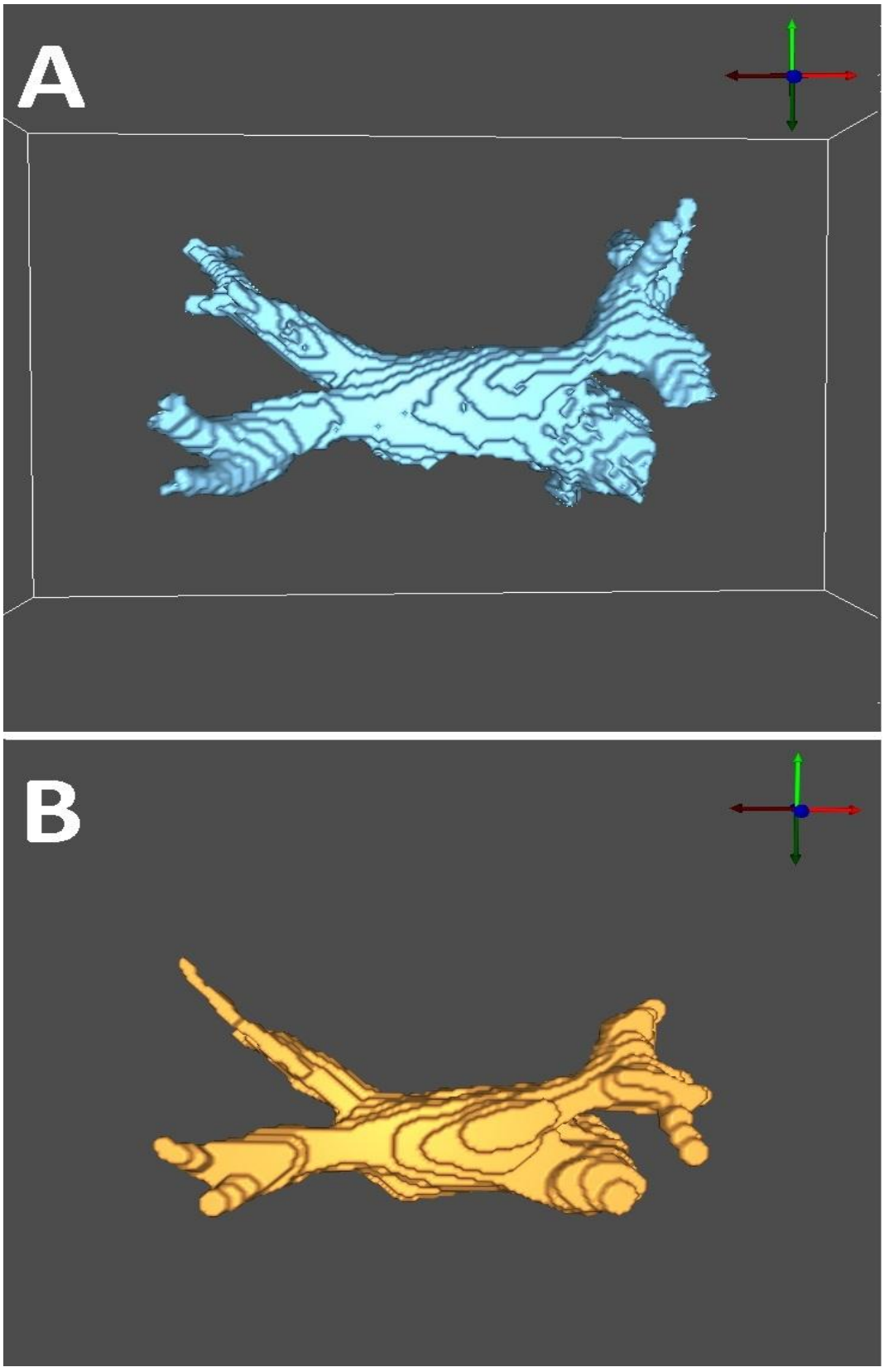

Figure 27. A) Result of Marker-Controlled Watershed Segmentation. B) Corresponding ground-truth image. (Dataset ID : 886)

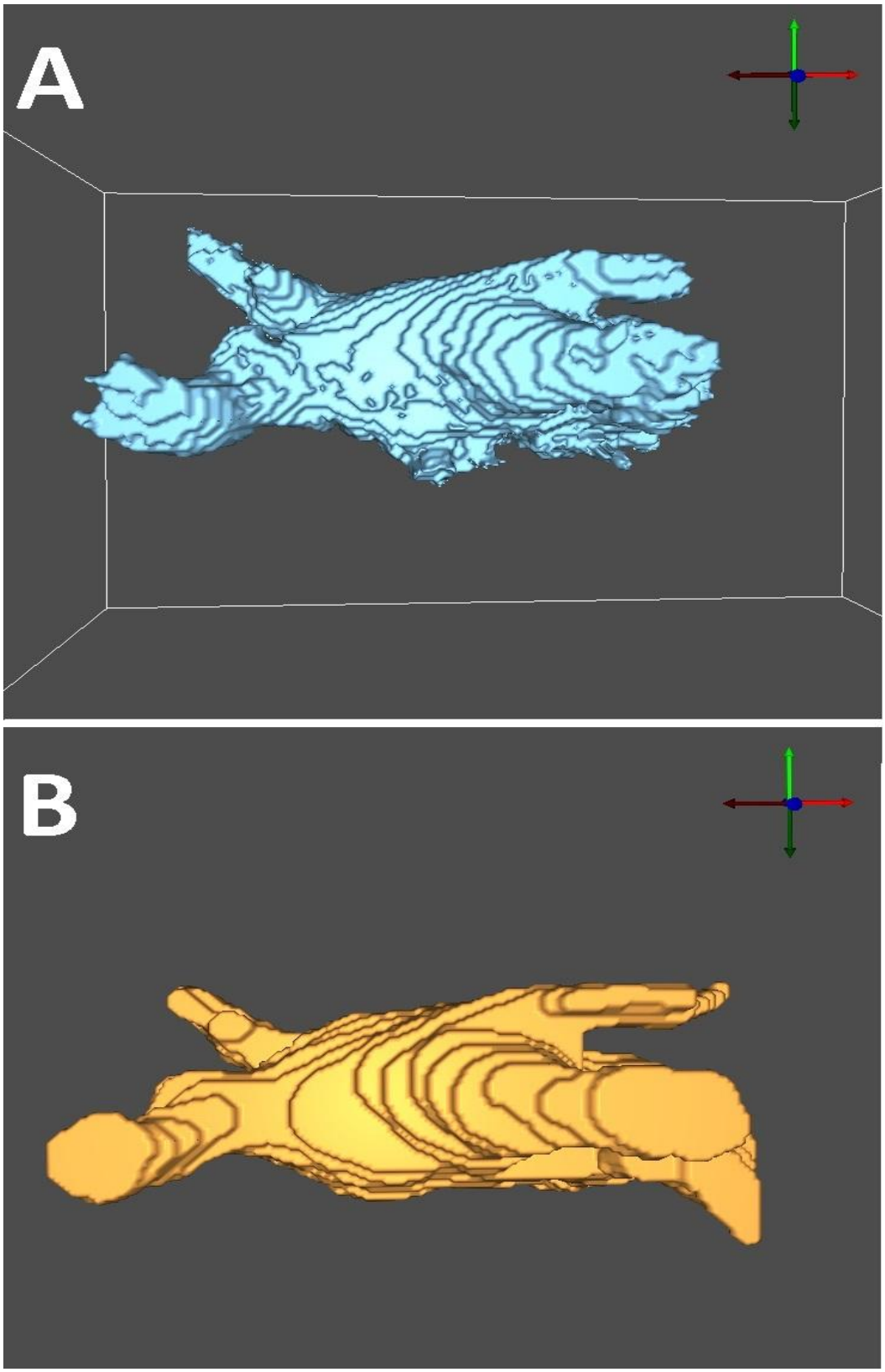

Figure 28. A) Result of Marker-Controlled Watershed Segmentation. B) Corresponding ground-truth image. (Dataset ID : 937)

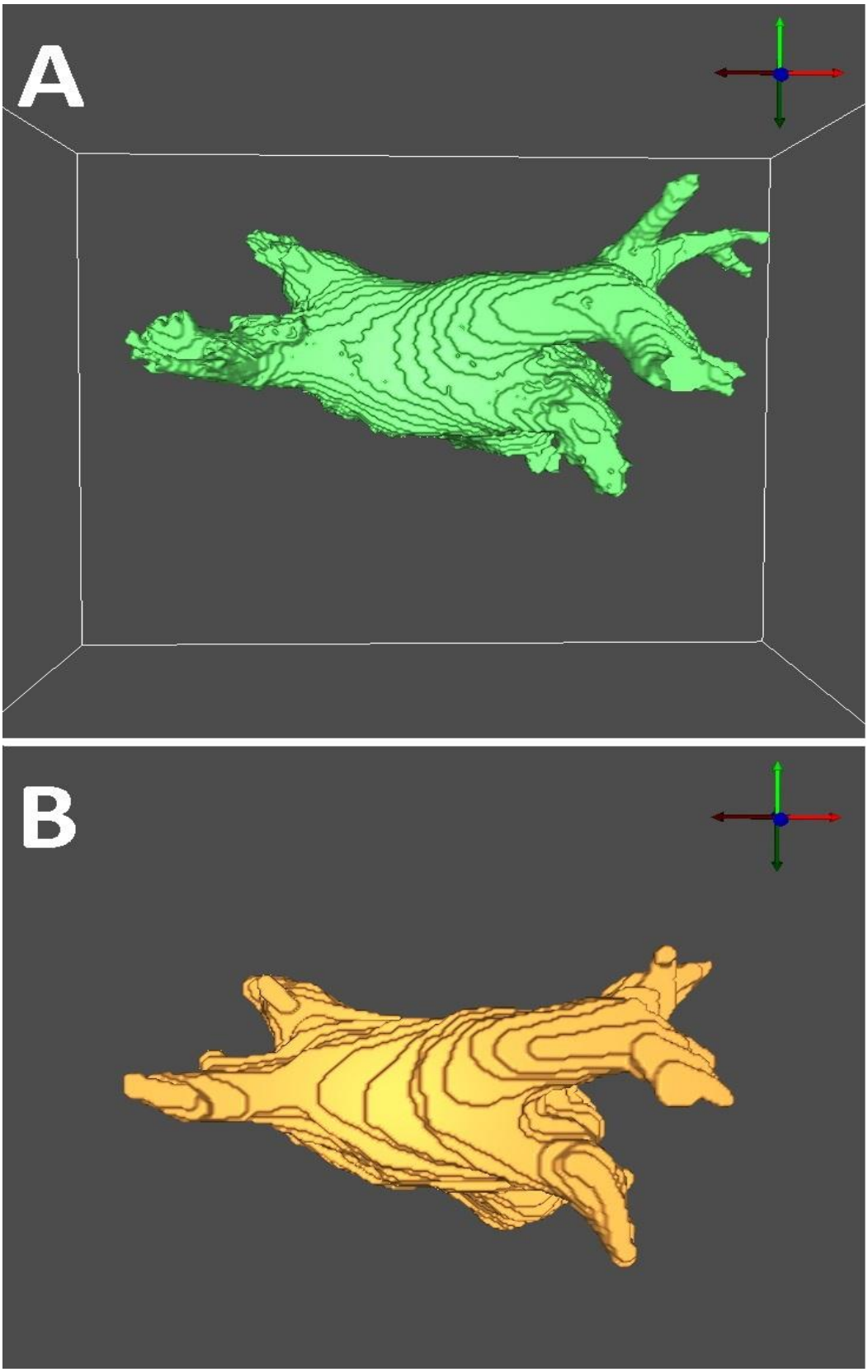

Figure 29. A) Result of Marker-Controlled Watershed Segmentation. B) Corresponding ground-truth image. (Dataset ID : 969)

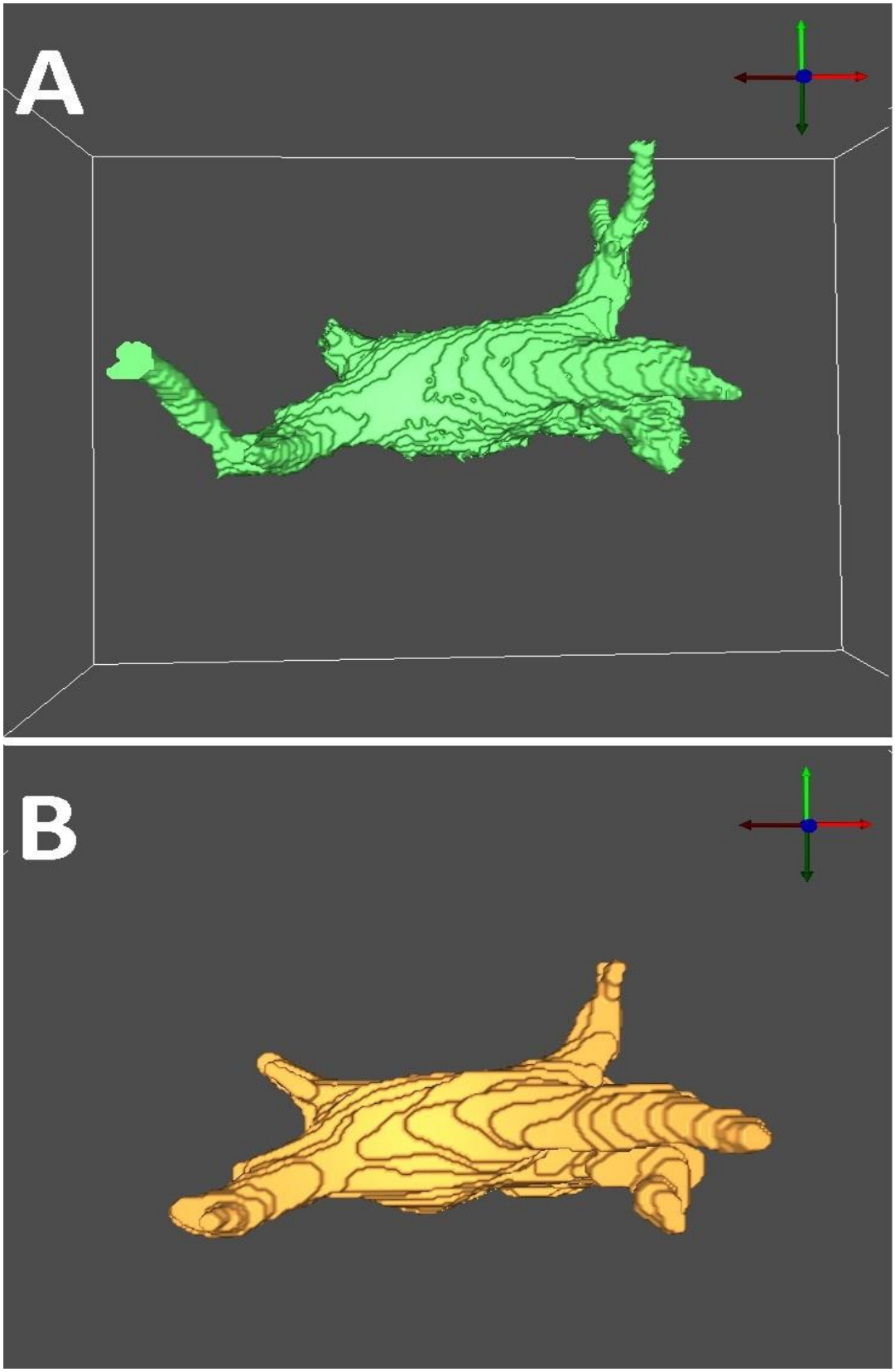

Figure 30. A) Result of Marker-Controlled Watershed Segmentation. B) Corresponding ground-truth image. (Dataset ID : 996)

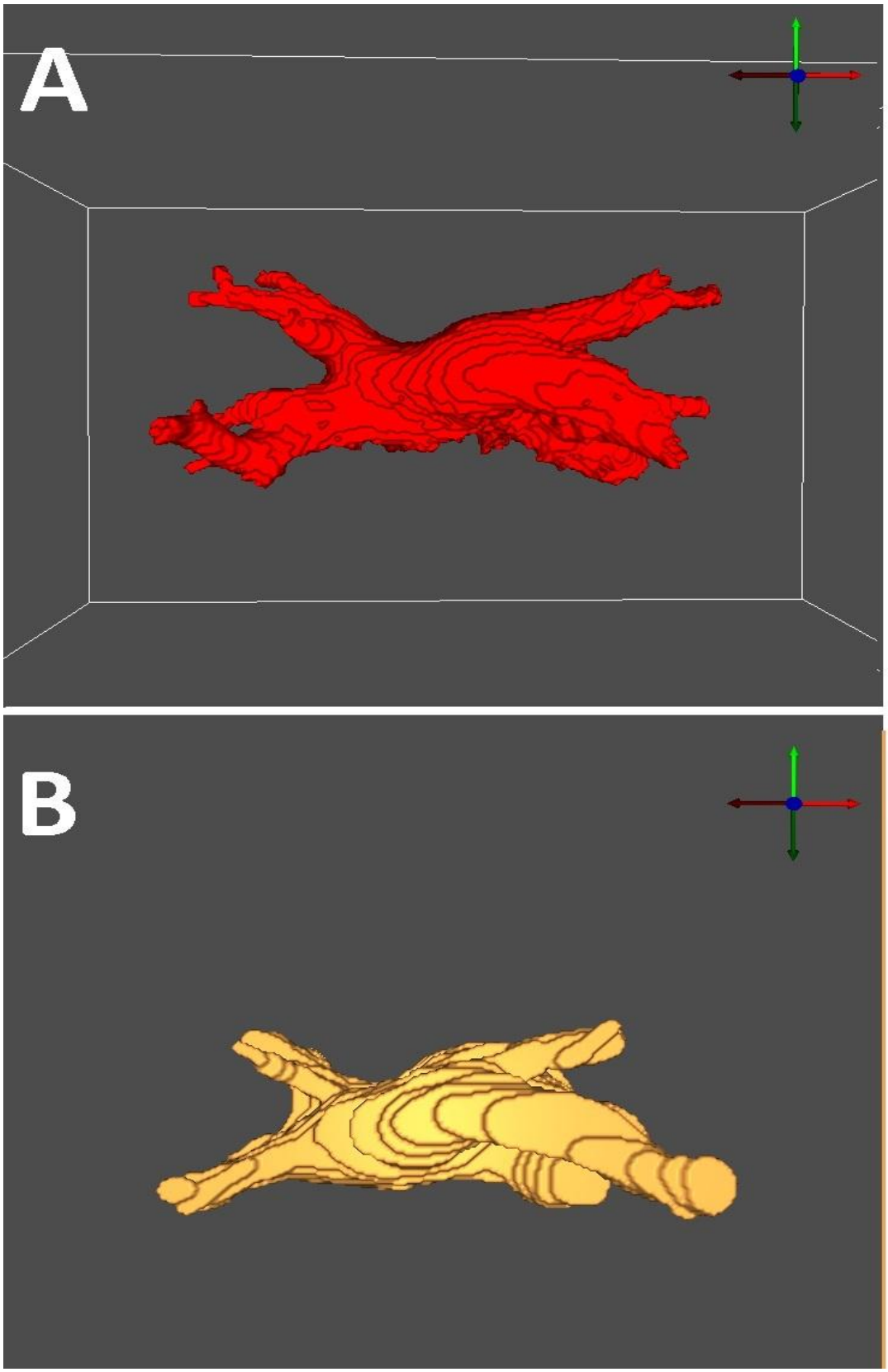

Figure 31. A) Result of Marker-Controlled Watershed Segmentation. B) Corresponding ground-truth image. (Dataset ID : 1063)

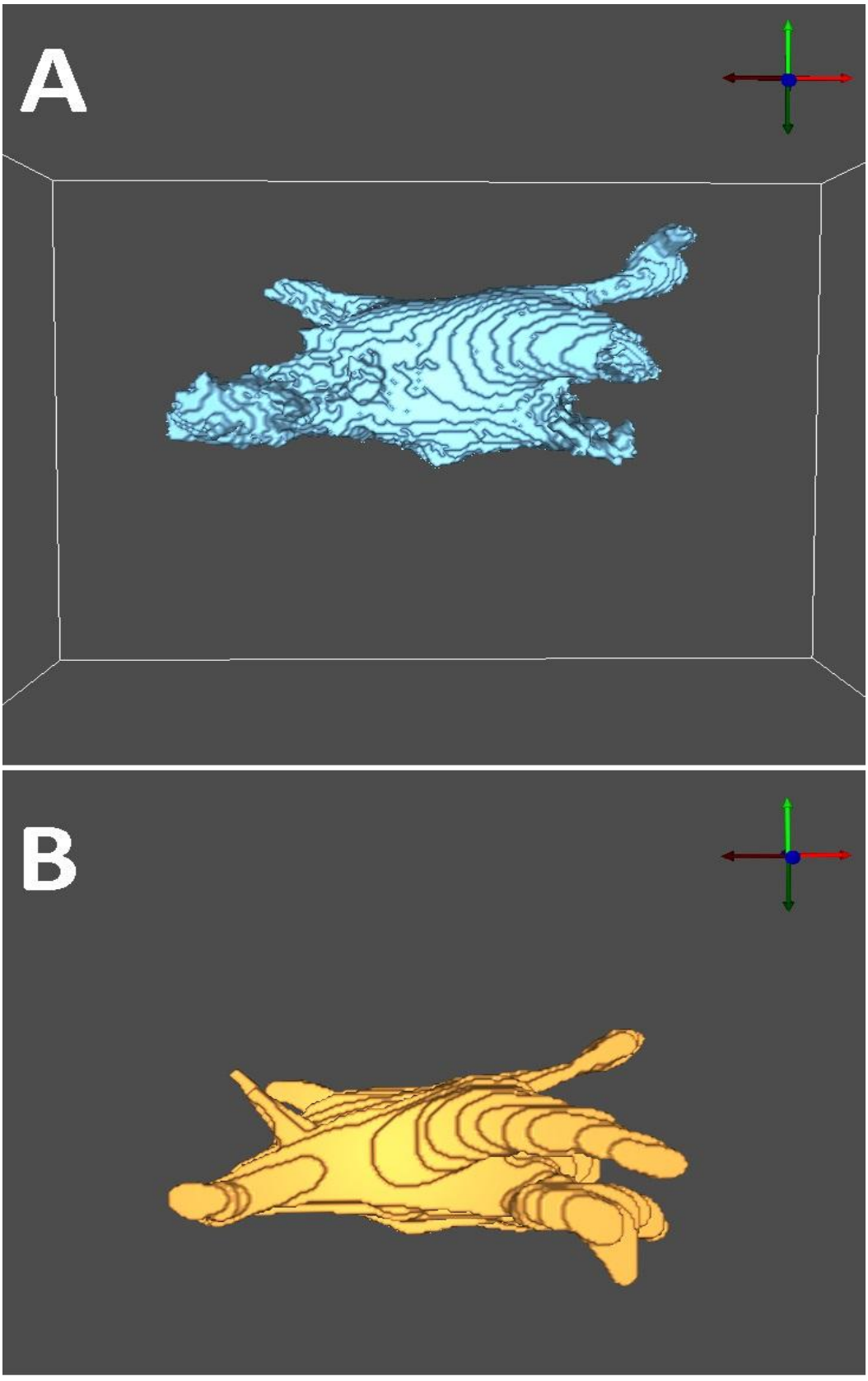

Figure 32. A) Result of Marker-Controlled Watershed Segmentation. B) Corresponding ground-truth image. (Dataset ID : 1092)

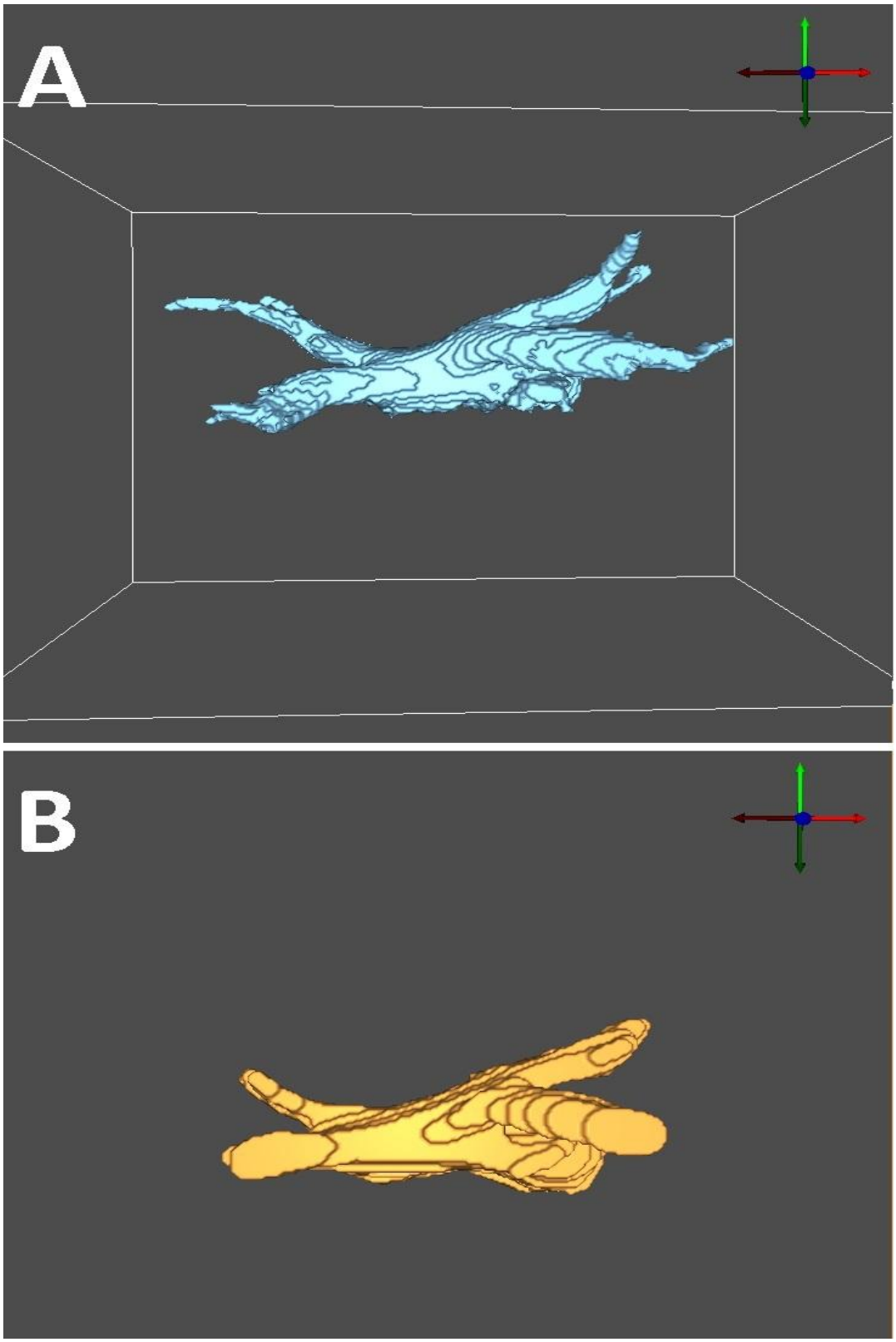

Figure 33. A) Result of Marker-Controlled Watershed Segmentation. B) Corresponding ground-truth image. (Dataset ID : 1133)

10. Appendix B

The distance between points of two datasets (each single Marker-Controlled Watershed Segmentation and its ground truth image) is presented in this chapter from two different angles based on a Hausdorff Distance algorithm. Theses image datasets depict the accuracy of the algorithm based on the distance between each point of Marker-Controlled Watershed output compared to the ground truth image. Nevertheless, this algorithm computes the distances according to point to cell instead of point to point, hence the results are more accurate. Here we considered the Marker-Controlled Watershed outputs as the reconstructions while the ground truth images are considered to be references, and the results have been calculated based on reconstruction versus reference. Also corresponded histogram is presented for all the datasets.

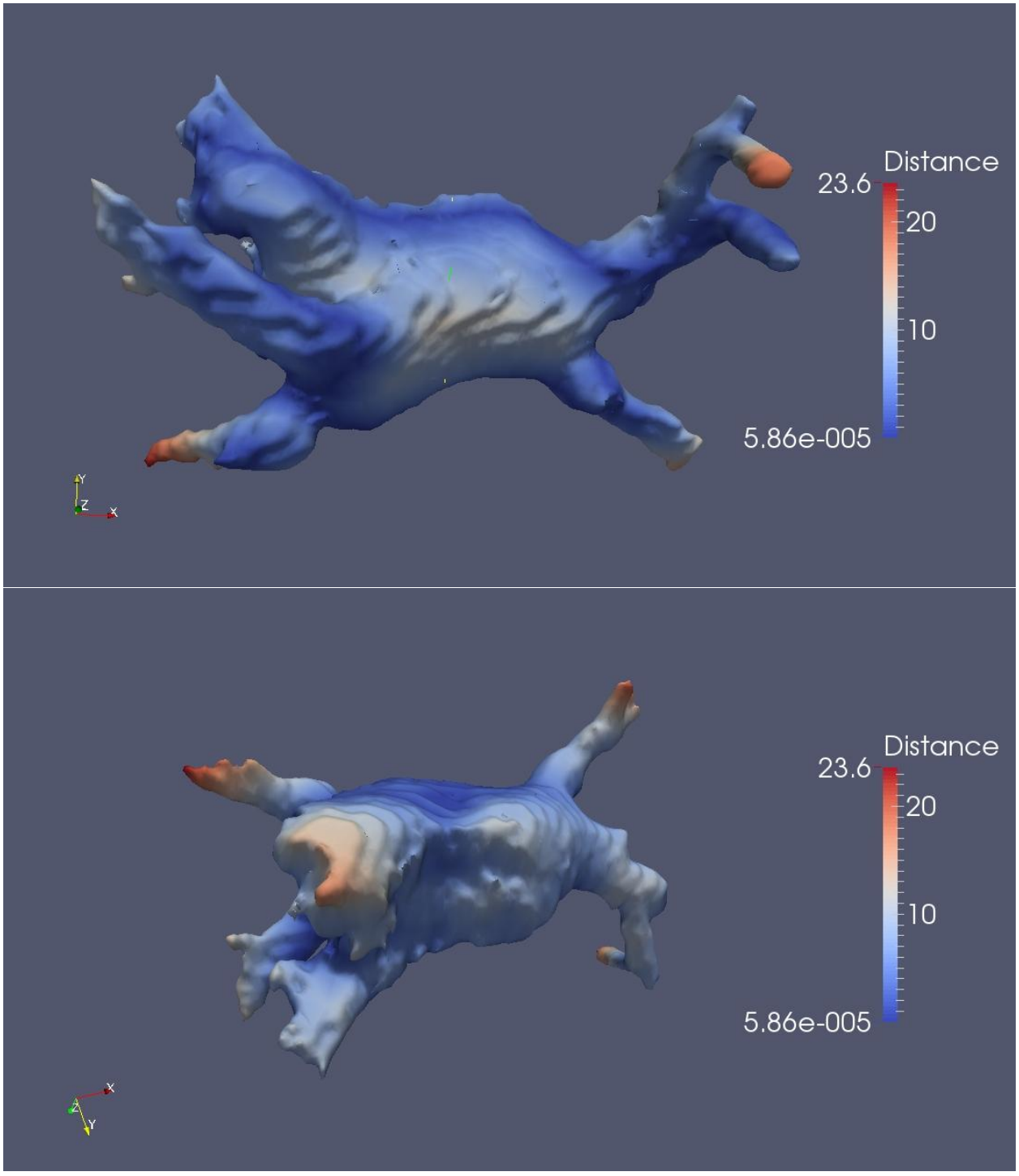

Figure 34. A 3D reconstruction of the Marker-Controlled Watershed Segmentation versus the ground-truth image as the reference, dark blue color show the maximum overlap between the points of two data sets, while dark red color shows the maximum distance between points of two data sets. (Dataset ID : 72)

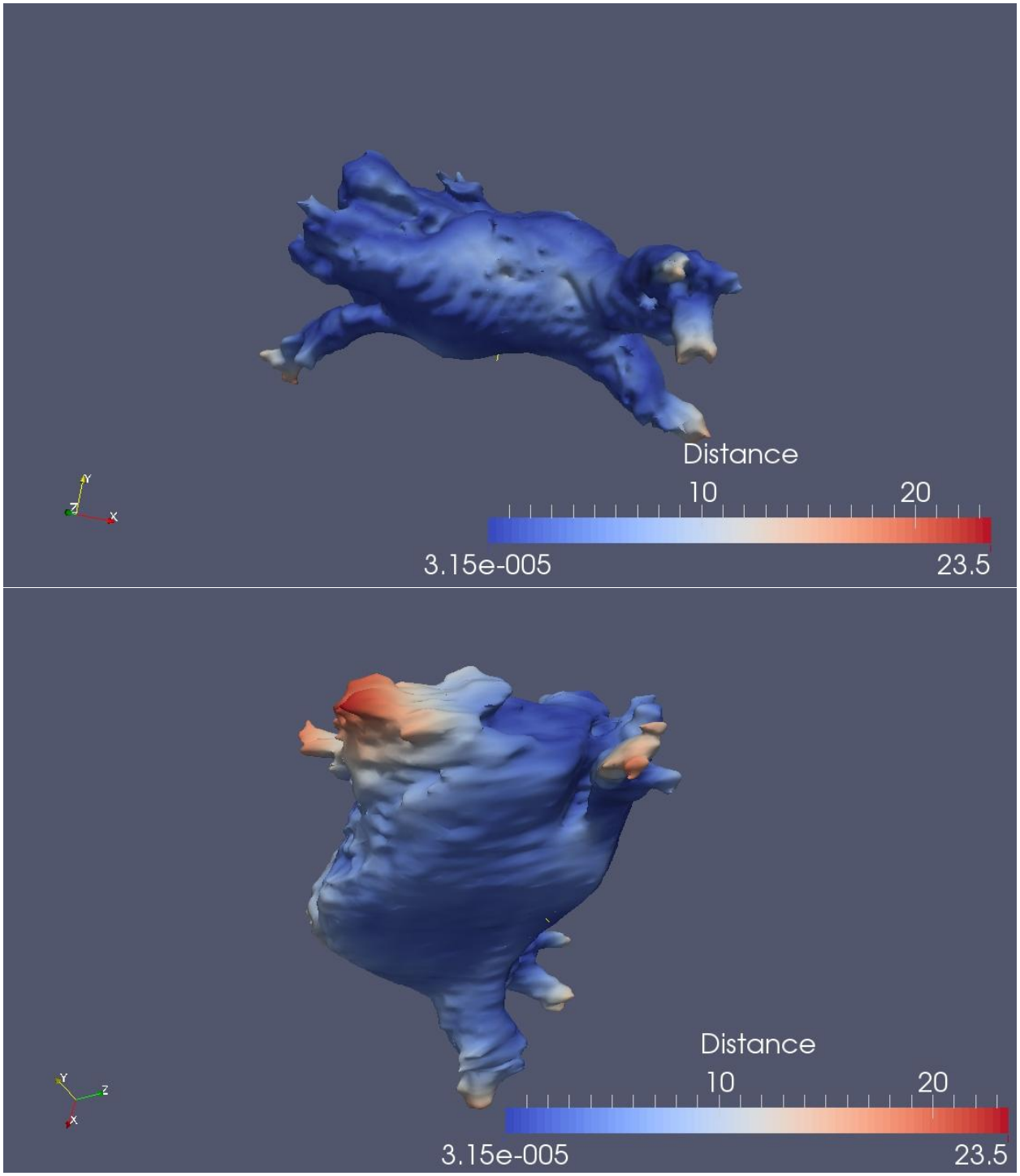

Figure 35. A 3D reconstruction of the Marker-Controlled Watershed Segmentation versus the ground-truth image as the reference, dark blue color show the maximum overlap between the points of two data sets, while dark red color shows the maximum distance between points of two data sets. (Dataset ID : 154)

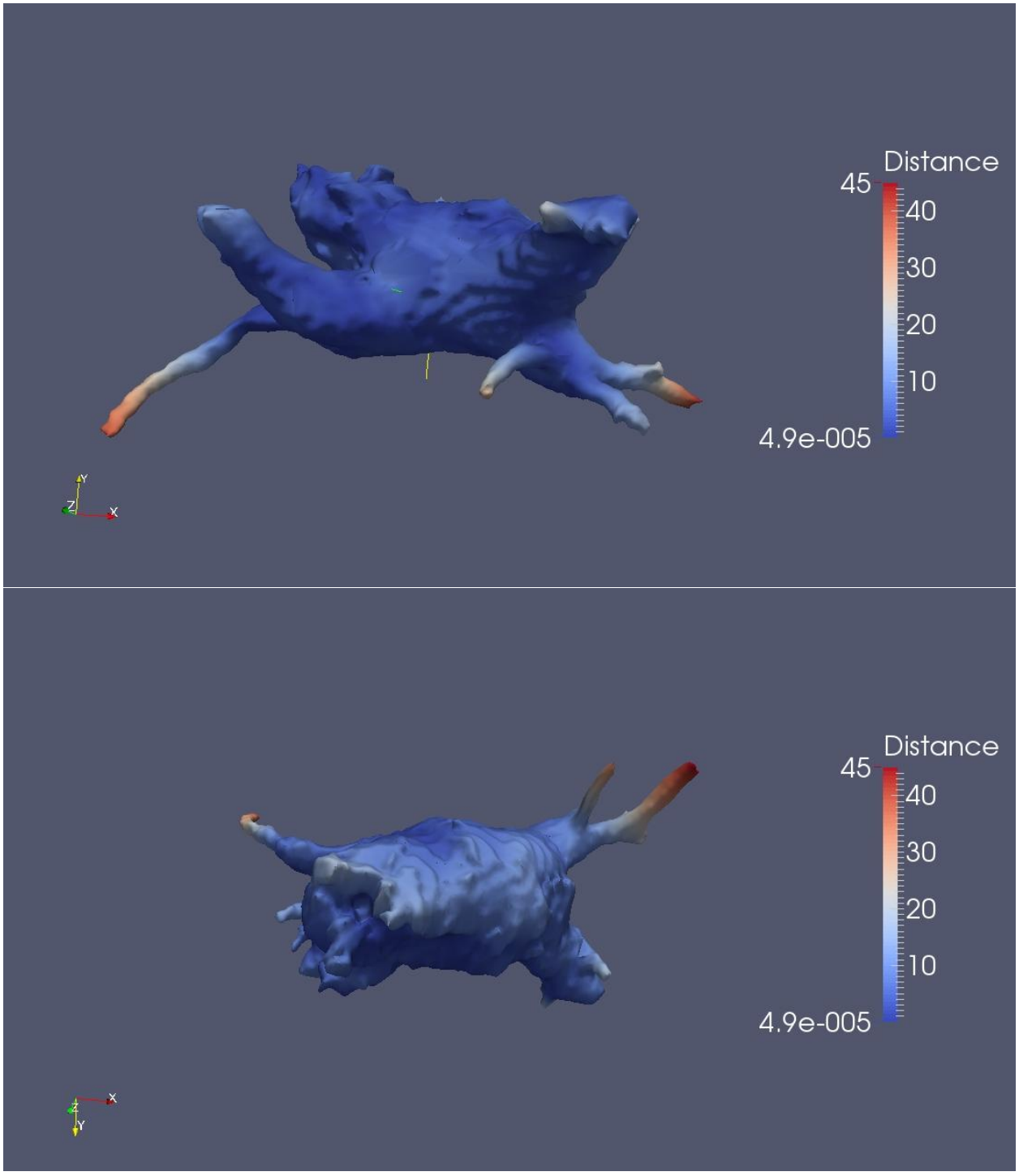

Figure 36. A 3D reconstruction of the Marker-Controlled Watershed Segmentation versus the ground-truth image as the reference, dark blue color show the maximum overlap between the points of two data sets, while dark red color shows the maximum distance between points of two data sets. (Dataset ID : 254)

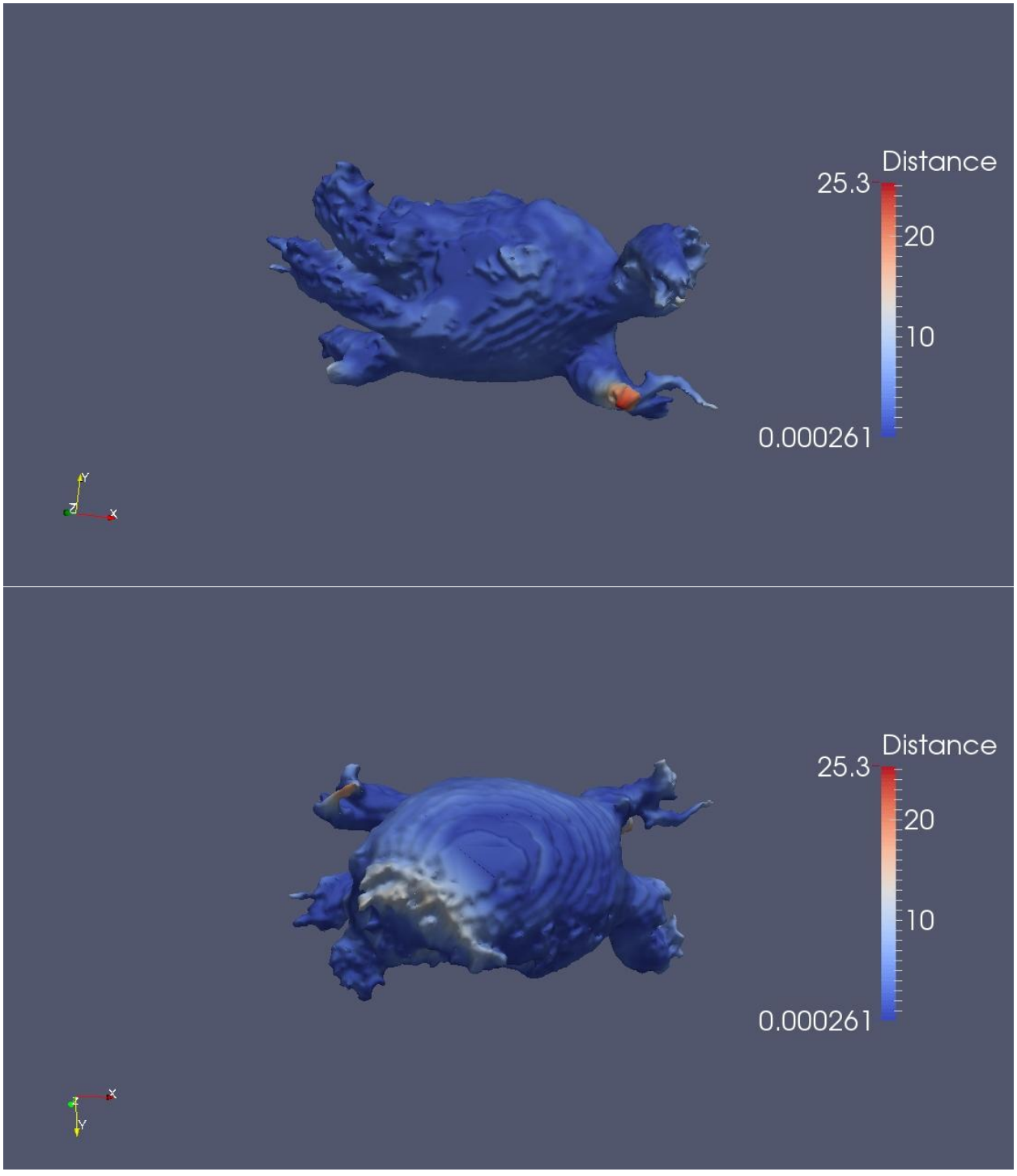

Figure 37. A 3D reconstruction of the Marker-Controlled Watershed Segmentation versus the ground-truth image as the reference, dark blue color show the maximum overlap between the points of two data sets, while dark red color shows the maximum distance between points of two data sets. (Dataset ID : 440)

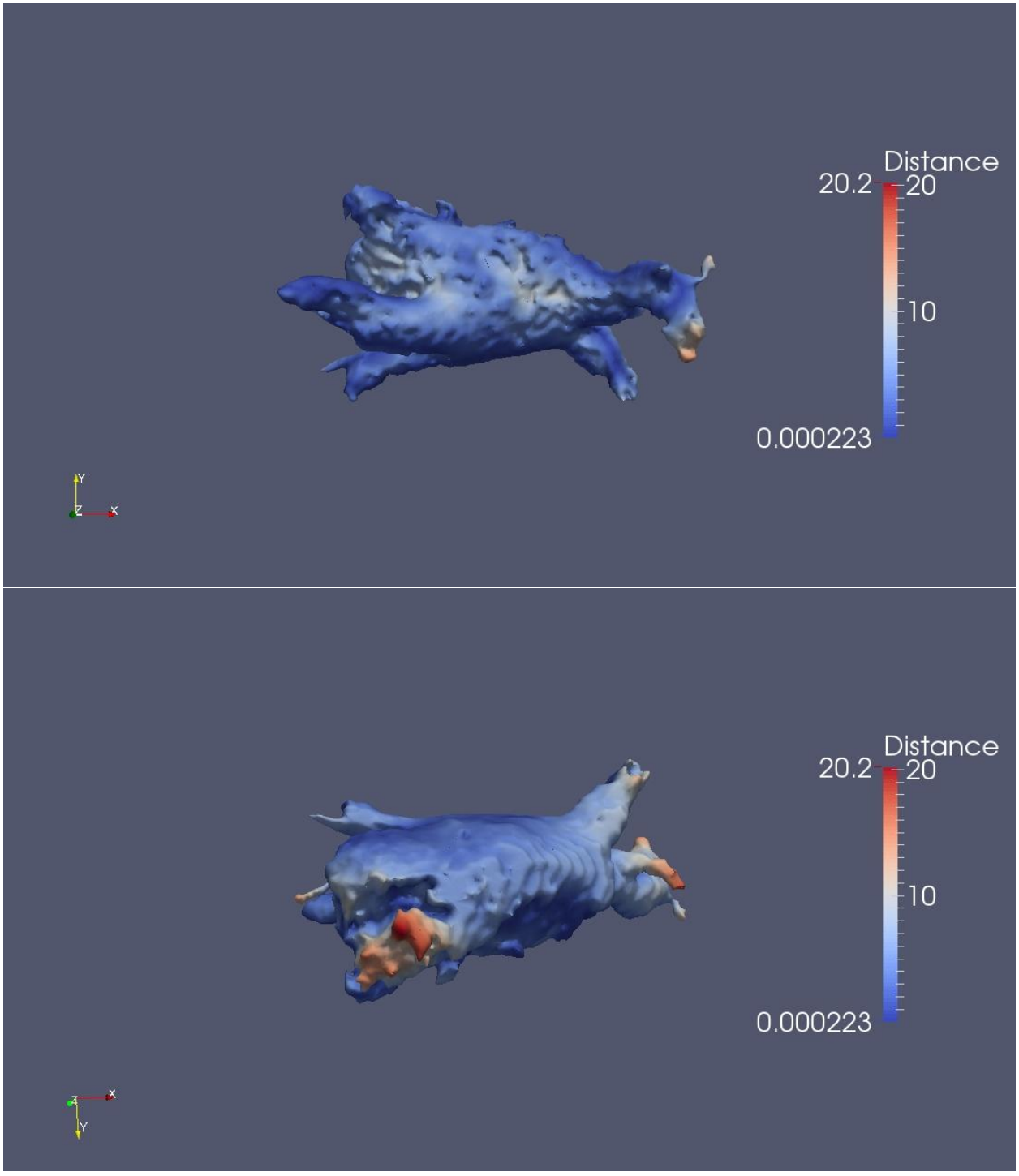

Figure 38. A 3D reconstruction of the Marker-Controlled Watershed Segmentation versus the ground-truth image as the reference, dark blue color show the maximum overlap between the points of two data sets, while dark red color shows the maximum distance between points of two data sets. (Dataset ID : 606)

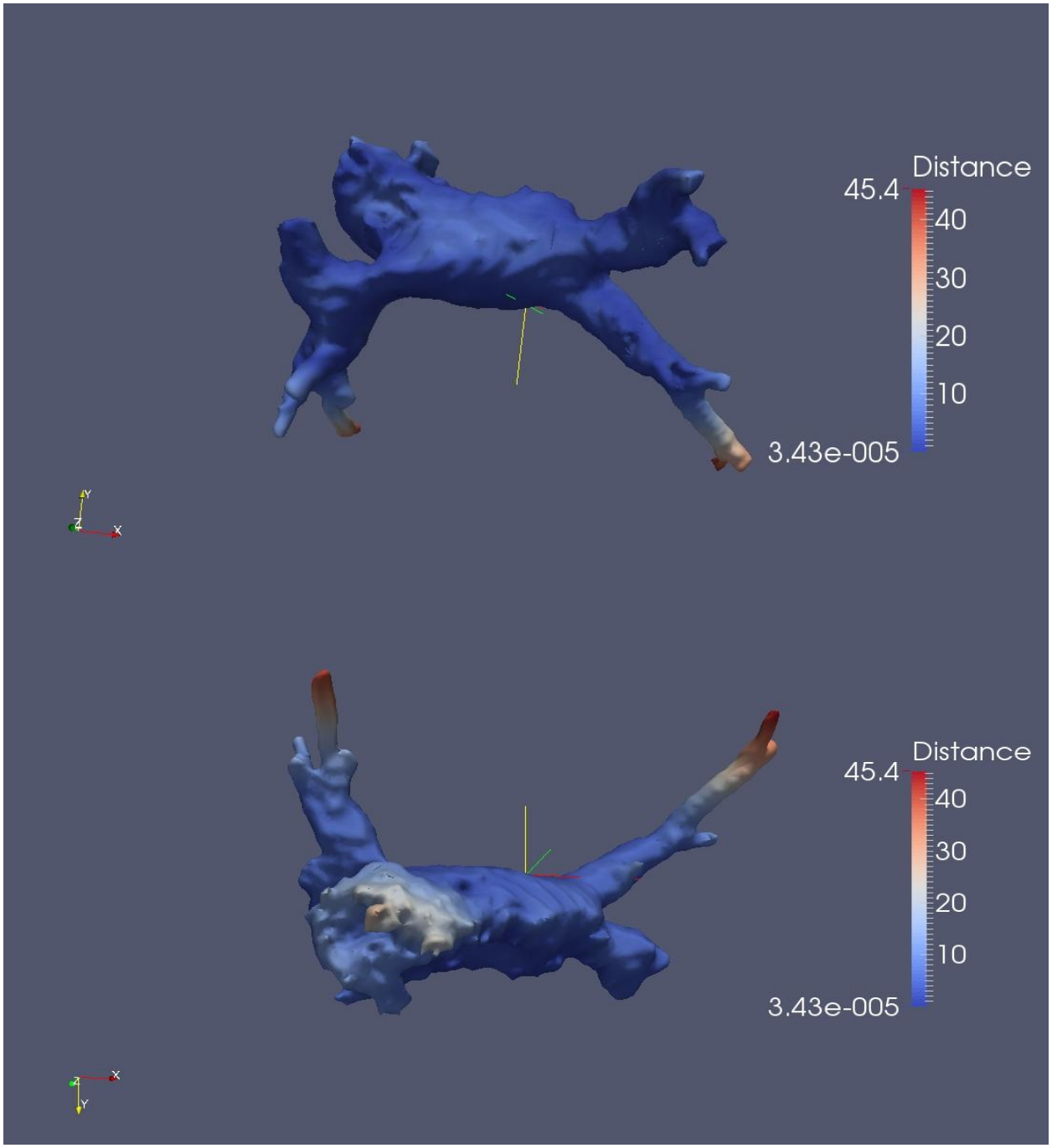

Figure 39. A 3D reconstruction of the Marker-Controlled Watershed Segmentation versus the ground-truth image as the reference, dark blue color show the maximum overlap between the points of two data sets, while dark red color shows the maximum distance between points of two data sets. (Dataset ID : 886)

.

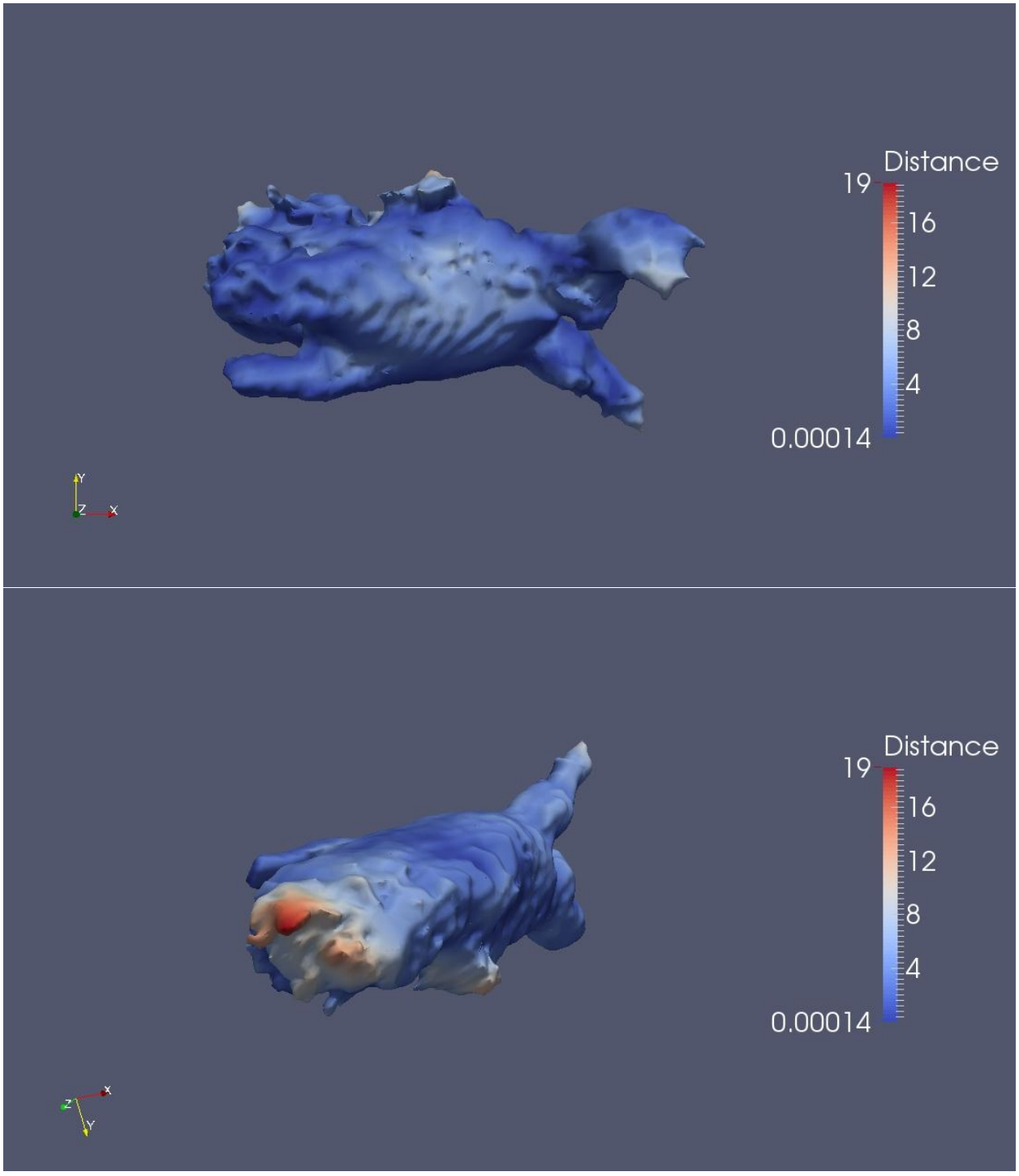

Figure 40. A 3D reconstruction of the Marker-Controlled Watershed Segmentation versus the ground-truth image as the reference, dark blue color show the maximum overlap between the points of two data sets, while dark red color shows the maximum distance between points of two data sets. (Dataset ID : 937)

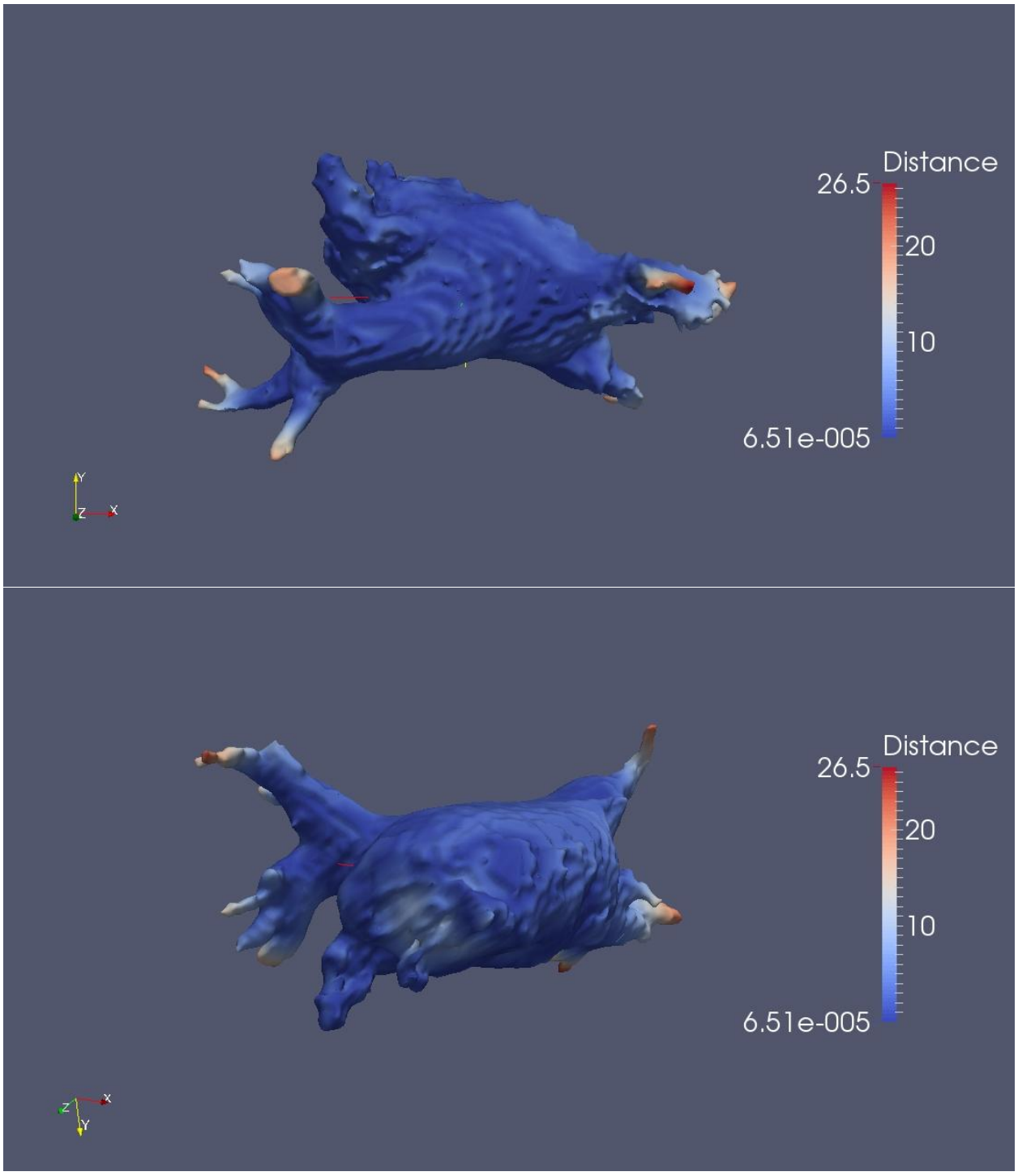

Figure 41. A 3D reconstruction of the Marker-Controlled Watershed Segmentation versus the ground-truth image as the reference, dark blue color show the maximum overlap between the points of two data sets, while dark red color shows the maximum distance between points of two data sets. (Dataset ID : 969)

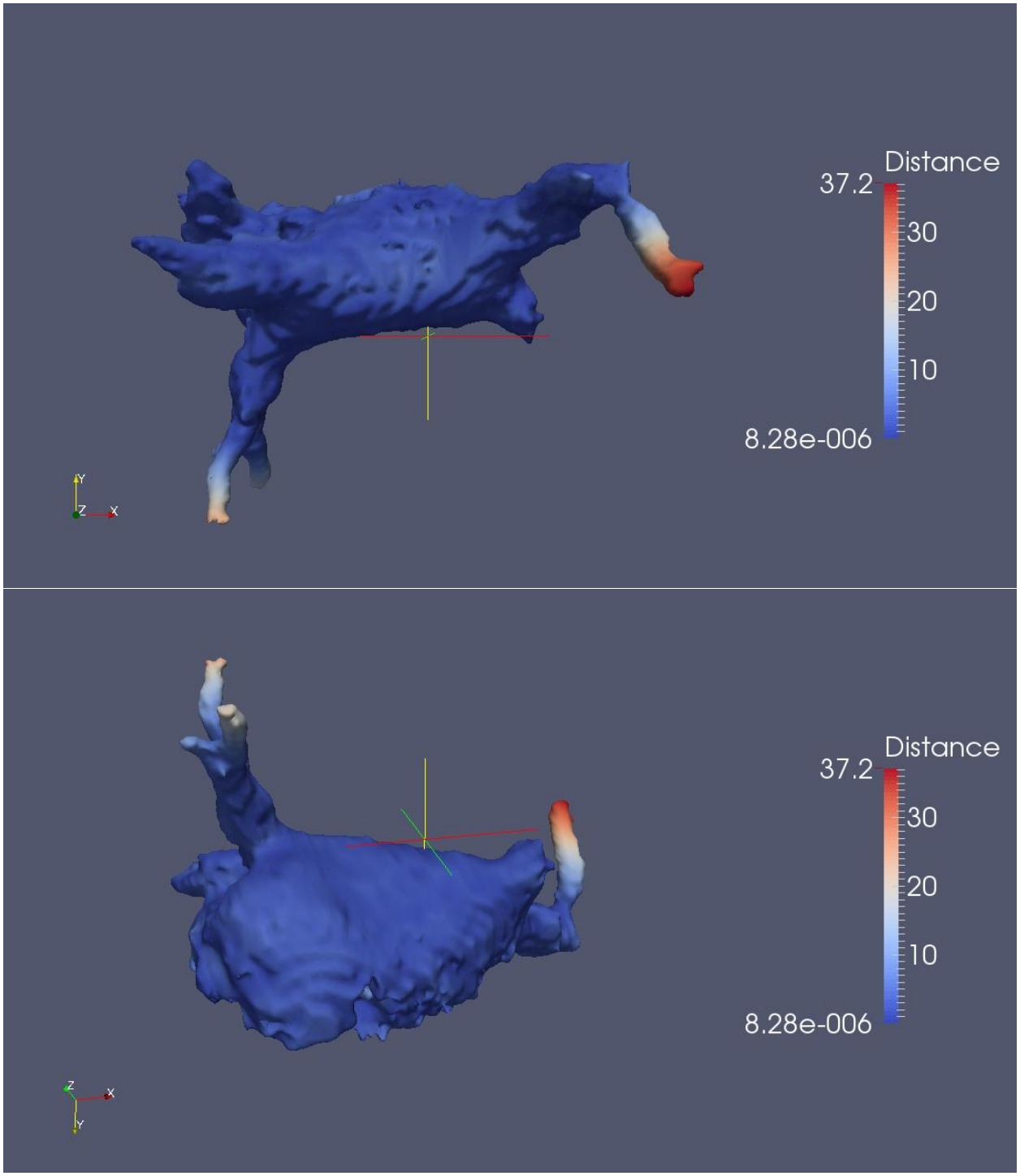

Figure 42. A 3D reconstruction of the Marker-Controlled Watershed Segmentation versus the ground-truth image as the reference, dark blue color show the maximum overlap between the points of two data sets, while dark red color shows the maximum distance between points of two data sets. (Dataset ID : 996)

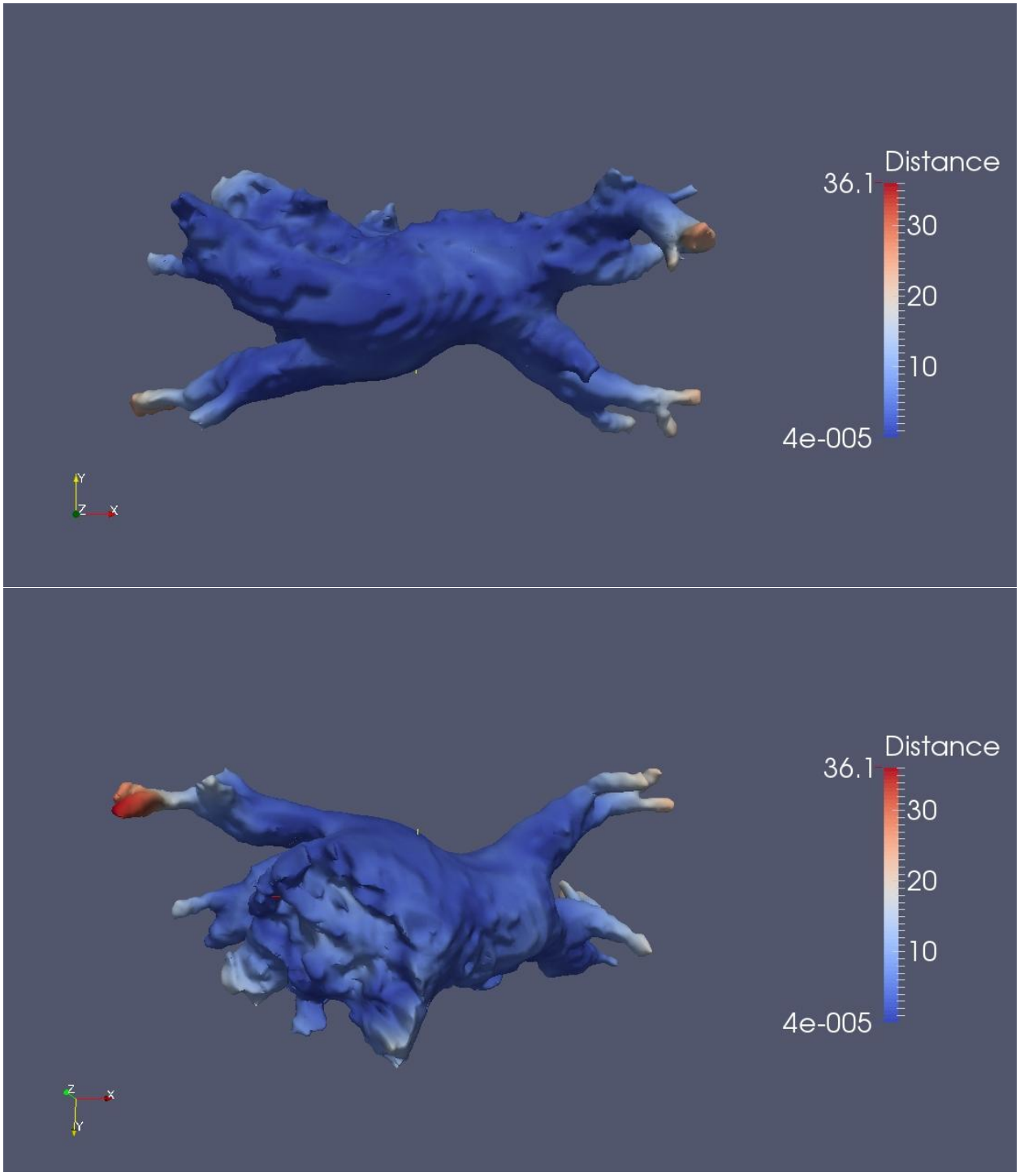

Figure 43. A 3D reconstruction of the Marker-Controlled Watershed Segmentation versus the ground-truth image as the reference, dark blue color show the maximum overlap between the points of two data sets, while dark red color shows the maximum distance between points of two data sets. (Dataset ID : 1063)

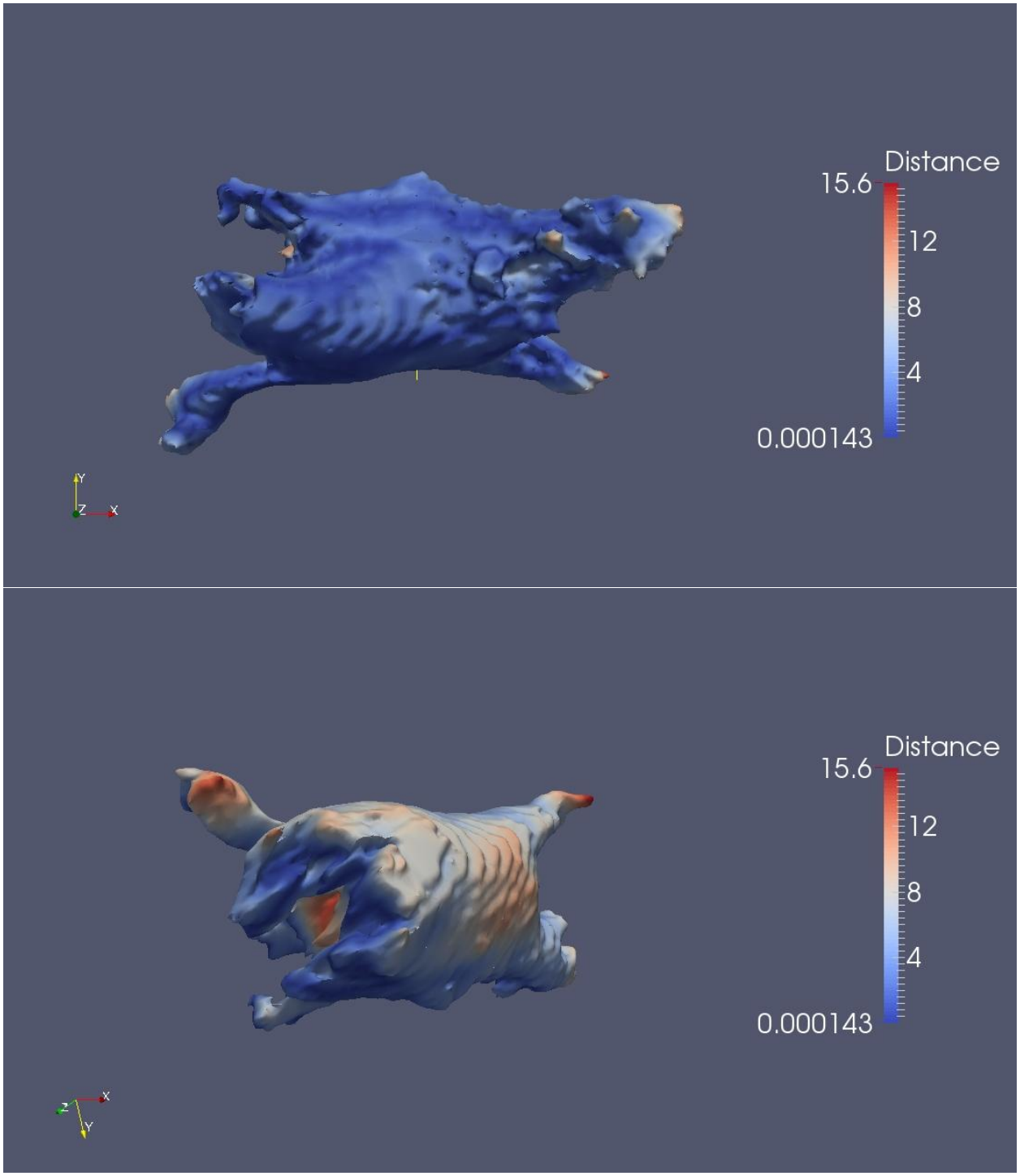

Figure 44. A 3D reconstruction of the Marker-Controlled Watershed Segmentation versus the ground-truth image as the reference, dark blue color show the maximum overlap between the points of two data sets, while dark red color shows the maximum distance between points of two data sets. (Dataset ID : 1092)

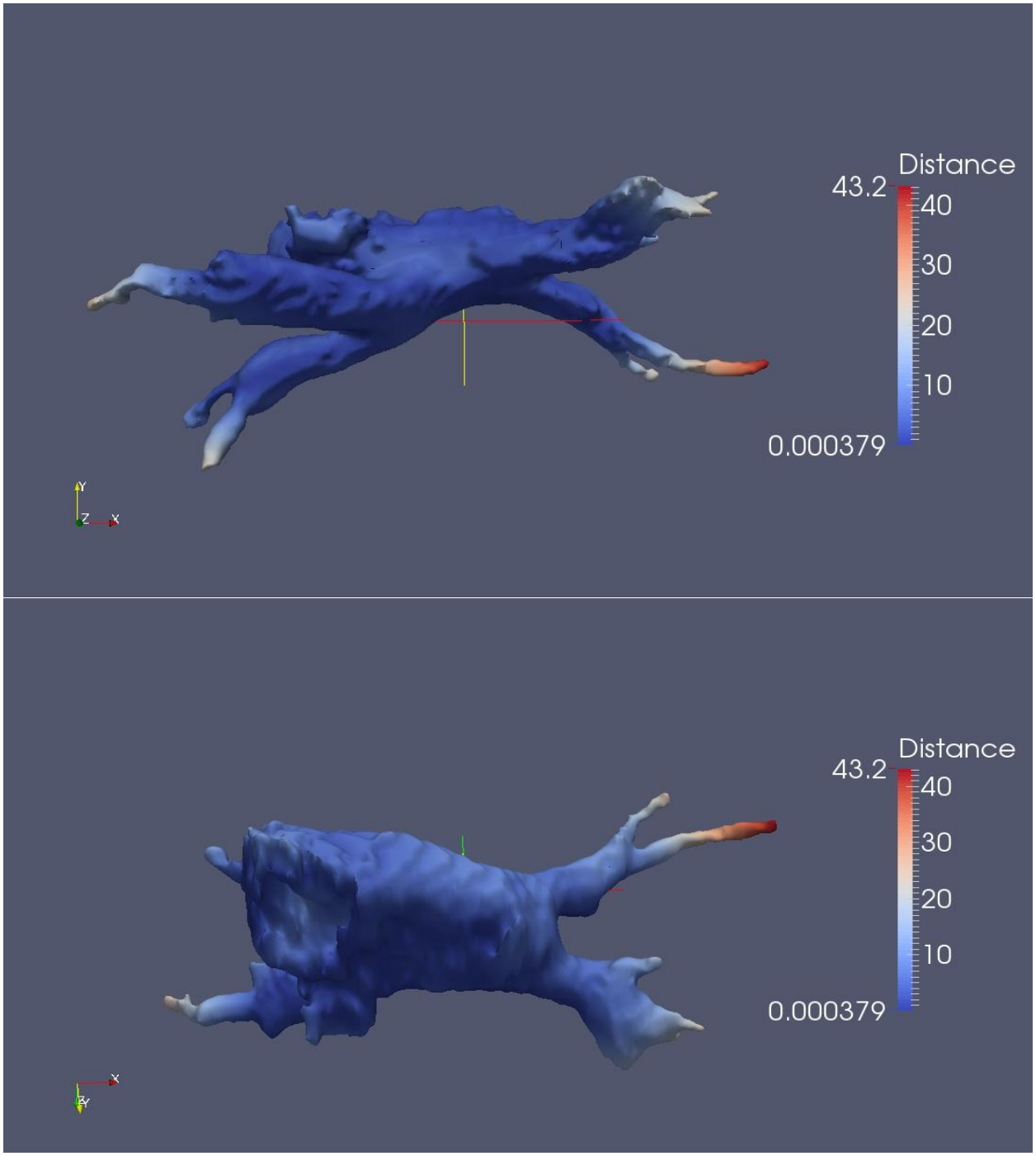

Figure 45. A 3D reconstruction of the Marker-Controlled Watershed Segmentation versus the ground-truth image as the reference, dark blue color show the maximum overlap between the points of two data sets, while dark red color shows the maximum distance between points of two data sets. (Dataset ID : 1133)

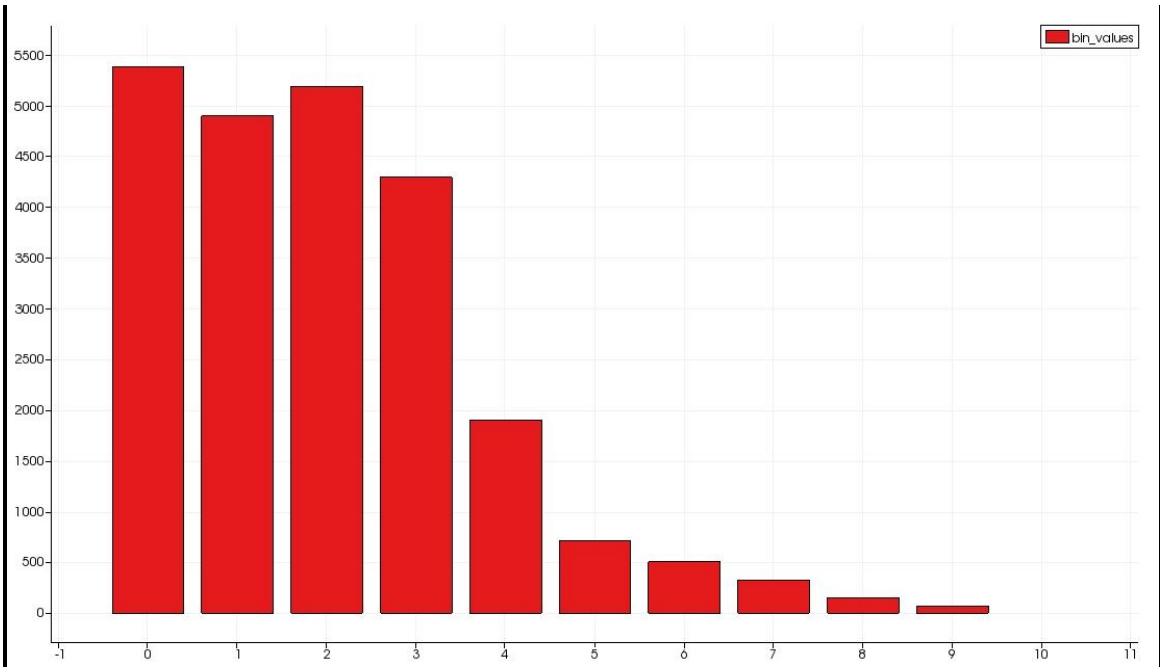

Figure 46 . Histogram of the Hausdorff Distance. It describes amounts of the points in two datasets have the distance 0 (points of two data sets are completely overlapped) until 9 (minimum overlap between points of two datasets). (Y-axis shows amount of the points while X-axis shows the distance in mm). (Dataset ID : 72)

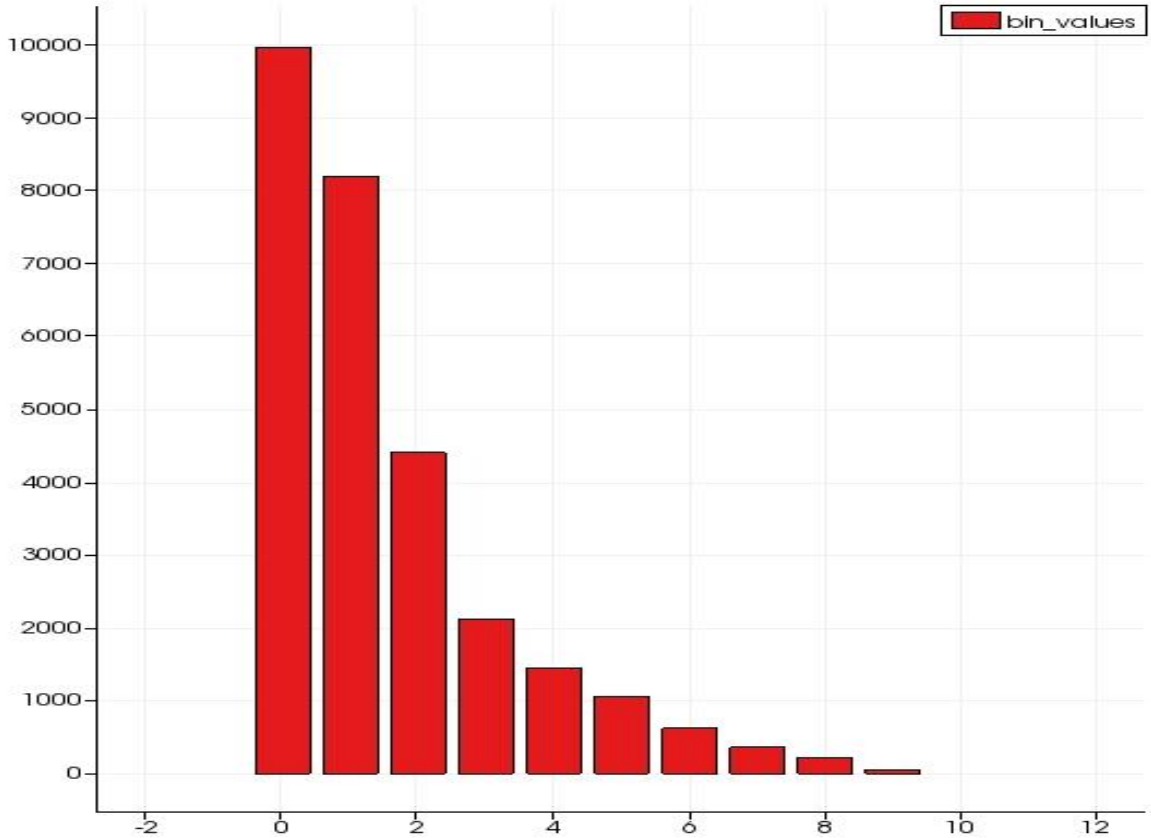

Figure 47 . Histogram of the Hausdorff Distance. It describes amounts of the points in two datasets have the distance 0 (points of two data sets are completely overlapped) until 9 (minimum overlap between points of two datasets). (Y-axis shows amount of the points while X-axis shows the distance in mm). (Dataset ID : 154)

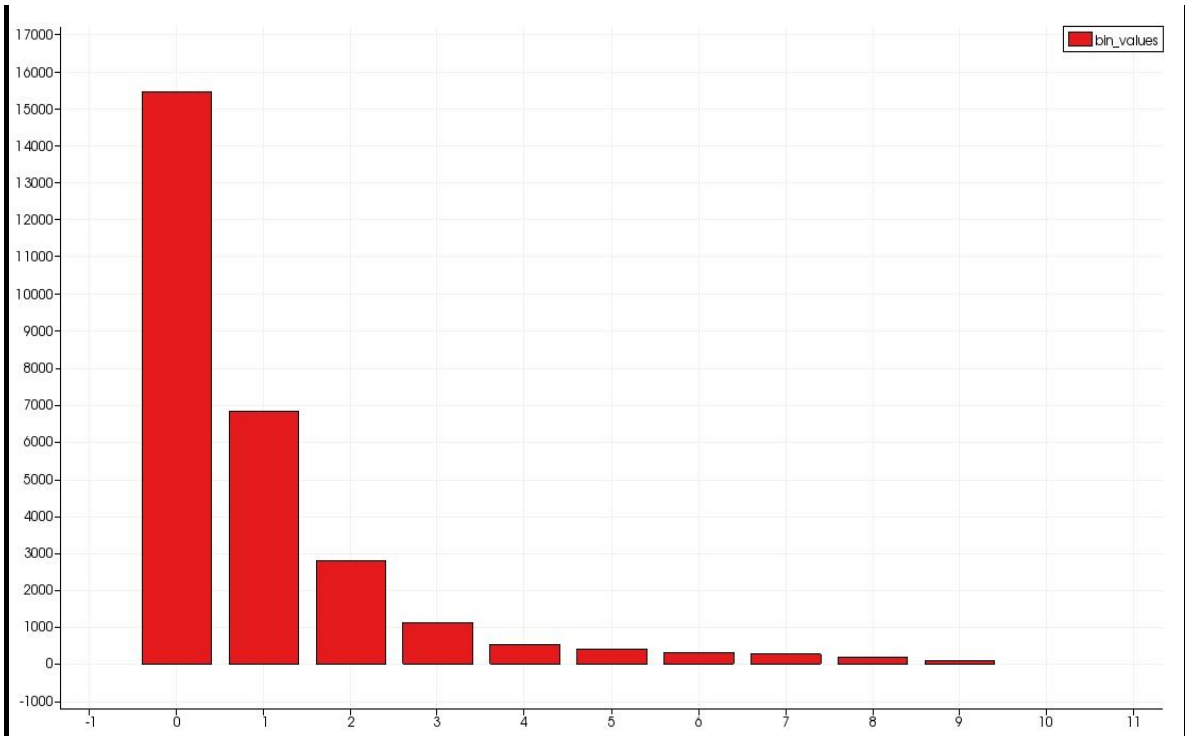

Figure 48 . Histogram of the Hausdorff Distance. It describes amounts of the points in two datasets have the distance 0 (points of two data sets are completely overlapped) until 9 (minimum overlap between points of two datasets). (Y-axis shows amount of the points while X-axis shows the distance in mm). (Dataset ID : 254)

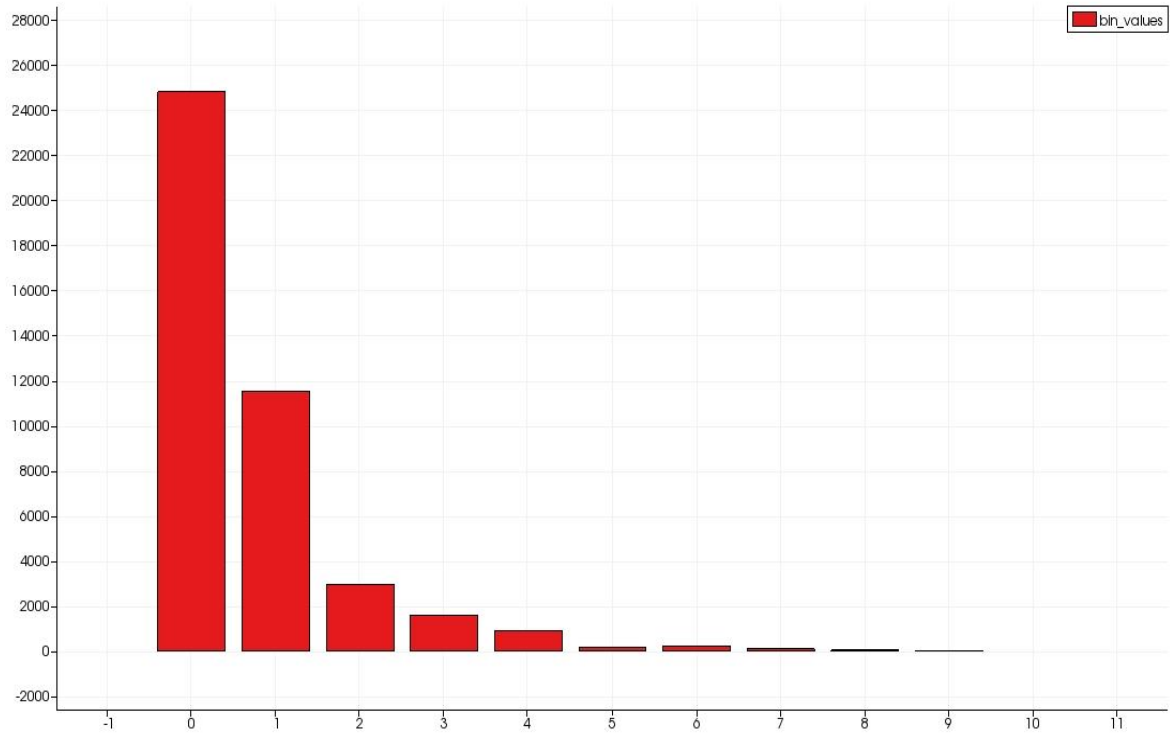

Figure 49 . Histogram of the Hausdorff Distance. It describes amounts of the points in two datasets have the distance 0 (points of two data sets are completely overlapped) until 9 (minimum overlap between points of two datasets). (Y-axis shows amount of the points while X-axis shows the distance in mm). (Dataset ID : 440)

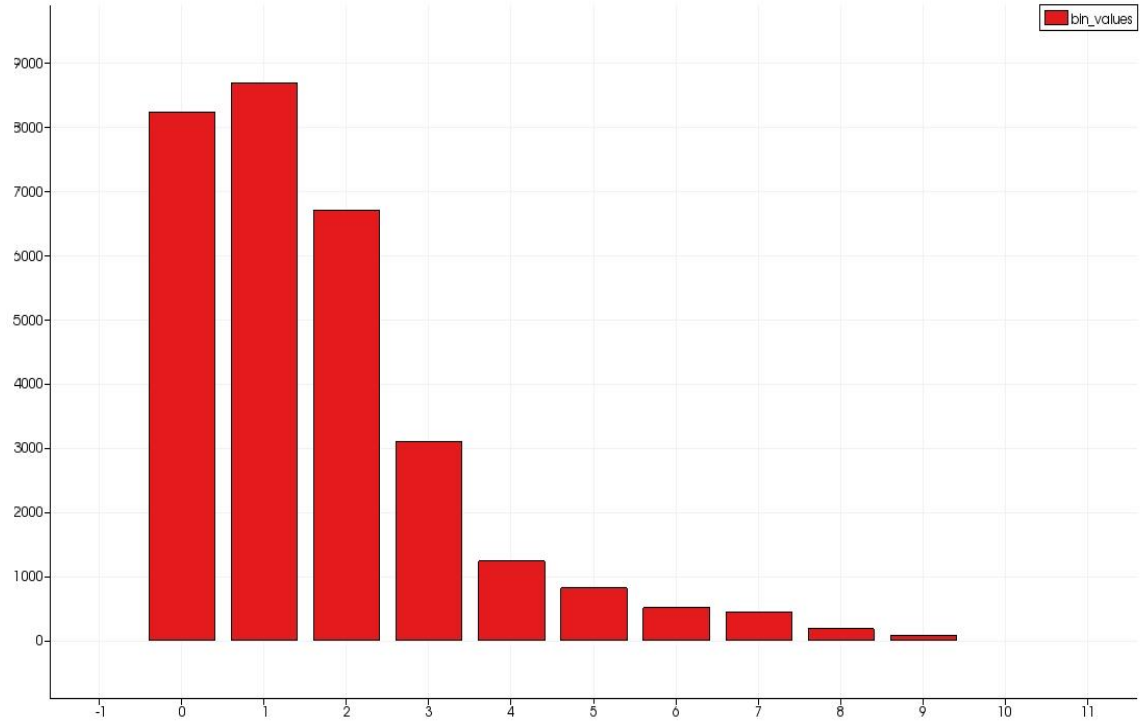

Figure 50 . Histogram of the Hausdorff Distance. It describes amounts of the points in two datasets have the distance 0 (points of two data sets are completely overlapped) until 9 (minimum overlap between points of two datasets). (Y-axis shows amount of the points while X-axis shows the distance in mm). (Dataset ID : 606)

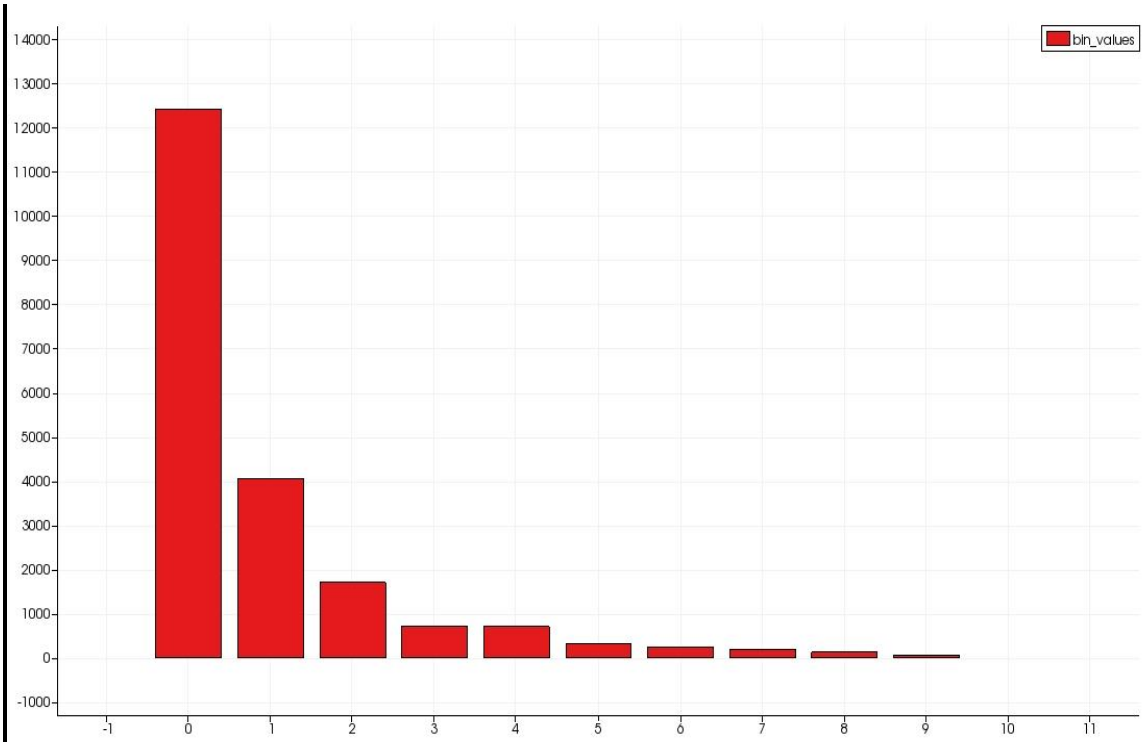

Figure 51 . Histogram of the Hausdorff Distance. It describes amounts of the points in two datasets have the distance 0 (points of two data sets are completely overlapped) until 9 (minimum overlap between points of two datasets). (Y-axis shows amount of the points while X-axis shows the distance in mm). (Dataset ID : 886)

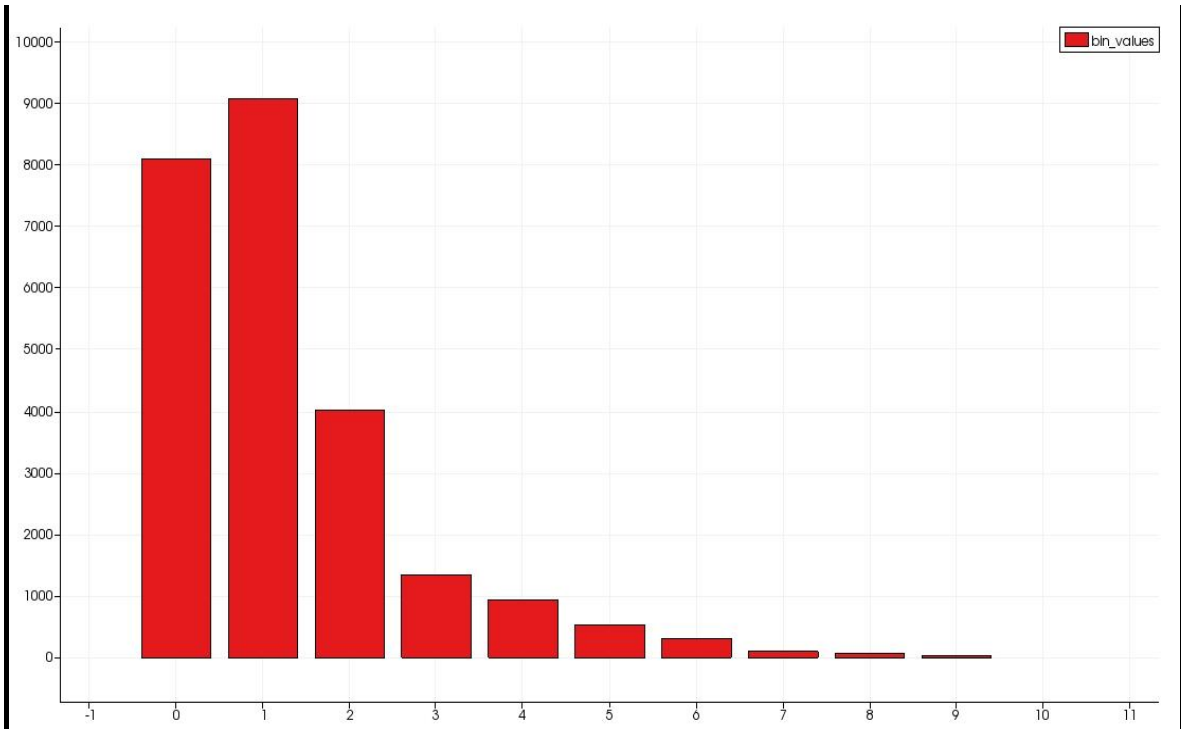

Figure 52 . Histogram of the Hausdorff Distance. It describes amounts of the points in two datasets have the distance 0 (points of two data sets are completely overlapped) until 9 (minimum overlap between points of two datasets). (Y-axis shows amount of the points while X-axis shows the distance in mm). (Dataset ID : 937)

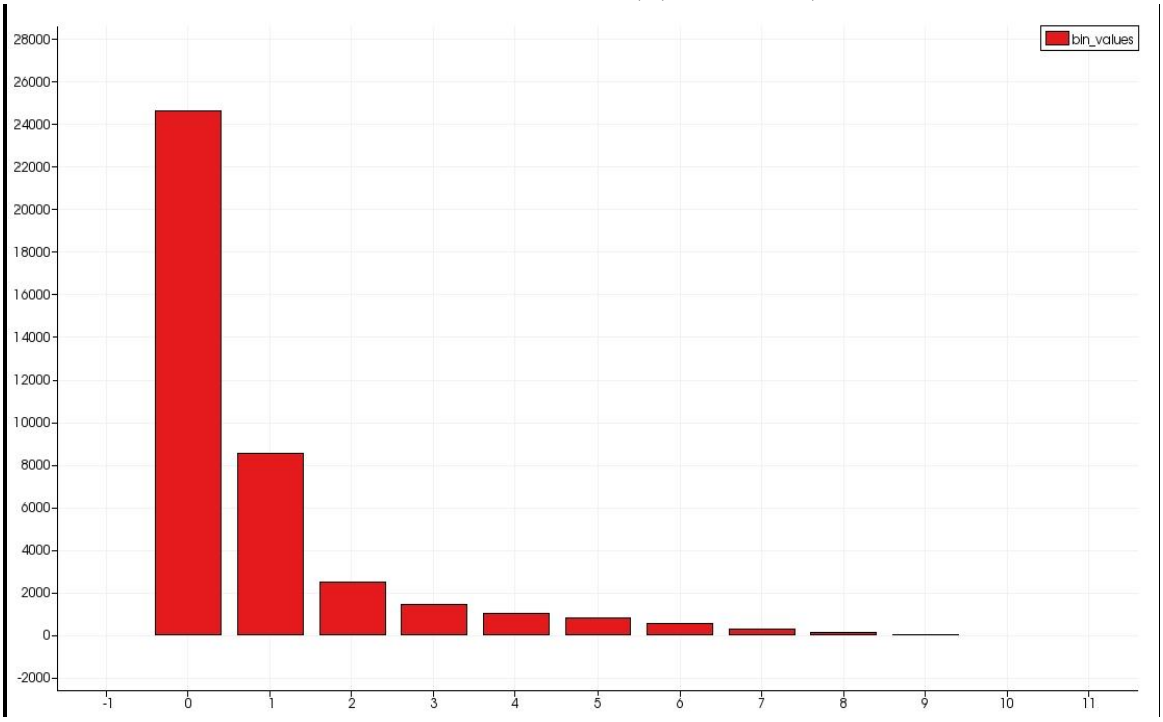

Figure 53 . Histogram of the Hausdorff Distance. It describes amounts of the points in two datasets have the distance 0 (points of two data sets are completely overlapped) until 9 (minimum overlap between points of two datasets). (Y-axis shows amount of the points while X-axis shows the distance in mm). (Dataset ID : 969)

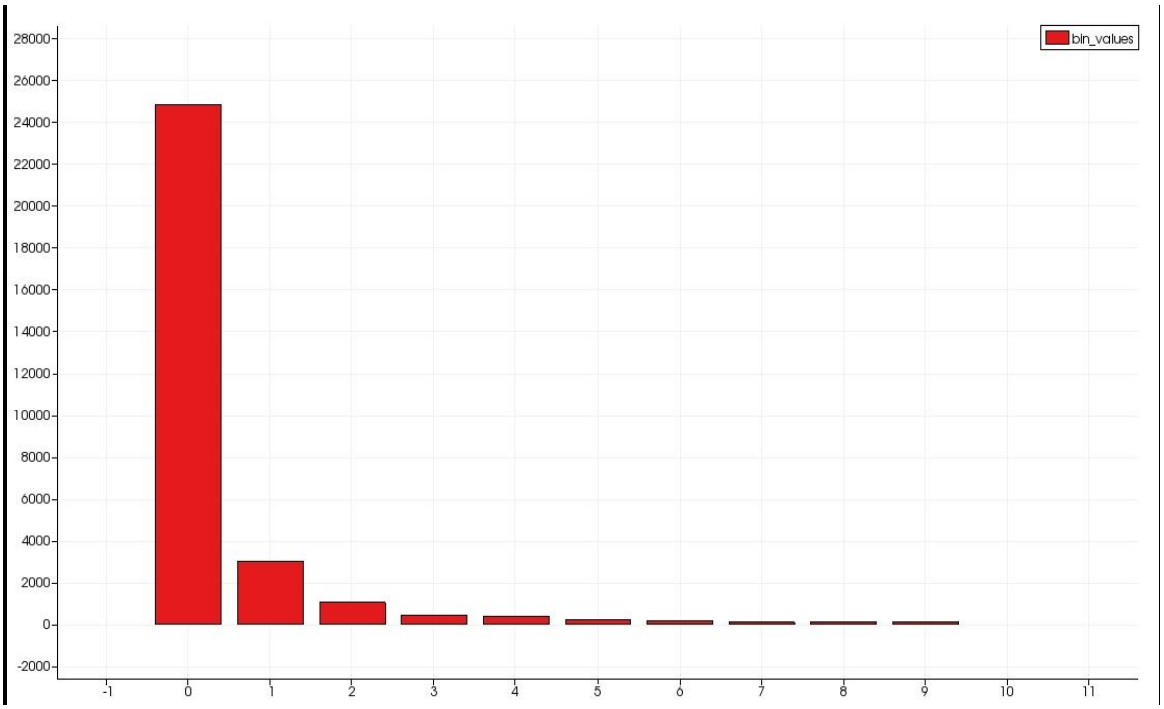

Figure 54 . Histogram of the Hausdorff Distance. It describes amounts of the points in two datasets have the distance 0 (points of two data sets are completely overlapped) until 9 (minimum overlap between points of two datasets). (Y-axis shows amount of the points while X-axis shows the distance in mm). (Dataset ID : 996)

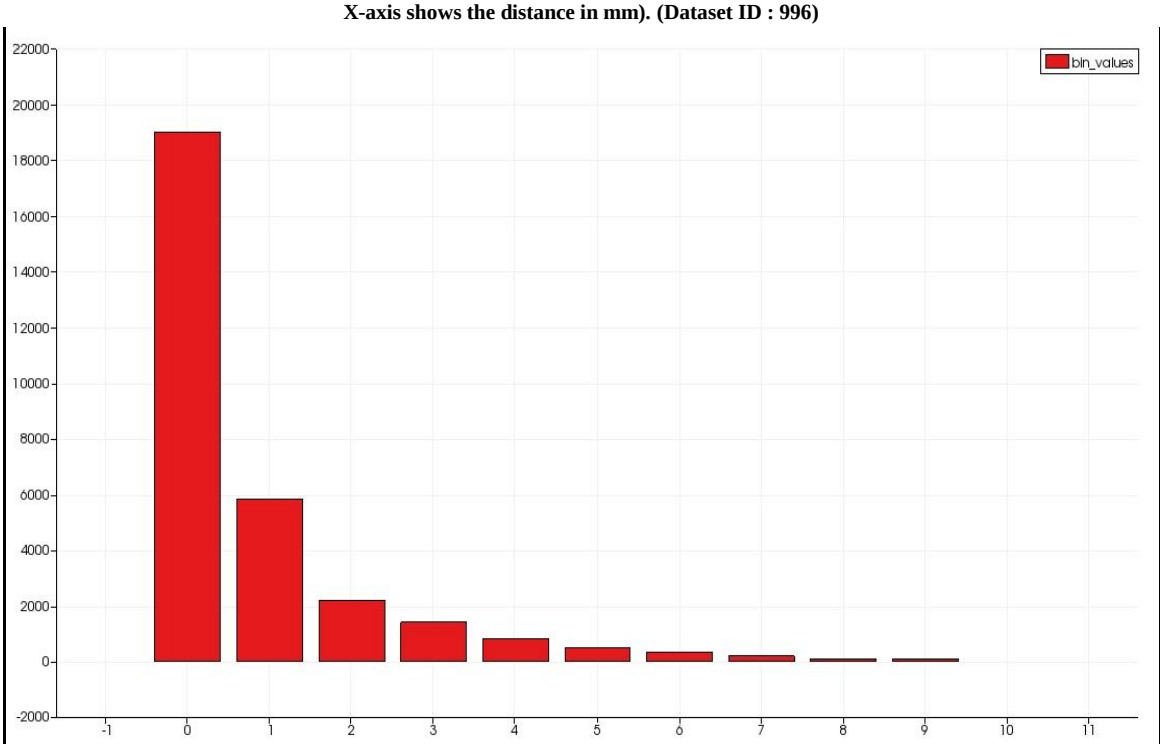

Figure 55 . Histogram of the Hausdorff Distance. It describes amounts of the points in two datasets have the distance 0 (points of two data sets are completely overlapped) until 9 (minimum overlap between points of two datasets). (Y-axis shows amount of the points while X-axis shows the distance in mm). (Dataset ID : 1063)

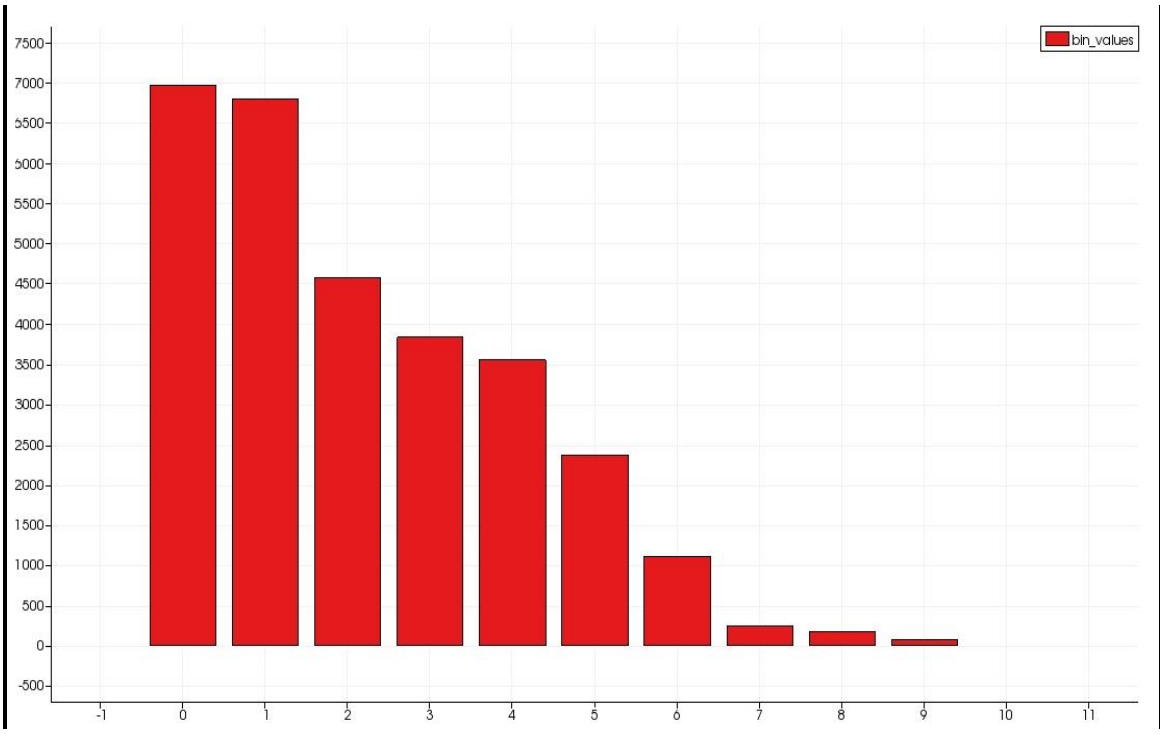

Figure 56 . Histogram of the Hausdorff Distance. It describes amounts of the points in two datasets have the distance 0 (points of two data sets are completely overlapped) until 9 (minimum overlap between points of two datasets). (Y-axis shows amount of the points while X-axis shows the distance in mm). (Dataset ID : 1092)

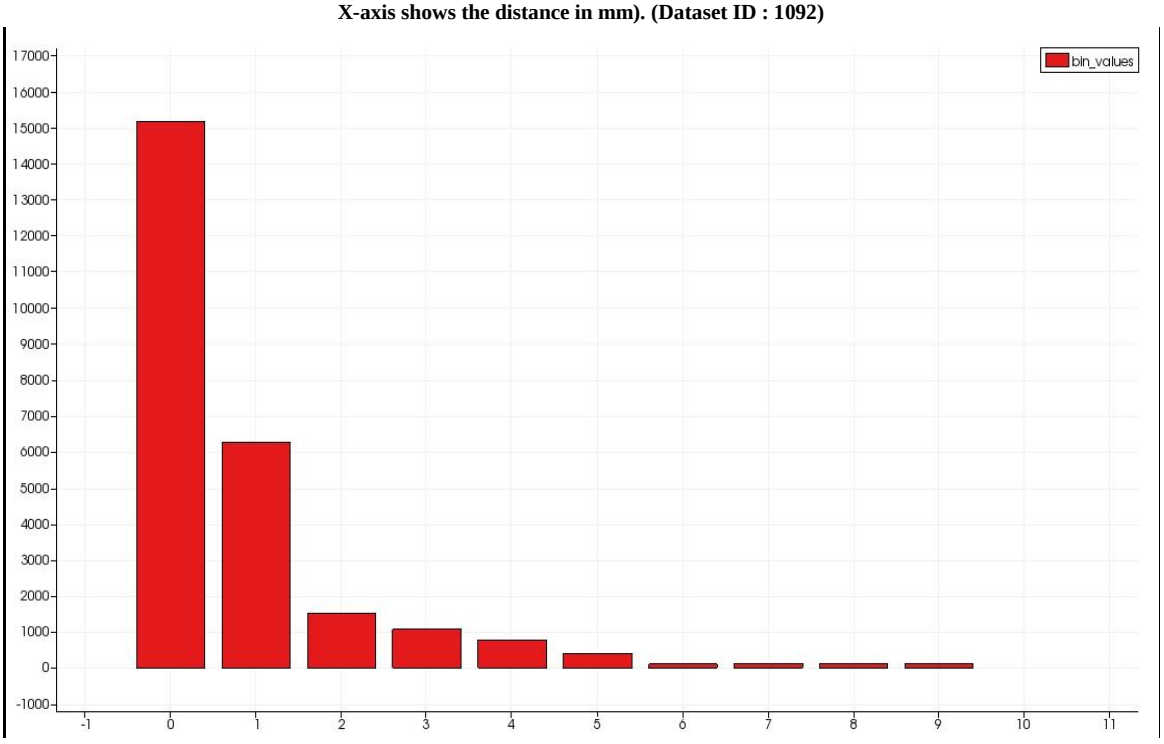

Figure 57 . Histogram of the Hausdorff Distance. It describes amounts of the points in two datasets have the distance 0 (points of two data sets are completely overlapped) until 9 (minimum overlap between points of two datasets). (Y-axis shows amount of the points while X-axis shows the distance in mm). (Dataset ID : 1133)